

THE UNIVERSITY OF HULL

Microcapsule synthesis for 3D printing of self-healing materials

being a Thesis submitted for the Degree of

Doctor of Philosophy

in the University of Hull

By Polly Sanders

April 2021

ACKNOWLEDGEMENTS

I would first like to thank my supervisors, Prof. Nicole Pamme and Asst. Prof. Jia Min Chin (University of Vienna) for your guidance and support. As well as the University of Hull for funding my studies and allowing me to continue my further education.

Grateful thanks is also given to all my fellow researchers in both the Chin and Pamme research groups. For all your advice on various aspects of this work as well as providing friendship and emotional support.

I would like to give specific thanks to Dr Alexander Iles who fabricated the glass devices, Ellis Marshall for helping with the 3D printing and Solweig Chartier for helping me collect the droplet measurements.

TABLE OF CONTENTS

TABLE OF CONTENTS	3
ABSTRACT.....	9
LIST OF ABBREVIATIONS.....	11
1.....	INTRODUCTION
13	
<i>1.1 3D Printing</i>	<i>13</i>
1.1.1 Filament/ink based printing	15
1.1.2 Vat photopolymerisation 3D printing methods.....	16
1.1.3 (Meth)acrylate based photocurable systems	18
1.1.4 SLA 3D printing of composite materials	22
<i>1.2 Self-Healing Materials.....</i>	<i>24</i>
1.2.1 Intrinsic self-healing	25
1.2.2 Extrinsic self-healing	28
1.2.4 Demonstration and quantification of self-healing.....	32
1.2.5 Introduction to crack propagation.....	36
1.2.6 Applications	37
1.2.7 Transparent self-healing materials	38

1.2.8 Refractive index matching for transparent composites.....	39
1.3 Capsule synthesis for extrinsically self-healing materials	42
1.4 Droplet Microfluidics for vesicle generation	43
1.4.1 Flow regimes in microfluidic devices.....	45
1.4.2 Droplet microfluidics for materials generation.....	50
1.4.3 Droplet generation using viscous liquids.....	54
1.5 3D printing of self-healing materials	55
1.6 Project Aims	56
2.....	EXPERIMENTAL
58	
2.1 Chemicals	58
2.2 In-situ encapsulation of self-healing materials with urea-formaldehyde shell.....	60
2.3 In-situ encapsulation of self-healing materials with PMMA shell.....	62
2.4 In-situ encapsulation of self-healing materials with commercial resin shell	63
2.7 Preliminary healing agent plane welding screening tests.....	64
2.6 Preliminary studies for microfluidic droplet generation.....	65

<i>2.7 Generation of capsules for self-healing using droplet microfluidic devices</i>	65
<i>2.8 Microfluidic devices – Fabrication and interfacing</i>	66
2.8.1 Glass microfluidic devices	66
2.8.2 PDMS microfluidic devices	70
<i>2.9 Size distribution analysis</i>	74
<i>2.10 SEM analysis</i>	75
<i>2.11 IR analysis</i>	75
<i>2.12 TGA analysis</i>	75
<i>2.13 Generation of formulations for stereolithographic printing resins</i>	76
<i>2.14 Tapered double cantilever beam (TDCB) measurements and quantification of self-healing</i>	76
<i>2.15 3D printing</i>	79
3. STEREO LITHOGRAPHIC 3D PRINTING OF EXTRINSICALLY SELF-HEALING MATERIALS	80
<i>3.1 Capsule synthesis, characterisation and size distribution analysis</i>	80
<i>3.2 Formulation of self-healing composites</i>	85
<i>3.3 Quantification of self-healing efficiency</i>	87

<i>3.4 3D printing</i>	95
<i>3.5 Conclusion to stereolithographic 3D printing of extrinsically self-healing materials</i>	97
4.INVESTIGATION INTO THE PRODUCTION OF MICROCAPSULES FOR USE IN TRANSPARENT SELF-HEALING MATERIALS VIA TRADITIONAL MIXING METHODS	98
<i>4.1 PMMA capsules</i>	100
<i>4.2 Commercial resin capsules</i>	102
4.2.1 Investigation into type of surfactant	105
4.2.2 Investigation into core material	106
4.2.3 Investigation into surfactant concentration	108
4.2.4 Investigation into phase volume ratio	108
4.2.5 Investigation into mixing method	109
<i>4.4 Conclusion to investigation into the production of capsules for transparent self-healing materials via traditional mixing methods</i>	111
5.INVESTIGATION INTO THE PRODUCTION OF MICROCAPSULES FOR USE IN TRANSPARENT SELF-HEALING MATERIALS THROUGH UTILISATION OF MICROFLUIDIC DEVICES	112
<i>5.1 Preliminary droplet studies</i>	112

<i>5.2 Utilisation of glass microfluidic devices for production of self-healing capsules.....</i>	<i>113</i>
5.2.1 Investigation into flow rate	115
5.2.2 Investigation into composition and viscosity of discontinuous phase	117
5.2.3 Investigation into the viscosity of the continuous phase	121
5.2.4 Conclusion into the use of glass devices for the production of self-healing capsules	124
<i>5.3 Utilisation of PDMS microfluidic devices for production of self-healing capsules.....</i>	<i>125</i>
5.3.1 Utilisation of a PDMS device with the same dimension as MD2.....	127
5.3.2 Utilisation of a PDMS device with narrower channels and longer outlet.....	129
5.3.3 UV Polymerisation of microfluidic produced droplets.....	131
<i>5.4 Conclusion to investigation into the production of capsules for transparent self-healing materials through utilisation of microfluidic devices</i>	<i>132</i>
6.MICROFLUIDIC-ASSISTED PRODUCTION OF TRANSPARENT EXTRINSICALLY SELF-HEALING MATERIALS FOR 3D PRINTING	133
<i>6.1 Self-healing preliminary trials.....</i>	<i>136</i>
<i>6.2 Formulation of self-healing composites</i>	<i>136</i>
<i>6.3 Quantification of self-healing</i>	<i>137</i>

6.4 3D Printing.....140

6.5 Conclusion.....141

**7..... CONCLUSION
142**

**8..... REFERENCES
144**

ABSTRACT

3D printing allows for the manufacture of finished structures from starting components with essentially no specialist training required. The process is autonomous; the starting components, such as inks, are poured into the machine and the finished product is produced with no intervention from the user. Currently, most commercial printers only produce structures which have limited functionality and are often used to produce 'prototypes' rather than a finished product. There have been recent advancements in the utilisation of 3D printing to produce structures which have longer lifespans, wider material choice and improved functionality, in order to extend the utility of printed structures beyond prototyping and expand potential applications. Within the research reported in this thesis, the focus is primarily on the production of 3D printing resins with embedded capsules, which can be utilised in 3D printers for the production of microcapsule containing composites. Specifically, these capsules contain solvents and polymers which can be used for self-healing with the intention of extending the lifetime and toughness of any structures built by 3D printers using these materials.

In this work, the 3D printing of self-healing materials is shown through the use of 3D printing resins modified with solvent and polymer containing urea-formaldehyde microcapsules. Urea-formaldehyde capsules are utilised widely in the literature for extrinsically self-healing microcapsule-based systems. The inclusion of the capsules showed no harmful effect on the quality of printing and mechanical testing showed the capability of fracture toughness recovery after healing via a classic solvent welding mechanism to be 48-59% depending on which solvent and concentration was used. The addition of poly(methyl methacrylate) chains into the core of the capsules and increasing the healing time to 72 hours enhanced the self-healing ability of the solvent anisole. Under these conditions, mechanical testing showed a capability for fracture toughness recovery of 87%.

A more novel production route for microcapsules was also explored. The ability to generate an optically transparent self-healing system would be beneficial for utilisation in applications which require optically transparent materials. Microfluidic devices were utilised to produce microcapsules with a transparent resin shell and liquid oligomer core.

Therefore, a key investigation for this work regarded the optimisation of capsule generation via droplet microfluidic devices. Droplet microfluidic devices generated the capsules in one at a time with sequential UV polymerisation in a continuous flow fashion, this proved an elegant solution to some of the problems seen when investigating production using a batch mixing process. Despite concerns with regards to high viscosities (230-11,000 mPa s) and the complex rheology associated with polymer blends, it was shown that droplet generation can be controlled via microfluidics. This fixed some issues seen when trying to optimise this process using batch synthesis routes, producing superior capsules than a due to the high degree of control afforded by microfluidic devices.

These capsules were successfully utilised in a 3D printer and the reduced light scattering from these microcapsules when compared to the urea-formaldehyde capsules was significant. Here, we show that this mechanism had the ability to recover fracture toughness of up to 83%.

LIST OF ABBREVIATIONS

ABS	Acrylonitrile butadiene styrene
CAD	Computer aided design
CNC	Computer numerical controlled
CP	Continuous phase
DLP	Digital light processing
DP	Dispersed phase
EPA	Ethyl phenylacetate
FDM	Fused deposition modelling
FTIR-ATR	Fourier transform infrared
PCR	Polymer chain reaction
PDMS	Poly(dimethylsiloxane)
PLA	Poly(lactic acid)
PMMA	Poly(methyl methacrylate)
pNIPAAm	Poly(N-isopropylacrylamide)
PolyTHF	Polytetrahydrofuran
RI	Refractive Index
SEM	Scanning electron microscopy
SDS	Sodium dodecyl sulfate
SLA	Stereolithography
TDCB	Tapered cantilever-double beam
TGA	Thermogravimetric analysis

UF Urea formaldehyde

UV Ultraviolet

1. INTRODUCTION

In this chapter an overview of 3D printing techniques will be described and the modification of stereolithographic 3D printing resins for composite material printing will also be discussed. An introduction to self-healing mechanisms will be covered; particular attention will be paid to capsule based extrinsically self-healing mechanisms and the current developments towards transparent self-healing materials. The fabrication methods of microcapsules for self-healing mechanisms will be explored with the advantages of using droplet microfluidic devices for capsule production over more traditional synthesis routes discussed. Finally, the aims of the research described in this thesis will be laid out.

1.1 3D Printing

3D printing, also referred to as additive manufacturing, rapid prototyping or solid-freeform technology, is of increasing interest for the chemical and biological sciences.^{1,2} The concept was first established by Charles Hull, who developed the method stereolithography (SLA) and the .STL file format.³

In 3D printing, computer aided designs (CAD) are converted into an STL file which is a 3D data format, where the surface of the design can be visualised as a series of connected triangles. This conversion is generally followed by the use of ‘slicing’ software, which generates a G-code file; a readable set of commands for the printer instructing where to move and how fast to move using X and Y coordinates. After each layer has been produced, the build plate is moved along the Z axis (Figure 1).

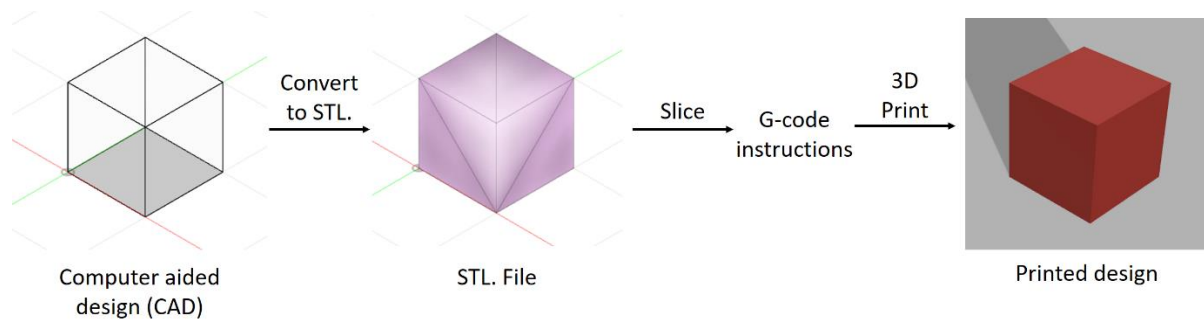


Figure 1: Sequence of steps showing the conversion of a CAD drawing to an STL file, followed by the slicing process to produce the G-code instructions that can be read by the 3D printer to produce the print.

For industry, the utilisation of such technology is attractive as parts can be produced quickly, without the need for specialist training. Prints can be produced within hours of being downloaded from digital STL files in data banks. Thus, storage requirements could be drastically reduced, as replacement parts do not need to be stored on site but can be produced on demand which could also lead to a reduction in waste. The potential to share these files and edit them to personal requirements using various software packages, also offers a great amount of flexibility for users of this technology.^{4,5}

A major disadvantage of these printers includes lack of choice when it comes to commercially available materials for printing. 3D printing has traditionally utilised thermoplastic filament as the material of choice for printing⁶⁻⁹. Research has already been conducted into developing new materials and methods that have successfully produced prints with improved physical traits when compared to prints produced using traditional 3D printing materials¹⁰⁻¹². Fluids rather than solid filaments have garnered much interest due to their tunability for different applications. Here, the aim is to widen the choices available for printing materials and more specifically, expand the ability to 3D print composite materials with extended lifespans, increased toughness and self-healing capability. Expansion of the catalogue of materials

available for 3D printing is important for its application beyond prototyping to be realised and be seen as a viable option for the manufacture of finished, fully functioning products.

1.1.1 Filament/ink based printing

Fused deposition modelling (FDM) is an extrusion based 3D printing method. A nozzle is used on a printer head from which the printing material is extruded (Figure 2a). Traditionally, FDM utilises thermoplastic filaments such as poly(lactic acid) (PLA) or acrylonitrile butadiene styrene (ABS) which require the heating of the nozzle to produce melted filament. The filament then solidifies on cooling once it has been deposited on the build plate. FDM is commercially the most popular 3D printing technique,¹³ this is due to the relatively low cost of these systems and the filaments when compared with other techniques. Due to the popularity of this technique, there has been much research on developing individual aspects of the printers, including materials, extrusion speed and bed temperature, in order to increase print quality.¹³

The desire to expand the materials beyond the scope of simple thermoplastics for deposition printers has led to the development of a technique called the direct-write. For direct write, rather than using thermoplastic filament, an area of keen research interest is the use of photo curable or thermal curable inks/pastes (Figure 2b). When the material is deposited on the build plate, heat or a ultraviolet (UV) light source is used to crosslink the monomers and create a solid structure. These inks have viscoelastic properties, which allow them to behave like a fluid and be easily manipulated but ‘set’ or gel quickly when they have been deposited onto the build plate. Due to no longer being restricted to thermoplastics, these inks can be modified to suit a wide variety of different applications.^{14,15}

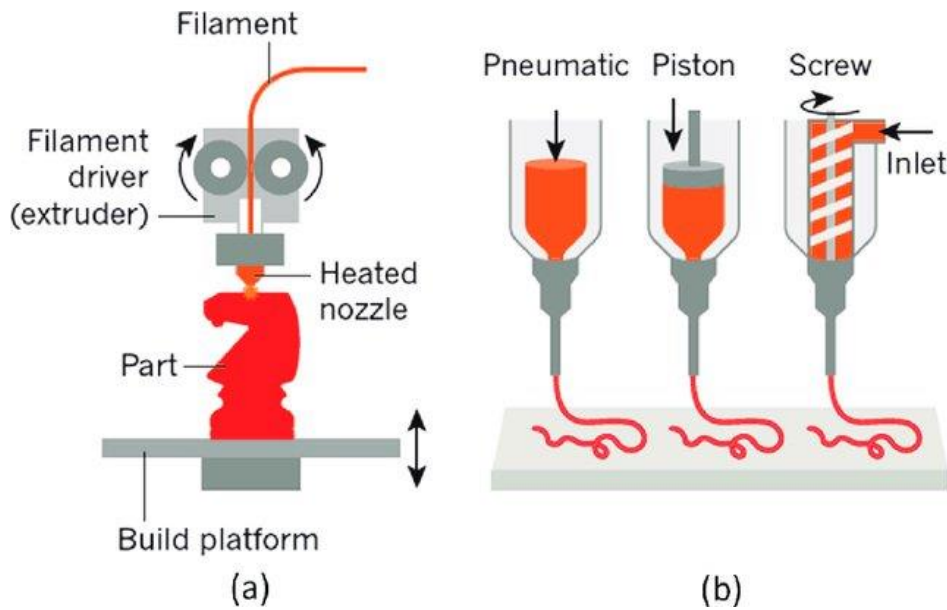


Figure 2: Deposition based 3D printing methods.¹⁵ a) Schematic showing the FDM extrusion method. b) Schematic showing the direct write method, with pneumatic, piston or screw based extrusion methods for the inks/paste.

1.1.2 Vat photopolymerisation 3D printing methods

The first 3D printing technology to be developed was stereolithographic printing (SLA). Developed by Charles Hull, it utilised a resin tank of photo curable resin and a laser for which to induce highly precise crosslinking of the resin to produce a solid structure (Figure 3). The structure is produced layer by layer and the resin tank is lowered after each layer has been created. SLA ‘grows’ the required print from reservoirs of material^{16–18}. The main advantage of SLA over other 3D printing methods is the high level of detail that can be attained; prints with features of up to 10 μ m have been achieved.¹⁰ An emerging method of the vat polymerisation technique is known as digital light processing (DLP). The working principle is very similar to SLA, although rather than using a laser to selectively polymerise the resin point by point, an array of up to a million mirrors is used, which can be independently turned to an ‘on’ or ‘off’ mode. Projection of light onto this array allows for the entire layer of the print to be polymerised at once, reducing print time drastically.¹⁹

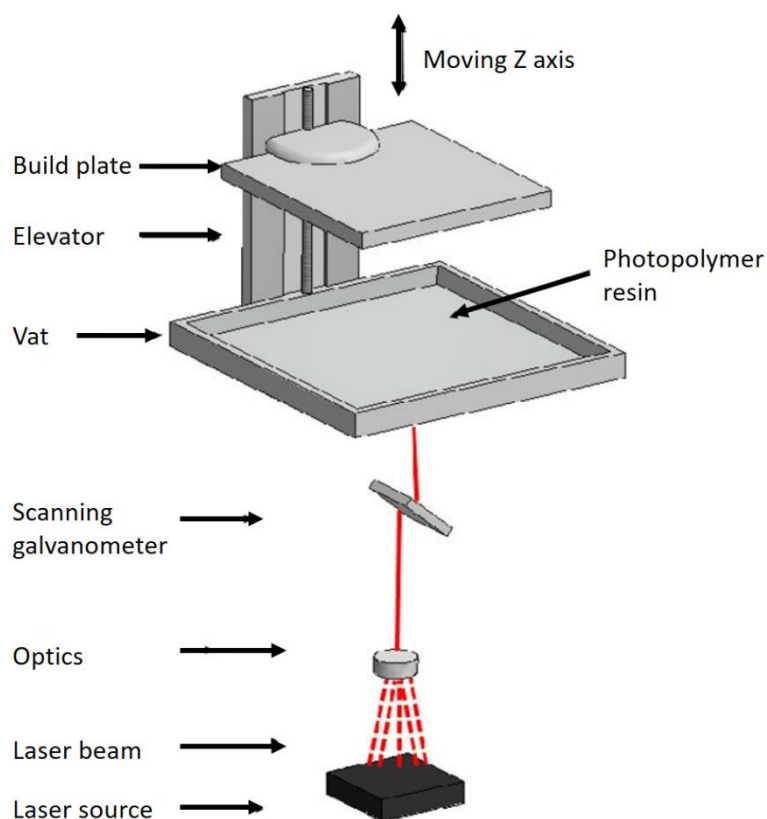


Figure 3: Schematic showing the SLA 3D printing process.¹⁶

There are many different photopolymer resin formulations available on the market. Many common SLA printers utilise a radical polymerisation mechanism; the composition of the resin mixture used consists of mainly acrylate and methacrylate monomers and oligomers due to low volatility, high reactivity, low colour and resistance to environmental and chemical degradation compared to other oligomers.²⁰ There will also be a photoinitiator (or tailored mixture of photoinitiators) in order to induce radical polymerisation of the oligomers/monomers.²¹ A high absorption coefficient photoinitiator is chosen in order to drive the radical polymerisation process. Most photoinitiator systems utilised are tailored to work at relatively short wavelengths (400 nm).²²

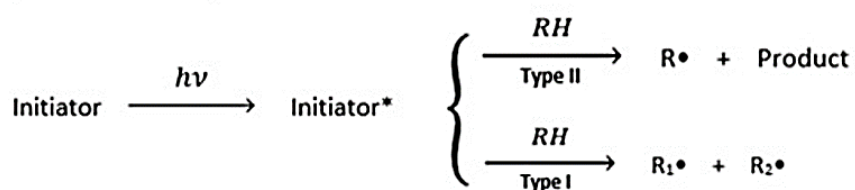
The mixture of oligomers, monomers and photoinitiators chosen is tailored to the printing process. A more detailed discussion focusing on (meth)acrylate systems commonly found in photopolymerisable resins will follow next.

1.1.3 (Meth)acrylate based photocurable systems

The resin mixtures utilised within these printers are composed of three major components; photoinitiator species (which produce free radical species upon exposure to UV light), functionalised oligomers (these will form the main body of the polymer matrix upon polymerisation) and functionalised monomers (these lower molecular weight reactive components are often added in order to act as dilutents and control the viscosity of the mixture).²³

Polymerisation occurs through a free radical polymerisation mechanism outlined in Figure 4.

Photoinitiation



Propagation



Chain-Transfer



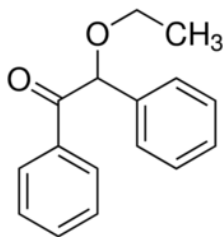
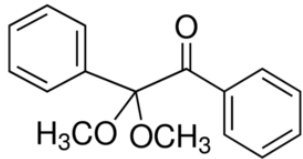
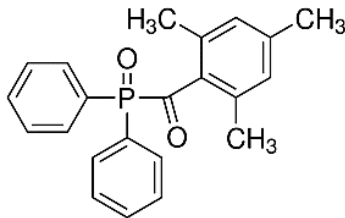
Termination



Figure 4: Schematic outlining the steps for a free radical polymerization reaction with monomer M, containing a C=C bond and photoinitiator R.²⁴ **Photoinitiation:** upon exposure to UV light, absorption of photon leads to production of radical species which readily react with the monomer. **Propagation:** Continued reaction of the monomer radical with the monomer species, leading to chain growth. **Chain-Transfer:** Transfer of a growing polymer chain onto another molecule terminating chain growth (will lead to a lower molecular weight of the final polymer) **Termination:** Chain growth is halted by a coupling or disproportionation reaction, removing the radical species.

The majority of commercially available photoinitiators undergo type 1 cleavage when exposed to UV to form a pair of radical fragment species.²⁵ A summary of common type 1 initiators found in photocurable resin is found in Table 1. The radical species will quickly attack the monomer species through the C=C bond generating a further functionalised radical species. Subsequent continued reactions with further monomer will result in propagation and chain growth. Termination of chain growth occurs through either coupling or disproportionation reactions.²⁴

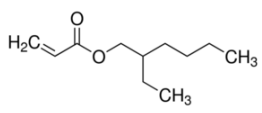
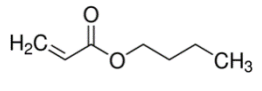
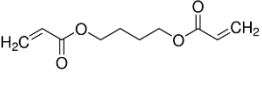
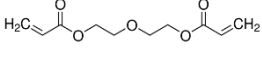
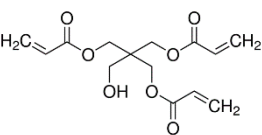
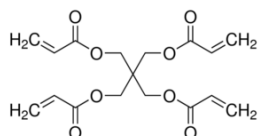
Table 1 Summary of the photoinitiators utilised in photopolymerisable resins required for initiation of free radical polymerisation.

Class	Example	Structure	Reference
Benzoin ethers	Benzoin ethyl ether		26
Benzil ketals	2,2-dimethoxy-2-phenylacetophenone		27
Acyl phenyl oxides	2,4,6-triDiphenyl(2,4,6-trimethylbenzoyl)phosphine oxide		28,29

The exact formulations of UV curable resins is often proprietary. Examination of patents and investigation of these resins has provided the research community with a better understanding of the composition of these resins.

A monomer is selected for a specific application due to its material properties, or the processing parameters of the printer, this could be due to its effect on curing speed, viscosity, deformation/shrinkage during polymerisation, volatility, colour, toxicity cost and shelf life. The most widely used monomers are acrylates.²⁷ A summary of common acrylate monomers used is summarised in Table 2.

Table 2: Summary of monomers often used in photopolymerisable resins. The choice of monomer is determined by the final material properties required and the conditions needed for the printing process.

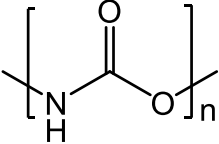
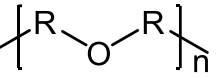
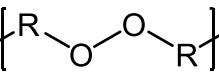
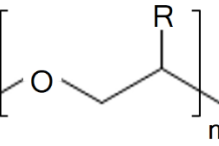
Class	Example	Structure	Pros	Cons	Reference
Monoacrylate	2-Ethylhexyl acrylate		Flexible	Slow cure, volatile and low solvent resistance	³⁰
Monoacrylate	Butyl-acrylate		Flexible and good diluent	Slow cure, volatile and low solvent resistance	³¹
Diacrylate	1,4-Butanediol diacrylate		Low volatility and good diluent	Suspected skin sensitiser	³²
Diacrylate	Di(ethylene glycol) diacrylate		Good diluent	Toxicity and skin sensitiser properties	³³
Triacrylate	Pentaerythritol triacrylate		Fast curing	Suspected carcinogen, eye irritant	³⁴
Tetraacrylate	Pentaerythritol tetraacrylate		Low volatility	Suspected carcinogen, eye irritant	³⁴

For the oligomer component, when designing photocurable resins, a mixture of acrylates and methacrylates are often used, as methacrylate species cure very slowly on their own; using only acrylates can cause deformation in the final printed object.³⁵ Four acrylate polymer structures are widely used in photopolymerisation resins these are; polyurethane, polyethers,

polyesters and epoxy. These polymer blocks make up the body of the oligomer structure with the acrylate functional groups present at the chain end.²⁴

Selection of the polymer backbone is important to the final properties of the polymerised material, as this component will constitute the main part of the matrix. Which polymer is chosen for the resin depends on the specific application, Table 3 summarises these polymers and outlines the positive and negative effects of each.

Table 3: Summary of polymer blocks commonly used in photopolymerisable resin.^{24,27} Each polymer results in differing properties of the final polymerised material.

Class	Chemical structure	Pros	Cons
Polyurethane		Best balance of hardness and elasticity.	Yellow colour, costly, toxic and plasticised by H ₂ O.
Polyether		Good adhesion, flexibility, elasticity and UV-resistance.	Low glass transition temperature.
Polyester		Good adhesion and hardness.	Poor hydrolytic ability, Poor UV resistance.
Epoxy		Good adhesion, hydrolytic ability, hardness and chemical resistance.	High viscosity. Poor UV resistance.

1.1.4 SLA 3D printing of composite materials

A major disadvantage of SLA 3D printing method is the difficulty of changing resin/powder reservoirs when it is required to print using more than one material.^{36,37} As a result there is less materials available for SLA printers compared to other methods.³⁸ In order to print composite

materials therefore, a solution to this challenge is to utilise modified resins which provide additional functionality or can be treated post printing to produce this functionality. This allows for complex materials to be printed without the need for multiple reservoirs of material.

Modified resin come with their own challenges however. The inclusion of additives or fillers to the resin can alter the viscosity of the mixture which can negatively impact the 3D printing process.³⁹⁻⁴¹ Care needs to be taken that any additives do not interfere with the polymerisation chemistry. The presence of filler particles can also cause light scattering effects which can limit cure depth.⁴² Attention also needs to be taken to ensure that any particles do not exceed the layer height of the 3D printing process.⁴³ Despite these challenges, modified photopolymerisable resins are a keen area of research due to the high level of resolution afforded by SLA compared to other 3D printing methods.

A high number of modified SLA resins revolve around the improvement of mechanical properties of the polymerised matrix. The incorporation of graphene oxide to improve the tensile strength of polymer composites is a popular area of research.^{44,45} Compared with carbon nanotube reinforcing,^{46,47} at only 0.2 wt% loading, graphene oxide provided not only improved tensile strength (increase of 62.2%) but provides good ductility to the resulting polymer (increase of 12.8% elongation).⁴⁵ The incorporation of nanoclays has also allowed for the improvement of mechanical properties. Montmorillonite nanoclay, with dimensions up to 1 μm , when loaded into photopolymer resins at a loading of 3 wt% resulted in a 70 % increase in Young's modulus in the x-y plane while also enhancing ductility (up to 100% increase in elongation).⁴⁸ These examples suggest the use of nanoparticles at these loadings does not affect the printing process.

As well as improving the mechanical properties of the printed objects, highly porous materials have also been generated. One such example is the use of high internal phase emulsions (80%

volume) acting as the resin. After polymerisation, evaporation of the internal phase from the polymer matrix produces highly porous materials for use in a wide variety of applications.^{49,50} An average pore diameter of 2.2 μm was achieved-determined from the size of the droplets loaded in the resin. Selectively not polymerising resin allowed for the production of secondary interconnecting pores with features of 1.5 μm were achieved. The layer height was maintained at 25 μm . Emulsion filled inks have also been utilised to show that the reverse, polymerisation of the droplets and evaporation of the continuous phase can also produce highly porous structures.⁵¹ In this particular example, inclusion of nanoparticles within the discontinuous phase also added electrical conductivity functionality to the material.

1.2 Self-Healing Materials

Self-healing materials have the ability to repair damage and regain some of the lost functionality of the material.⁵² Self-healing mechanisms can be considered autonomous (triggered by crack formation alone) or non-autonomic, which require external triggers such as heat or light. The ability to mimic this healing ability for synthetic materials would have great potential in applications that require longevity, in particular in areas with low accessibility. Many examples of self-healing can be seen in living organisms, such as the blood clotting mechanism seen with cuts or the healing of bone fractures. As a result, research in this area is heavily inspired by the examples we can see in nature. This is illustrated by the examples in Figure 5.⁵³ Inspiration was taken from the lotus leaf which has superhydrophobic leaves in order to produce self-cleaning surfaces.⁵⁴ The weeping fig tree which releases latex upon damage to the tree, stirred the development of microcapsule based self-healing material.⁵⁵ Blood vessel systems within animals have inspired vascular self-healing systems, whereby channels of self-healing material are embedded into the polymer which rupture upon fracture and heal the crack.^{56,57}

Over time, two distinct types of self-healing mechanism have emerged; intrinsic and extrinsic self-healing.

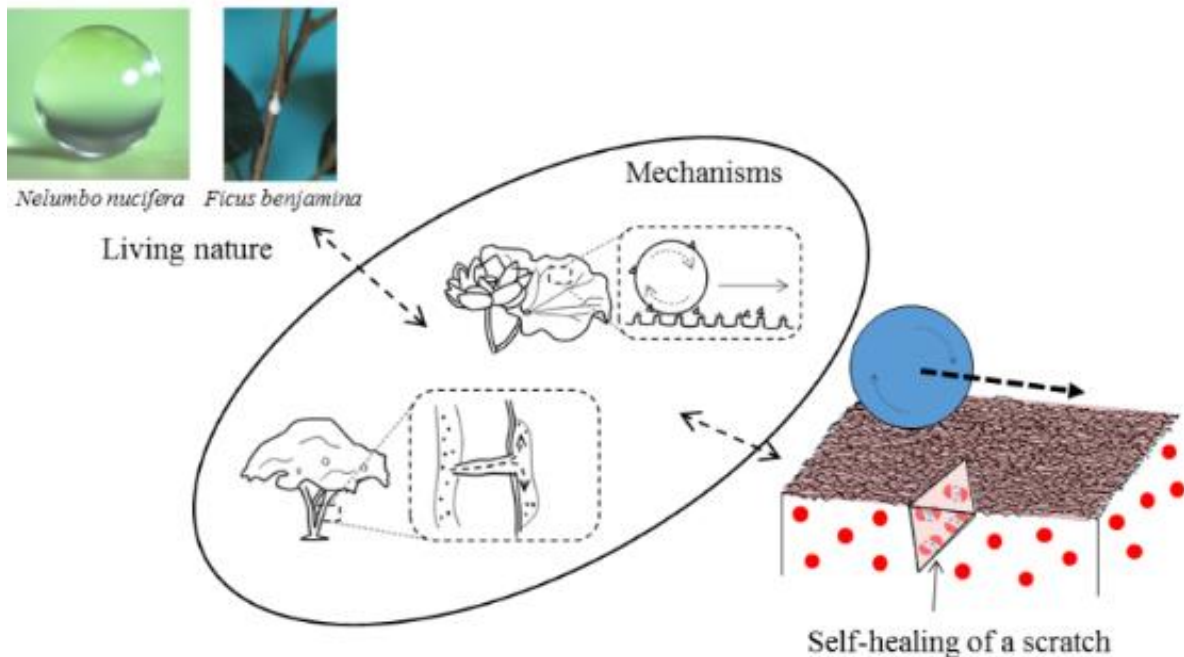


Figure 5: Translation of healing in nature into self-cleaning and self-healing materials.⁵³ The self-cleaning lotus leaf (*Nelumbo nucifera*) has led to the development of self-cleaning materials based on super hydrophobic and micro-structured surfaces.⁵⁴ Self-healing materials have been inspired by the vascular cells of the weeping fig tree (*Ficus benjamina*) which secretes latex upon damage.⁵⁵ This is mimicked in synthetic self-healing materials through targeted capsule delivery of self-healing material.

1.2.1 Intrinsic self-healing

Intrinsic self-healing mechanisms are possible due to the properties of components of the host material, with no self-healing component having to be added to the matrix.⁵⁸

One possibility for the development of intrinsic materials is to consider the possible chemical interactions, Figure 6. The breaking of bonds when damage is inflicted and the subsequent reformation/rearrangement of bonds have been shown as an example of intrinsic healing.^{59,60}

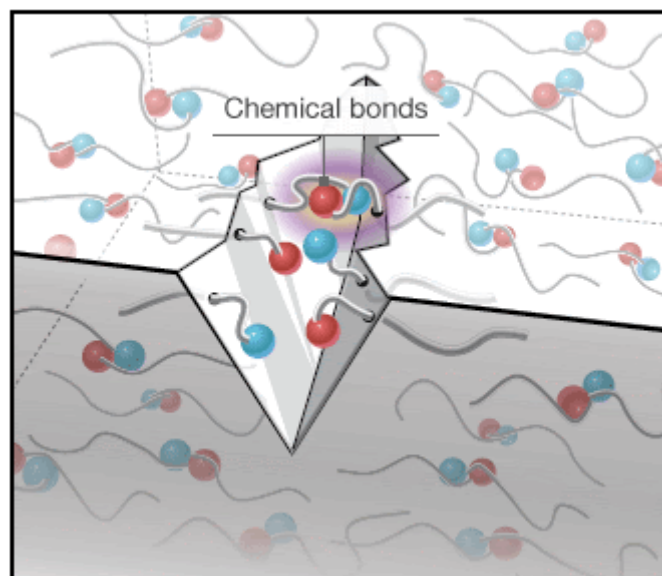


Figure 6: Schematic representation of intrinsic self-healing.⁶¹ This approach requires the polymer to have intrinsic functionality such as reversible bonds to allow for healing of damage.

Non covalent bond reshuffling such as hydrogen bonding⁶² and metal ion binding⁶³ has been investigated. Investigation into dynamic covalent bonds has also been carried out, for example, polyurethane has been shown to successfully self-heal using a mechanism that utilises the radical reshuffling of disulphide bonds under the stimulation of visible light.⁶⁴ Room temperature intrinsic self-healing of a hydrogel that was crosslinked with zirconium hydroxide nanoparticles has also been shown, Figure 7.⁶⁵ This was possible through the breakage and reforming of hydrogen bond networks.

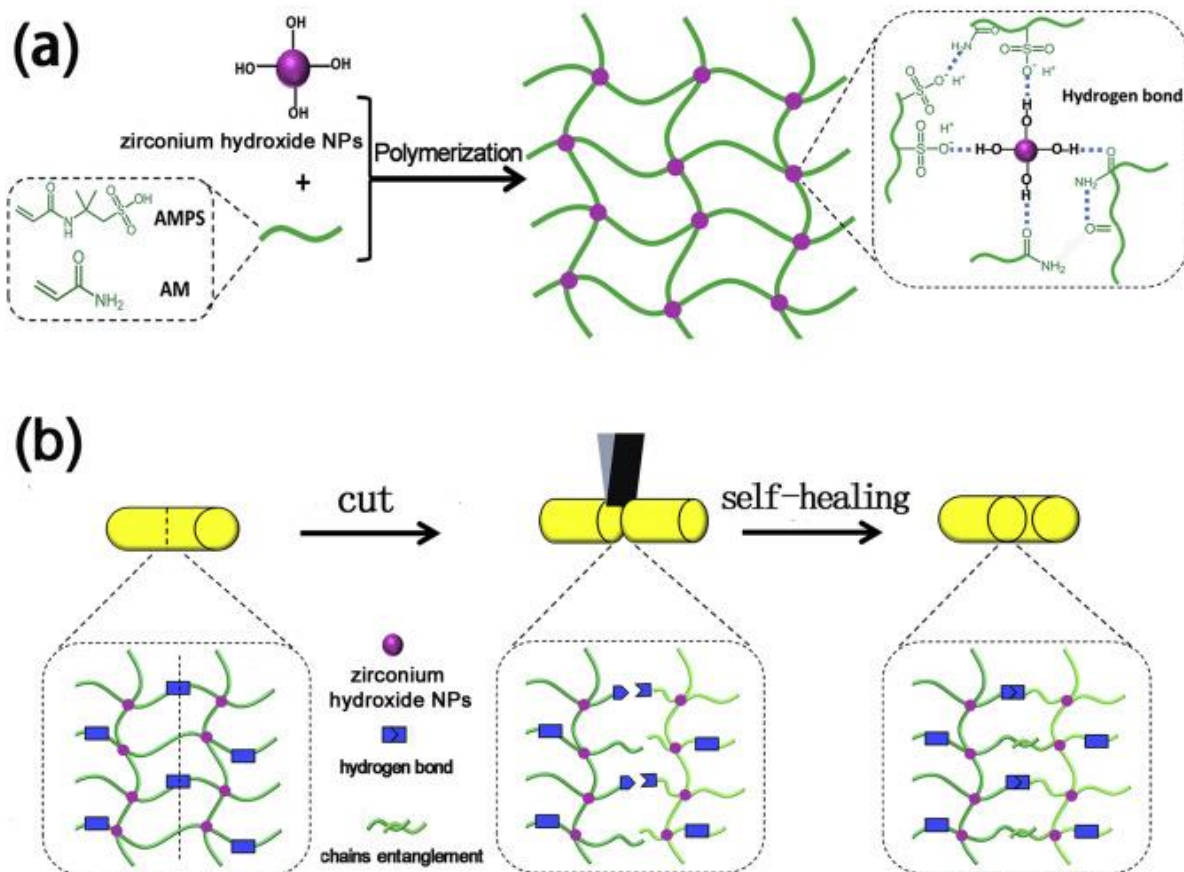


Figure 7: Schematic representation of hydrogel formation and the subsequent self-healing ability through reversible hydrogen bonding. a) Hydrogel formation through copolymerisation of 2-acrylamido-2-methyl propane sulfonic acid and acrylamide. b) Self-healing mechanism based on the breaking of hydrogen bonds upon fracture and reformation of hydrogen bonding on healing.

Physical interactions between the interfaces of a crack are a different approach to the development of intrinsically self-healing materials. For various polymers, chain entanglement due to intermolecular diffusion has been exploited successfully. Often however this involves the input of a little energy into the system in order to initiate the healing process.^{66,67} For example, heating the amorphous glassy polymers to the glass transition temperature allows for chain diffusion to occur and therefore heal cracks.⁶⁸ To reduce the glass transition temperature and facilitate chain diffusion, the interface of the crack can be wetted with solvent such as methanol or ethanol.^{69,70} The use of methanol to facilitate crack healing in poly(methyl

methacrylate) PMMA was shown that the full mechanical strength could be recovered.⁶⁹ Ideally however, crack healing would be achieved autonomously without the need for intervention after crack formation has occurred.

1.2.2 Extrinsic self-healing

Extrinsic self-healing mechanisms are possible due the addition of a self-healing component material being added to the polymer matrix.⁵⁸

The first instance of an autonomous self-healing material, as described by White *et al.*⁷¹ was an extrinsic system, in which microcapsules containing the healing agent dicyclopentadiene were embedded into a polymer matrix that contains Grubbs catalyst. On crack propagation, the microcapsules would rupture resulting in the healing agent filling the crack, when coming into contact with the embedded catalyst, polymerisation would occur (Figure 8). Many other systems involving various combinations of strained ring monomers and Grubbs catalyst, which exploits a ring opening metathesis mechanism, were developed from this initial design.^{72,73}

The size of microcapsules utilised in extrinsically self-healing systems can an range from a few micrometers⁷⁴ to a few hundred micrometers⁷⁵. Generally larger mcircapsules can heal larger cracks (as they contain higher amounts of healing agent). Small capsules (below 75 μm) struggle to heal crack damage and are mostly limited to the coating applications.^{76,77}

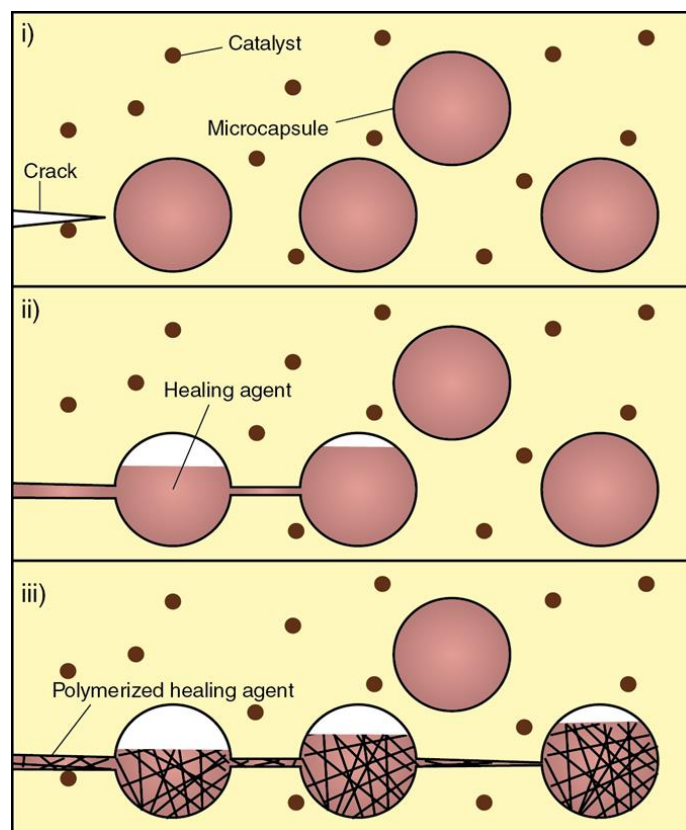


Figure 8: The mechanism for the first autonomous extrinsically self-healing material developed by White's group involving the Grubbs catalyst induced ring opening metathesis polymerisation.⁷¹ i) Crack propagation. ii) Rupture of capsules and release of healing agent. iii) Polymerisation and healing of crack.

As well as the microcapsule design, materials with microvascular networks that contain the healing components have also been developed. Examples of extrinsically self-healing polymer composites are provided in Table 4. For example, materials have been created that have two isolated networks embedded within, one containing epoxy resin and the other an amine based curing agent. On fracture, the components are released, and the crack faces are bonded closed. It has been shown that this system can heal a single crack multiple times, with mechanical testing showing up to 70% healing efficiency (although there was depletion of healing efficiency when observed over multiple cycles).⁷⁸

Table 4: Summary of extrinsically self-healing polymer composites.

	Healing Mechanism	Healing efficiency	Healing conditions	Host material	Ref.
<u>Micro capsule-based systems</u>	<i>(Embedded catalyst)</i>				
	DCPD + Grubbs	75-100%	10-48 hours, RT	Epoxy	71,79-81
	DCPD + WCl	20-65%	24 hours, RT	Epoxy	82,83
	<i>(Solvent Welding)</i>				
	Epoxy + Solvents	82-100%	24 hours, RT	Epoxy	84-86
	Anisole	89%	72 hours, RT	PMMA	87
	Dibutylphthalate	Barrier recovery	72 hours, RT	PMMA	77
<u>Vascular-based systems</u>	DCPD + Grubbs	70	12 hours, RT (7cycles)	Epoxy	56,78
	Epoxy + Hardner	60-90%	48 hours, 30°C	Epoxy	57,88
	Two stage healing polymerisation steps	62% mechanical damage	Hole filled in 20 min, 3 hours, RT (for mechanical damage)	PMMA	89

The development of extrinsically self-healing materials which consist of a single embedded component would be attractive, the simpler design would make the materials easier to process. Ideally, the mechanism should also forgo the use of expensive catalysts in order to be commercially viable.⁹⁰ One such mechanism, solvent welding, is discussed here.

1.2.3 Solvent welding

In the section 1.2.1, an intrinsic self-healing mechanism involving the exploitation of polymer chain diffusion and entanglement was discussed, including the addition of a solvent that could increase the efficiency of this system.⁶⁹ By combining this intrinsic self-healing mechanism

with the embedded microcapsule concept from extrinsic self-healing mechanisms, an efficient autonomous solvent welding mechanism was proposed (Figure 9).

For solvent welding mechanisms, a popular *in-situ* microencapsulation technique for self-healing components was developed by Brown *et al.*⁹¹ to yield microcapsules with urea-formaldehyde (UF) shells, ideal in size and shell thickness distribution for use in self-healing polymers.⁹² The technique utilises an oil/water emulsion template with the selected self-healing component acting as the discontinuous phase. During synthesis, UF nanoparticles are formed in the aqueous continuous phase and precipitate at the droplet interface to form a solid capsule with a shell of UF. Previous work utilising solvent welding mechanism utilised methanol and ethanol as the solvents of choice, however these solvents are not easily encapsulated using the *in-situ* UF emulsion technique. Alternatives that possessed suitable hydrophobic qualities including, chlorobenzene,⁸⁶ phenyl acetate⁹³ and dibutyl phthalate⁷⁷ have been investigated. The addition of monomer or polymers to the solvent containing microcapsules has been shown to further improve the self-healing capability of this type of mechanism.^{87,93}

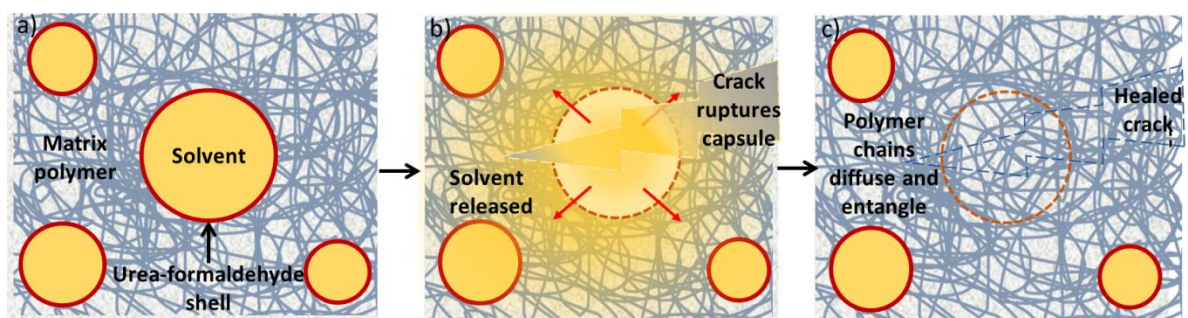


Figure 9: Mechanism for a solvent welding self-healing system which utilises a solvent encapsulated within a urea-formaldehyde shell embedded within a polymer matrix.⁹⁴ a) UF capsules with solvent cores are embedded within the polymer matrix. b) A crack ruptures the shell wall and the solvent core is released into the crack. c) The surrounding polymer chains diffuse and entangle which allows the crack to heal.

1.2.4 Demonstration and quantification of self-healing

The process of self-healing can be evidenced via several methods. Visual inspection, either through photos or microscope images of scratch or fracture healing, is an easy way of ‘showing’ the self-healing capability of a material (Figure 10).^{77,95,96} Surface profiling techniques have also been employed to measure the decrease in the depth of grooves/scratches after self-healing has taken place.

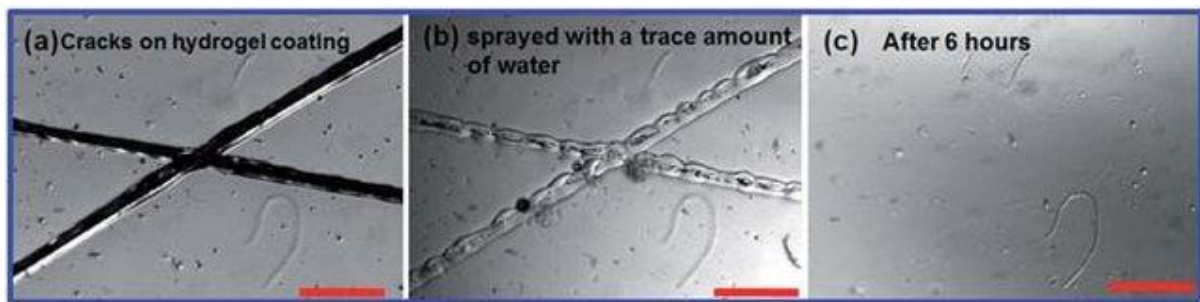


Figure 10: Optical images showing the self-healing process of a hydrogel coating.⁹⁷

Alternatively, the quantification of extrinsically self-healing composites is often defined through the comparison of the mechanical properties of the virgin polymer and that of the healed polymer.⁹⁸ A common method of utilising this definition for extrinsic self-healing materials was developed by White *et al.*,⁷¹ and concerns the testing of the fracture toughness of the healed and the virgin material and expressing as a ratio as shown in Equation 1. Where Kc is the fracture toughness (N). This method has been successfully utilised to demonstrate self-healing ability throughout the literature.^{99,100}

Equation 1

$$\text{Healing efficiency \%} = \frac{Kc_{\text{Healed}}}{Kc_{\text{Virgin}}} \times 100$$

For intrinsic self-healing materials, simple rectangular samples are often utilised in tensile tests.^{101,102} Due to the elastic nature of such materials, the healed samples composing of two fractured parts of sample can be simply pushed back together and left to heal before being tested in the same fashion, Figure 11.

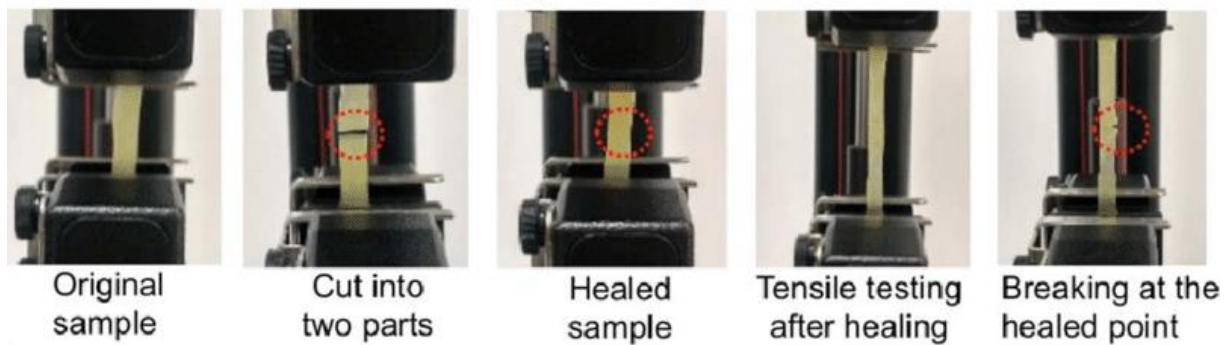


Figure 11: Intrinsic self-healing material undergoing tensile testing.¹⁰² A comparison of the tensile strength of the virgin vs the healed polymer can be made to indicate self-healing efficiency of the polymer.

For extrinsic self-healing materials the lack of matrix fluidity (as opposed to the gel/elastomer characteristics seen in common intrinsic self-healing materials) means that the damage interfaces need more assurance that they will remain in close contact during healing. Also due to the more brittle nature of such materials, in order to achieve accurate fracture toughness measurements of the virgin and healed samples, the direction of crack propagation needs to be consistent and crack length needs to be monitored due to the dependence of critical stress (the load at which crack propagation occurs) on these parameters. Over time, a more complex sample geometry was therefore developed for fracture toughness testing of extrinsically self-healing materials.¹⁰³ The tapered double-cantilever beam (TDCB) sample geometry (Figure 12) has a constant critical stress along the centre line of the sample-regardless of crack length. A useful characteristic as this allows for comparative fracture toughness measurements to be

taken for a sample in the virgin and healed state without the need to ensure that crack length is the same.^{99,104}

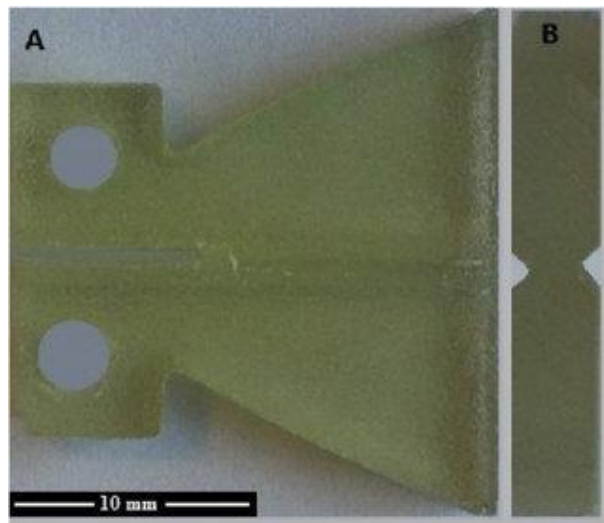


Figure 12: An example of a self-healing specimen using the TDCB geometry.¹⁰⁵ a) The tapered shape means that the critical stress of the sample is the same along the centre line, regardless of crack length. b) End on view displaying the 45° angle groove along the centre line of the sample.

The constant critical stress of the sample along the centre crack, regardless of crack length is due to the tapered structure of the samples; side grooves along the centre line of the sample at a 45 ° angle are also utilised as this promotes linear crack propagation without compromising the unique characteristics of this geometry (Figure 13).¹⁰⁶



Figure 13: TDCB samples that have undergone loading tests to failure, showing the importance of the central groove for these specimens.⁹⁹ On the right is a sample without the 45° centre groove which shows deviation of the crack from the centre line. On the left is a sample with the centre groove which shows that crack propagation follows the centre line. The critical stress of the sample remained the same along the length of the crack for a certain length (between 20 and 40 cm).

Before undergoing testing, a small pre-crack is introduced at the head of the groove and the sample undergoes loading tests in order to allow the crack to propagate through the sample. The crack will be allowed to propagate to a set length along the sample, generally between 20-40 cm.⁷⁹

Kc is proportional to the critical stress, P_c , (N) (the stress at which crack propagation is promoted) for TDCB specimens, (Equation 2). Where α is a geometric constant dependant on the geometry and the material of the sample. The TDCB geometry is very useful as, in the case of α being unknown for a new material, P_c can be substituted in place of Kc in Equation 1,¹⁰⁷ to calculate healing efficiency, as α is essentially cancelled out, Equation 3.

Equation 2

$$Kc = \alpha P_c$$

Equation 3

$$\text{Healing Efficiency} = \frac{\alpha P_{C_{\text{Healed}}}}{\alpha P_{C_{\text{Virgin}}}} \times 100 = \frac{P_{C_{\text{Healed}}}}{P_{C_{\text{Virgin}}}} \times 100$$

The use of fracture toughness recovery is therefore a well-established method of self-healing quantification. The potential applications of self-healing polymers is discussed in section 1.2.6.

Despite the niche application of the TDCB geometry to the quantification of self-healing properties, the information gained on the materials properties is limited (Young's modulus cannot be gained). Therefore, traditional geometries such as the rectangular 'dog bone' geometry would still be required to gain this information.

1.2.5 Introduction to crack propagation

In order to understand why the TDCB geometry has constant P_c regardless of crack length, it's important to take a look at simple crack propagation theory. (Figure 14) This section will focus on Mode 1 fracture (tensile stress) for crack propagation and will model brittle materials-similar to the polymers often used for extrinsic self-healing materials.

First we must consider the two competing forces determining crack propagation, the force required to break the chemical bonds of the material generating two new surfaces (the surface energy). And the strain energy released by the surrounding material upon unloading from the stress. The strain release occurs within the volume of material surrounding the crack and has a quadratic dependence on crack length. Eventually, the energy released by further crack growth dominates the surface energy and crack propagation becomes spontaneous as the system can continue lowering its energy by further crack growth.¹⁰⁸

This energy-balance approach was first described by Griffith and describes a key relationship between the crack length and the critical stress required for crack propagation.¹⁰⁹

As previously stated, the TDCB geometry was specifically developed to achieve a constant critical stress over a range of crack lengths. The tapered sample shape ensures that the strain release within the volume of material surrounding the crack grows linearly (as opposed to quadratically) with crack length. This removes the dependence of critical stress on crack length over that range.

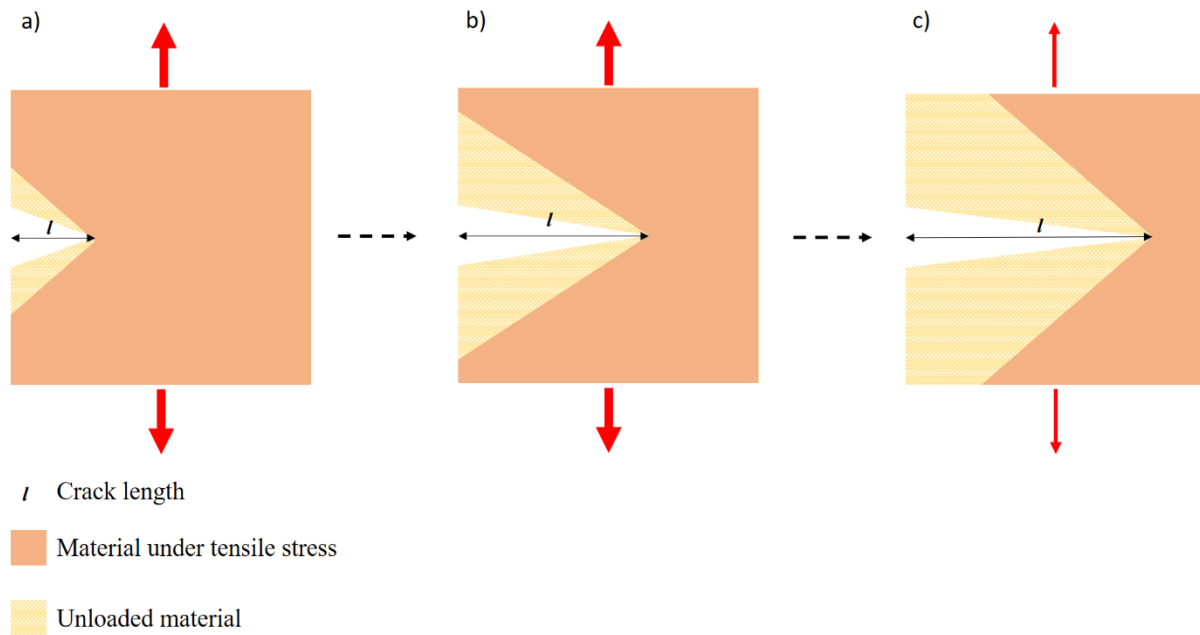


Figure 14: Schematic showing the dependence of crack growth on crack length in brittle materials undergoing Mode I fracture. a) At small crack lengths, crack propagation is dominated by the force required to open the crack, due to the increase in surface energy. A small amount of energy is released as the material surrounding the flanks of the crack become unloaded. b) As crack length grows, the energy released grows quadratically with crack length and begins to compete with the opposing force required to overcome the surface energy. c) At longer crack lengths, the energy released due to crack growth dominates the required energy to overcome the surface energy and crack growth becomes catastrophic.

1.2.6 Applications

Many different materials have been investigated for the development of self-healing systems. Self-healing ability increases the lifespan of materials which reduces the cost of long-term use applications and is useful for applications where manual intervention for repair purposes is difficult. Ceramics and concrete have been investigated.^{110,111} One example is the use of bacteria-laden capsules embedded within concrete. The bacteria will become activated if water

permeates through the cracks, where they start to precipitate CaCO_3 , which seals the crack surface.¹¹¹ Self-healing coatings is a key application with scratch reduction and anticorrosion properties being driving factors for development.^{112,113}

As well as improving the lifespan of materials, the addition of self-healing components can lead to the development of composite materials with additional functionality. Functionalised polymer chains have also been used to produce a self-healing materials with additional functionality, an example of which is the use of graphene modified polymers to produce self-healing materials and improve mechanical strength of the composite in comparison to the unmodified material.¹¹⁴ For extrinsic self-healing polymer composites, the addition of fibres¹¹⁵ or microcapsules¹¹⁶ has also proven to induce a toughening effect for the material as well as adding self-healing functionality. Polymers are by far the most widely studied materials⁵⁸ due to their easy processability and the huge range of polymers available.

1.2.7 Transparent self-healing materials

An optically transparent self-healing would be appealing as this would allow for their use in a wider range of applications such as optics and also improve the aesthetic quality of the material. There are examples of intrinsically self-healing transparent materials but the gel-like quality of these materials^{117,118} limits the applications to areas where robust structural properties are not required.(Figure 15)

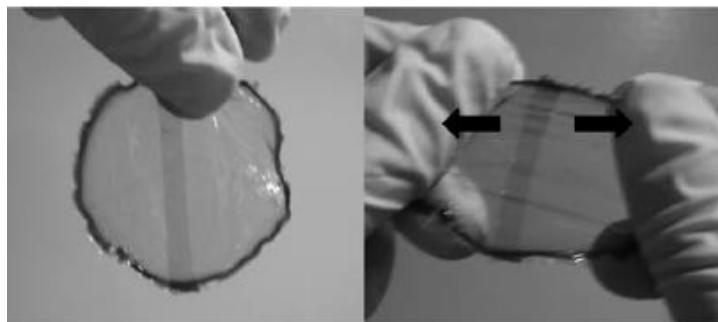


*Figure 15: Transparent intrinsic self-healing elastomer polymer.*¹¹⁸

An extrinsically self-healing transparent material was generated by Jackson *et al.*⁷⁷ This was achieved through utilisation of a solvent welding mechanism and refractive index (RI) matching of the PMMA polymer matrix with the corresponding self-healing core material. The microcapsules however were produced using the Brown method⁹¹ which of course produces non transparent UF shell capsules. It has been shown, that by using very small capsules (which will produce far less light scattering effects) an optically transparent self-healing materials could be produced.⁷⁷ Although, the use of smaller capsules as discussed above limits the self-healing ability of the material⁷¹ and as a result, this example was only shown to recover scratch damage to the coating, (Figure 16) with no recovery of mechanical strength from fracture shown.

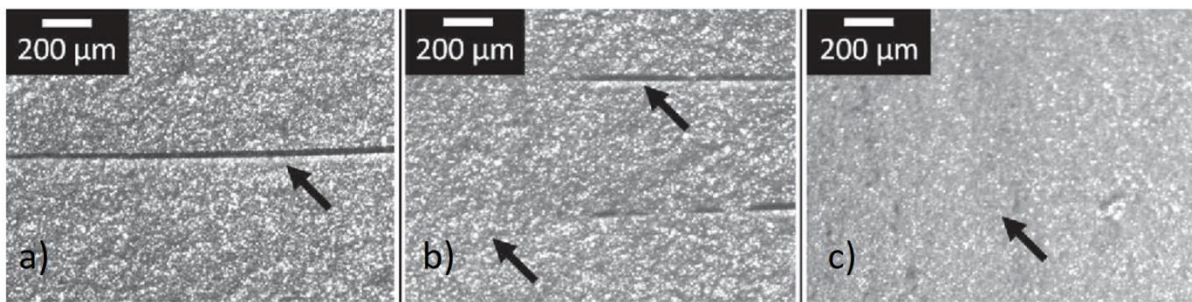


Figure 16: Reflected optical microscope images showing the healing ability of a transparent coating after 72 hours healing time. a) PMMA only b) 10 wt% 1.5 μm capsules and c) 6wt% 75 μm capsules. Larger capsules showed better healing of scratches of the coating but the UF Particles on the surface of the capsules limited the ability to test larger capsules.

1.2.8 Refractive index matching for transparent composites

For transparent materials, light can travel through the air, pass into this material and through to the air again. As rays of light pass through mediums of differing densities the speed at which the light moves can change. The RI of a material describes the ratio of the speed of light in a vacuum over the speed light when passing through the material. This results in RI value being

inversely proportional to the speed of light through that medium with air essentially being equal to 1.

Light travelling perpendicular to the material interface will change speed as it passes through the material but the path of light will not change, if the light hits the interface of the material at any other angle the path of light will change – this is refraction of light through a transparent medium (Figure 17a).

For composite materials, light is no longer passing through only an air/ material and then material/air interface. If the materials within the composite have different RI values, the path of light can be drastically affected by the sequential refraction steps as the light passes through the material causing a large amount of light scattering (Figure 17b).

If the composite is comprised of materials which have more closely matched RI values, the speed at which the light transmits through the material is similar and therefore refraction angle at the interface of the composite materials is drastically reduced and the resulting light scattering is minimalised (Figure 17c). This results in increased optical clarity of the final material.

This is why when designing transparent extrinsically self-healing systems ideally all the components need to have matching RI values. Modification of the PMMA self-healing system discussed in section 1.2.6 is a promising prospect for this work. PMMA is a transparent material with a similar chemical structure to SLA 3D printing resins, it is therefore likely they will have similar physical characteristics (including RI). Using a novel encapsulation method replacing the UF capsule shell with an RI match transparent material, could lead to a printable transparent material with larger capsules. Therefore, resulting in enhanced self-healing ability.

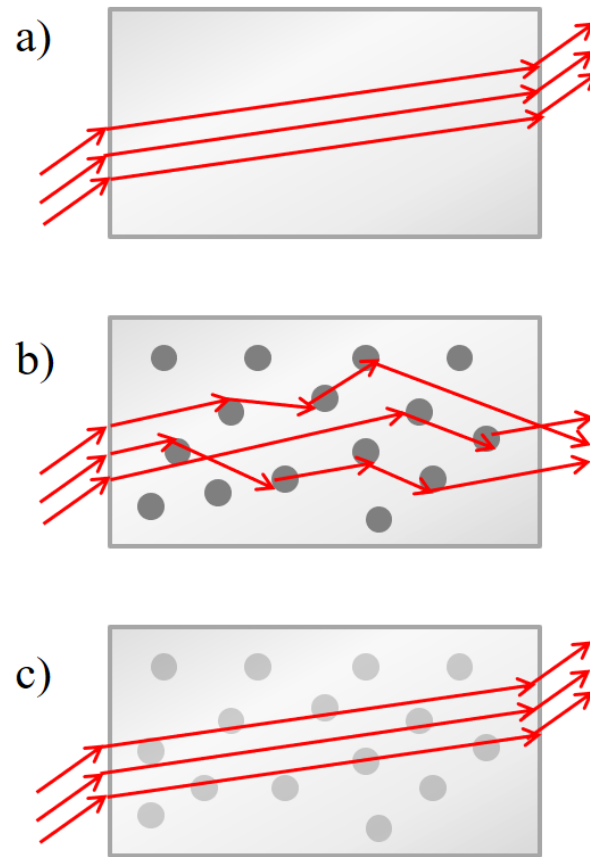


Figure 17: Schematic showing the refraction of light in different mediums, a) Single material. b) Composite material with components having different RI values. c) Composite material with components having the same RI values,

1.3 Capsule synthesis for extrinsically self-healing materials

For capsules based self-healing, the vesicle wall material needs to be considered to ensure the resulting capsules will be fit for purpose. Generally, the vesicle shell wall needs to be chemically/mechanically stable, adhere well to the matrix material, be non-porous or have limited leakage and respond to damage with release of core material.^{119–121}

Throughout the literature a number of techniques have been developed for the production of core-shell microcapsules for self-healing a compilation of which can be found in Table 5.

Table 5: Compilation table of microcapsule formation methods for use in extrinsically self-healing materials.

Shell wall material	Fabrication method	Ref.
Urea-formaldehyde	Oil in water emulsion polymerisation	71,87,91,122,123
PMMA	Solvent evaporation	124–126
Polyurethane	Interfacial polymerisation	74,113,127,128
Polyurea	Interfacial polymerisation using droplet microfluidics	129–131
Acrylate	Oil in water emulsion photo polymerisation using droplet microfluidics	132,133
Alginate	Interfacial polymerisation using droplet forming electro spraying	134

As outlined in section 1.2.2, a popular method for preparation of capsules for self-healing materials is using the urea-formaldehyde technique outlined by Brown *et al.*⁹¹ Urea-formaldehyde fits the ideal profile for the shell wall outlined above and as a result this technique has become a highly popular technique for encapsulation of self-healing cores. There are concerns over the toxicity of urea-formaldehyde which could limit the materials application

and the non-transparency means these materials are not ideal for applications which require optical transparency.

To overcome these shortcomings, microcapsules have been formulated with different shell wall materials. PMMA microcapsules have been fabricated using a solvent evaporation method.¹³⁵ Interfacial polymerisation is another popular method for development of new microcapsule synthesis. Polyurethane microcapsules synthesised using this method also raise health concerns due to the use of isocyanates during productions.¹³⁶

A promising area of investigation is in the incorporation of microfluidics for production of microcapsules for self-healing. The generation of droplets on microfluidic devices allows for the UV polymerisation of acrylate shells within the channel of the microfluidic device.^{132,133} Microfluidic devices produce a high level monodispersity compared to batch production and the high shear produced at within the device could be used to provide more control over high viscosity and non-newtonian fluids. Microfluidic devices for the production of microcapsules is discussed more section 1.4.

1.4 Droplet Microfluidics for vesicle generation

Microfluidic lab-on-a-chip devices are being increasingly utilised in smart material synthesis research.^{129,137-141} Through the use of micrometer sized channels or ‘pipes’, valves, mixers and pumps, these devices manipulate small volumes of liquid (nL or pL) to autonomously complete various tasks.¹⁴²

Lab-on-a-Chip devices can be fabricated from a range of materials including glass, poly(dimethyl siloxane) (PDMS) and PMMA.¹⁴³ Glass is an attractive choice where solvent resistance, high thermal stability or transparency are required.¹⁴⁴ Glass has a hydrophilic surface and therefore lends itself to supporting the formation of o/w droplets with an aqueous continuous phase. The glass surface can also readily be chemically functionalised as required.

When compared to traditional reaction vessels, advantages include a high surface area to volume ratio which is much larger than that in conventional reactors, controlled flow regimes of the reactants and solvents involved, short diffusion distances, efficient heat and mass transfer, safety factors and shorter reaction times.¹⁴⁵

Fluid flow is laminar, mixing controlled by diffusion, gives spatial and temporal control over reaction conditions and large surface area to volume ratios allow for surface based catalysis. Multiphase reaction mixtures are therefore of particular interest for microfluidic reactors due to the ability to tightly control interfacial behaviour of various phases.¹⁴⁶ Of particular interest is droplet microfluidics and the generation of uniformly sized vesicles.

Compared to batch processes for the production of emulsions, the high degree of control afforded by microfluidic devices allows for tight control over droplet size and droplet frequency.¹⁴⁷⁻¹⁴⁹ By variation of inlet positioning, phase flow rates and channel width ratios, a huge array of laminar^{150,151} and droplet^{152,153} flow regimes can be achieved.

The inclusion of elements such as serpentine bends within devices can also increase mixing within droplets formed, producing highly efficient miniscule reaction vessels within each droplet.^{147,152} Polymerisation of the droplets at the interface of the emulsion droplets allows for the production of microspheres with a high degree of uniformity.^{129,154} Exploitation of interfacial reactions and phase selective polymerisation has led to the production of structures such as microcapsules^{130,132} and microfibres.¹⁵⁵ These structures can be complex and contain hierarchical structures such as multi emulsion droplets¹⁵³ (Figure 18) and particles with multifunctional properties.¹⁵⁶ Droplets produced in this manner have been utilised in smart materials such as tissue engineering¹⁵⁷ and self-healing materials.¹²⁹

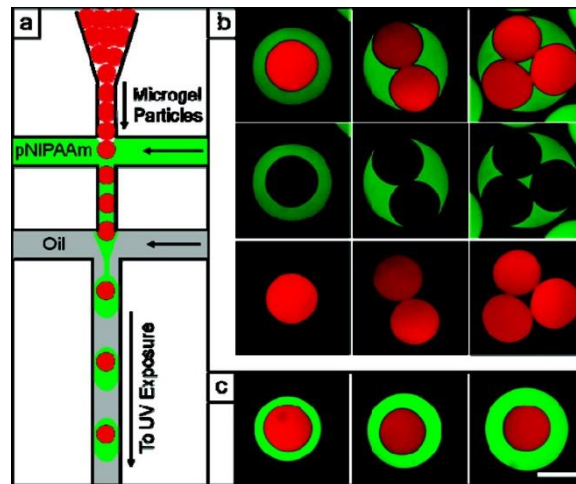


Figure 18: Example of a droplet microfluidic device being used to fabricate microgel capsules. The use of a microfluidic device allows for the creation of complex structures with a high degree of control.¹⁵⁸ a) Schematic of a microfluidic device forming aqueous poly(*N*-isopropylacrylamide) (pNIPAAm) droplets (middle green phase) that are loaded particles of a similar material, pNIPAAm or polyacrylamide (inner red phase). Adjusting the flow rates of the inner, middle and the outer oil phases controls the number of core structures in each shell (b) as well as the shell thickness (c).¹⁵⁹ Subsequent gelation of the pNIPAAm phase leads to microgels with a distinct core-shell architecture. (b, c)

1.4.1 Flow regimes in microfluidic devices

As mentioned in the previous section, the flow regime in microfluidic devices can be tightly controlled which is a key advantage for many applications. In large amounts of fluid, turbulence causes mixing with inertia being the controlling factor. On the micro scale however, viscous forces play a much larger role. The ratio of inertial to viscous forces is known as Reynolds number (Re).¹⁴² As a result, microfluidic systems which usually feature laminar flow patterns, are driven by low Re (<2000) (Figure 19).

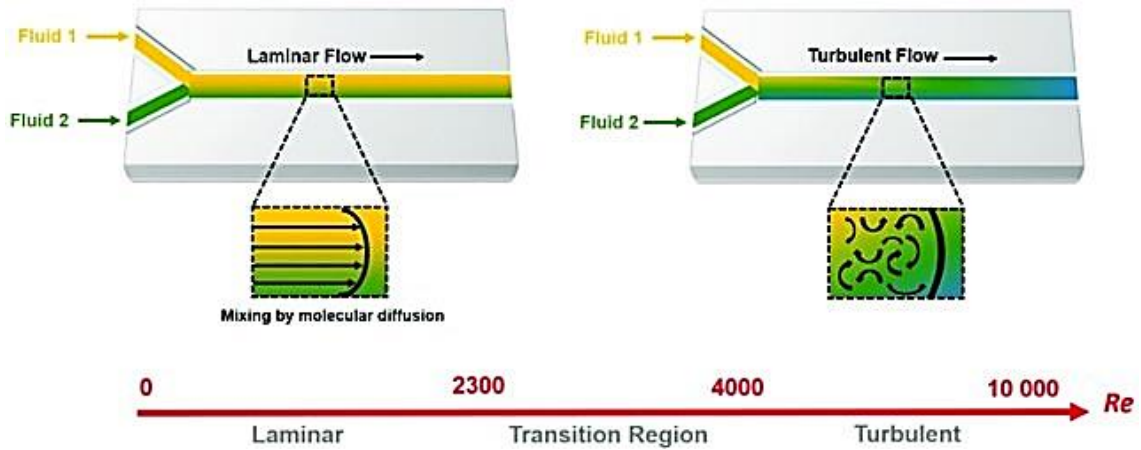


Figure 19: Schematic showing the transition from laminar flow at low Re numbers to turbulent flow at high Re values.¹⁶⁰

Re can be calculated using Equation 4, where ρ is density (kg m^{-3}), μ is dynamic viscosity ($\text{kg m}^{-1} \text{s}^{-1}$), r_h is the hydraulic diameter of the channel (m) and U is fluid velocity (m s^{-1}).

Equation 4

$$Re = \frac{\rho U r_h}{\mu}$$

The hydraulic diameter of the channel, m , can be calculated using Equation 5, A is area of the cross section of the channel (m^2) and p is the perimeter of the channel (m).

Equation 5

$$r_h = \frac{4 A}{p}$$

Within microfluidic devices with laminar flow regimes, when miscible fluids are utilised, the degree of mixing is therefore determined by diffusion.¹⁶¹ (Figure 20)

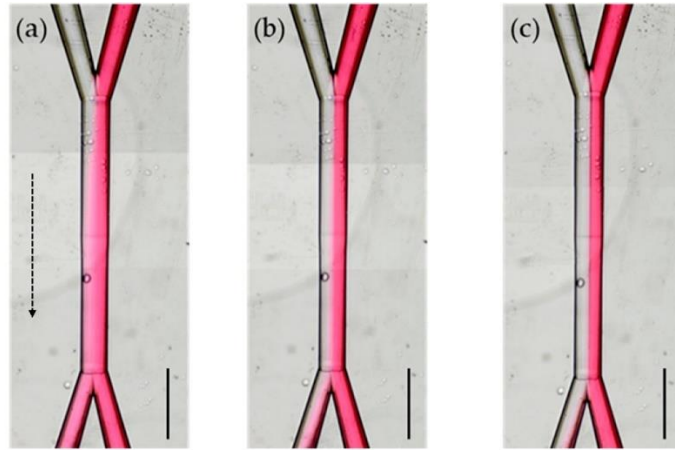


Figure 20: Optical images showing the mixing regime within microfluidic devices under laminar flow. Faster flow regimes (a) result in higher diffusion rates. Whilst slow flow regimes (c) show very little mixing due to slow diffusion rates.

When two or more immiscible fluids are used, through the exploitation of fluid junctions, droplets can be generated. For single emulsion droplet generation, a continuous phase and a dispersed phase are required. By adjusting flow rates and channel modification different size droplets of oil in water or water in oil droplets can be generated. Common junctions that are utilised in microfluidic devices for droplet generation are T-shaped junctions and fluid focusing junctions (Figure 21).

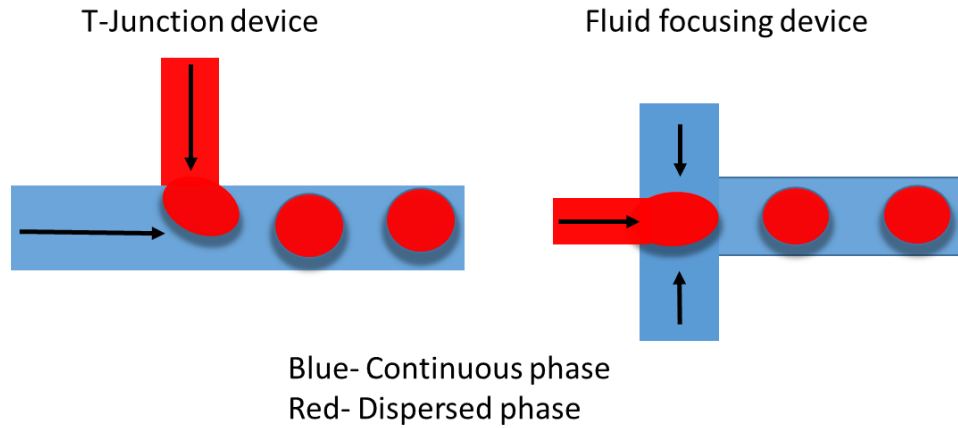


Figure 21: Droplet generation produced by T-junction and fluid focusing devices. Arrows represent the flow direction within the device.

Droplet generation is governed by inertial, viscous, gravitational and capillary forces. As mentioned above, at the microscale, mixing is dominated by viscous forces rather than inertia. By using small channel, capillary pressure is increased which in turn reduces gravitational effects. As a result, droplet generation is generally determined through a combination of viscous and capillary forces.¹⁴⁴ Capillary number, Ca , is a dimensionless number that is often used to determine droplet break off in microfluidic devices. It can be calculated using Equation 5, where μ , is viscosity of the continuous phase ($\text{kg m}^{-1} \text{s}^{-1}$), U is the velocity of the continuous phase, (m s^{-1}) and γ is the surface tension (kg s^{-2}) between the continuous and dispersed phases.

Equation 6

$$Ca = \frac{U \mu}{\gamma}$$

The size of droplets that can be produced from a single microfluidic device can therefore be varied widely. With only the chip dimensions and pressure capability of fixtures being the limiting factors. One key observation that can be made from the above equations and supported in the literature,¹⁶² is that if the continuous phase is kept constant, the flow rate of dispersed

phase is proportional to droplet size. Conversely, if the dispersed phase is kept constant, droplet size is inversely proportional to the flow rate of the continuous phase.

The flow behaviour inside of the droplets should also be considered. These flow regimes were first investigated by the Ismagilov group.¹⁵² In straight microfluidic channels, shear is generated at the liquid interface at the droplet front, this generates a steady recirculating flow. (Figure 22a) The ‘twirling’ effect seen as the droplet forms at the junction largely determines the amount of mixing within the droplet. Increasing the total flow rate of the regime causes faster pinch off, reducing the twirling effect and therefore reduces the amount of mixing that occurs within the droplet. (Figure 22b)

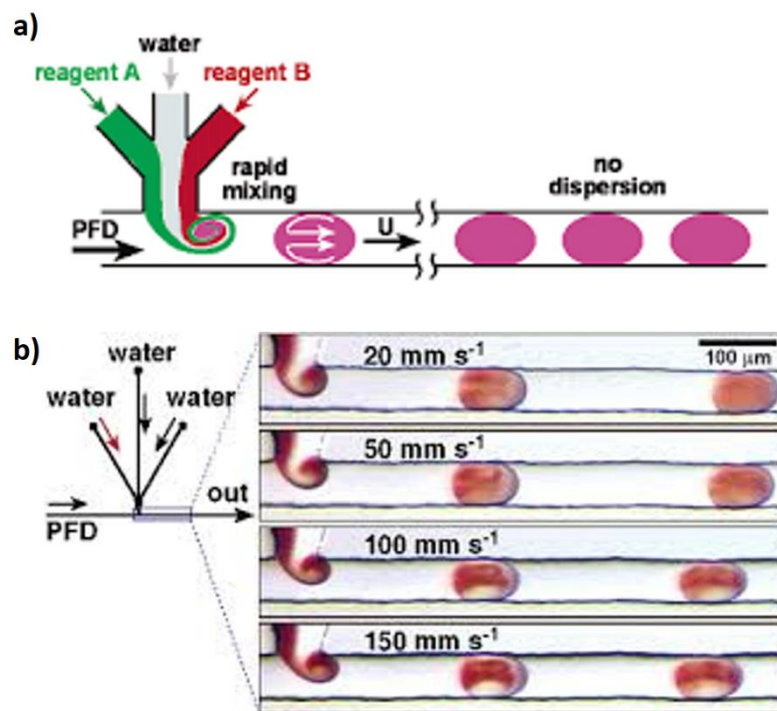


Figure 22: Mixing regime within droplets. a) Rapid mixing occurs at droplet formation. Detached droplets then undergo a steady recirculating mixing pattern. b) Mixing regimes of droplets highlighted by the use of dyed reagents. Increasing total flow causes faster droplet break-off. Thereby decreasing mixing efficiency.

The mixing in straight channels is therefore slow after the initial droplet break-off. Some applications require fast and chaotic mixing within the droplet for an extended period for reactant mixing. By changing the sample geometry enhanced mixing can be achieved, (Figure 23) with the inclusion of bends or serpentine channels causing more chaotic mixing within the droplets.

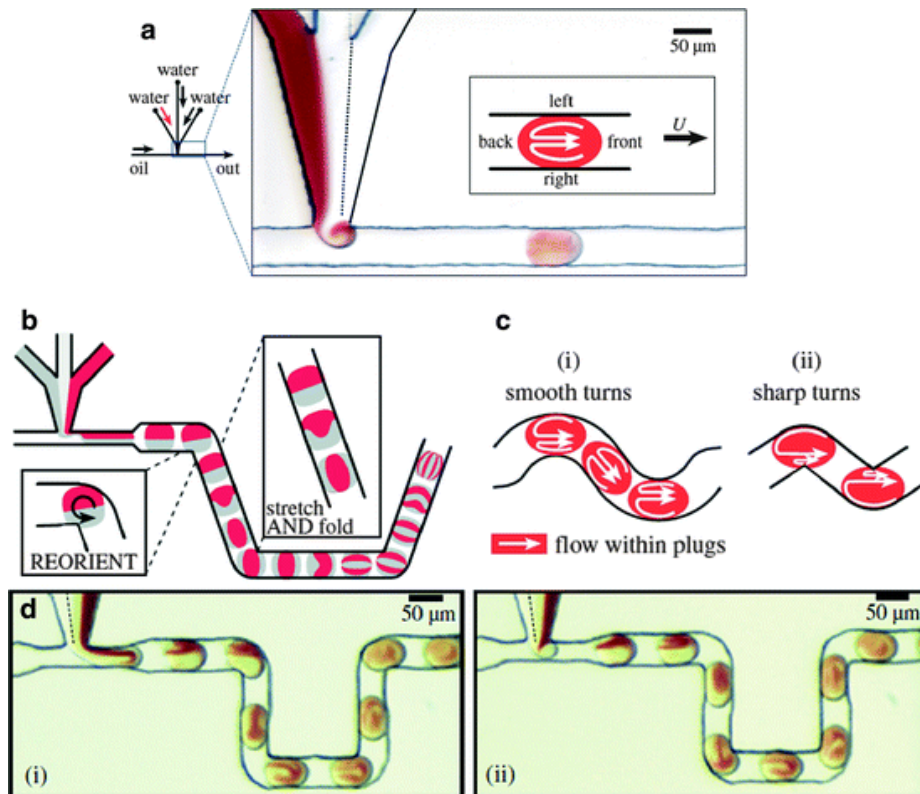


Figure 23: Different mixing regimes within droplets using different microfluidic device geometries.^{163,164} a) Steady recirculatory flow within straight channels. Stretch and fold mixing (b) and asymmetrical recirculation mixing (c) which can be generated in winding/serpentine channels. d) Optical images showing the use of winding channels to induce stretch and fold (i) and asymmetrical (ii) mixing.

1.4.2 Droplet microfluidics for materials generation

The applications for droplet microfluidics are wide and expanding.^{149,165} Some application such as digital droplet polymerase chain reaction (PCR) are already a standardised technique used in research laboratories, with commercial products already available.¹⁶⁶ For other applications,

the majority of research has been within biological and chemical analysis, with applications such as single cell analysis, medical diagnostics and drug discovery being summarised in regular and large review articles. A summary of applications for droplet microfluidics is shown in Table 6 with relevant review articles providing more in-depth discussion.

Table 6: Summary table of the state of the art for droplet microfluidic applications

Application	Ref.
Single Cell analysis	Review Papers, ¹⁶⁷⁻¹⁷⁰
Nucleic acid detection and analysis (Digital PCR)	Commercially available examples, Bio-Rad ddPCR systems, ^{166,171}
Medical Diagnostics	Review Papers, ¹⁷²⁻¹⁷⁴
Drug Discovery	Review Papers, ¹⁷⁵⁻¹⁷⁷
Food and agriculture analysis	Review Papers, ¹⁷⁸
Environmental analysis	Review Papers, ¹⁷⁹
Functional material synthesis	Review Papers, ^{180,181}

From the literature summary provided in Table 6, we have an overview of the research landscape within droplet microfluidics. Compared to other applications, functional material synthesis seems to be lagging. Application within the areas of functional material synthesis include, nanoparticle synthesis, drug delivery vesicles and microcapsule synthesis for composite materials. An overview of the application of droplet microfluidics for the production of functional materials is shown in Table 7.

Table 7: Summary of literature relating to material synthesis

Application	Examples/highlights	Ref.
Nanoparticle synthesis	Metal nanoparticles, Au, Ag	182,183
	Nanocomposites	184
	Metal-organic frameworks	185
Microstructure synthesis (For sustained drug delivery, catalysis, self-healing materials)	Drug delivery vehicles	186,187
	PLA microspheres with controlled porosity	188
	UV polymerised ethoxylated trimethyl-olpropane triacrylate microspheres	189
	Janus particles	190
	Microspheres for self-healing materials	131,133,191–193

Droplet microfluidic devices allows for tight control of the environment within the droplet for nanoparticle synthesis which in many cases has resulted in increased monodispersity when compared to traditional synthesis methods.^{194,195}

The biggest advantage however of using droplet devices for material synthesis is the ability to use the emulsion droplets as templates for the production of homogeneous spherical microparticles. Of particular interest for this work is the production of microspheres for self-healing materials. As discussed in section 1.4.1 droplets produced using these devices are more homogenous and could therefore aid in the distribution of capsules evenly throughout the polymer matrix. Production of droplets via these devices is also much more controlled and could provide a solution to problems encountered when trying to encapsulate certain materials via more traditional methods.

One such example, is the encapsulation of polyamine using a combination of microfluidic droplet technology and a batch mixer.¹³¹ The authors chose this approach as the high reactivity of polyamine and its solubility in both water and most organic solvents, means that stable emulsions are difficult to produce and therefore traditional methods prove challenging. By

utilising a microfluidic device to produce the template droplets within a co solvent before introduction to a reactive diisocyanate solution, polyurea capsules with polyamine cores were produced. (Figure 24) The polyamine capsules can be combined with epoxy core microcapsules to fabricate a dual capsule based self-healing system.

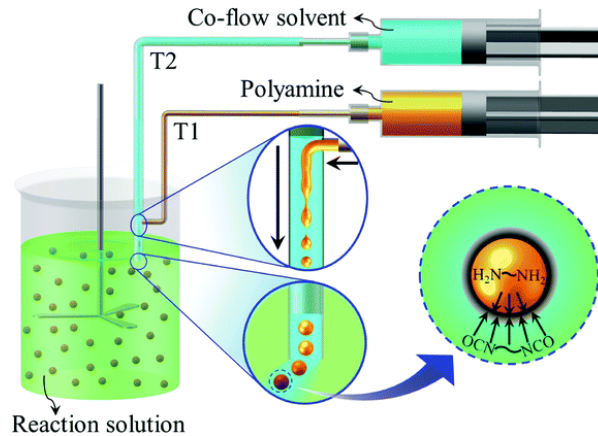


Figure 24: Schematic outlining the combination of a T-junction microfluidic device and a traditional batch mixer.¹³¹ Polyamine (T1) is used as the discontinuous phase within a T-junction device. The non-reactive co-flow solvent (T2) is used as the continuous phase. A non-polar solvent containing diisocyanate was utilised as the reaction solution. Upon exiting the T-junction device, the miscibility of the T2 solvent and the reaction solution allowed an instantaneous, interfacial polymerisation of the polyamine and diisocyanate to produce polyurea microcapsules.

Droplet microfluidic devices have also been utilised to produce multicomponent capsules which have both a healing agent, PDMS polymer base and a curing agent are present within the same capsule.¹⁹³ A double emulsion template was utilised, in which a PDMS polymer/silicone oil mixture and a PDMS curing agent were used as independent inner phases, a UV polymerizable triacrylate solution was utilised as the middle phase and an aqueous polyvinyl alcohol solution was used as the outer phase. Polymerisation of the middle phase produced capsules with two separate components for the two-part PDMS healing system. (Figure 25)

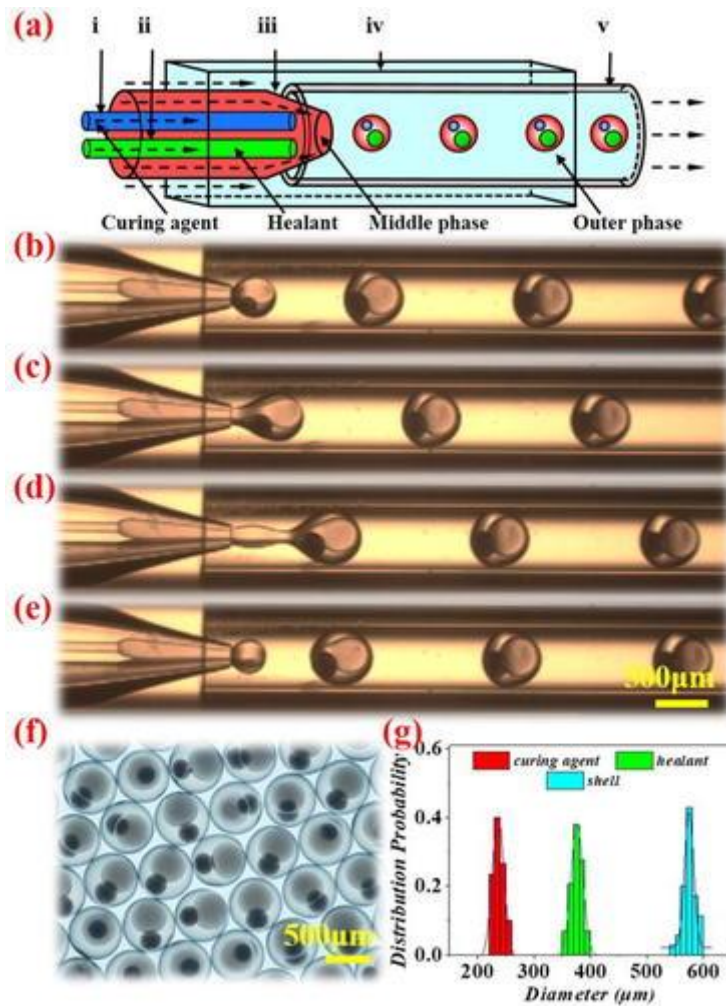


Figure 25: Schematic outlining the use of a droplet microfluidic device for the production of microcapsules containing a two-part healing agent.¹⁹³ a) Schematic showing the phase components within the microfluidic device. b-e) Evolution of droplet at the junction. f) Collected droplets containing both inner phases in separate compartments. g) Diameter distribution of the different components.

For the encapsulation of polymers for self-healing, microfluidic devices are a promising prospect. The viscosity of polymers is problematic when looking at their behaviour in microfluidic devices and is investigated in the next section.

1.4.3 Droplet generation using viscous liquids

The above theory on droplet generation within microfluidic devices, has been mostly generated using data gained from using fluids with low viscosities. The utilisation of viscous fluids such

as proteins, ionic liquids and polymers within micro-reactors means that more information on how higher viscosity liquids would behave in these devices is of interest.^{196,197} Early investigations into the effect of viscosity on droplet formation showed similar behaviour to that of low viscosity fluids, determining that droplet break off is dominated by Ca -however the viscous fluids investigated still had a relatively low viscosity of 18 mPa s.¹⁹⁷ More recently, liquids with viscosities of 1000-1214 mPa s, have been utilised, to ascertain whether the classic flow regime developed using lower viscosity fluids are suitable,^{196,198} with Bai *et.al.* determining that some universal assertions can be made. Droplet formation is highly dependent on the balance of shear stress and interfacial tension. Droplet size, as with low viscosity fluids, is still dependant on Ca .

1.5 3D printing of self-healing materials

The complex composite structures seen in nature have not been fully realised in 3D printing and the printing of functional materials and in particular self-healing materials is still in its infancy. This can largely be attributed to most current commercial applications driving research, such as dentistry, only require printing in a single material.

As a result, 3D printing of self-healing materials has been limited to intrinsic mechanisms with most of the current forecast of prospective self-healing materials for printing focusing on shear thinning gel materials.⁹⁶ Recently, self-healing gels were successfully printed that were formed by cross-linking benzaldehyde-functionalized poly(2-hydroxyethyl methacrylate) with ethylenediamine. The material showed self-healing properties of up to 98% after mechanical damage, which was possible due to dynamic imine bonds.⁹⁵ These intrinsically self-healing materials are tough and flexible but are limited due to their gel like characteristics without the ability to form tall, structurally complex constructions.

1.6 Project Aims

The aim of this project was to develop new materials for 3D printing which have additional functionality, specifically for self-healing. Previous examples in the literature concentrate on shear thinning gels with intrinsic mechanisms for self-healing but these materials have limited uses. Here the production of 3D printing resins which have embedded capsules is explored, which can be utilised in 3D printers for the production of microcapsule containing composites (Figure 26). These capsules contain solvents and polymers which can be used for self-healing, using the extrinsic self-healing mechanism of solvent welding. Several synthesis routes for the production of such capsules were explored, including the classic urea-formaldehyde capsules widely used in self-healing composites and their incorporation into SLA 3D printing resins. Furthermore, novel synthesis routes were investigated for the production of transparent self-healing capsules which are of great interest to UV-curable 3D printing resins due to their optically clear properties. The possibility of utilising microfluidic devices for the improved production of transparent microcapsules was also scoped.

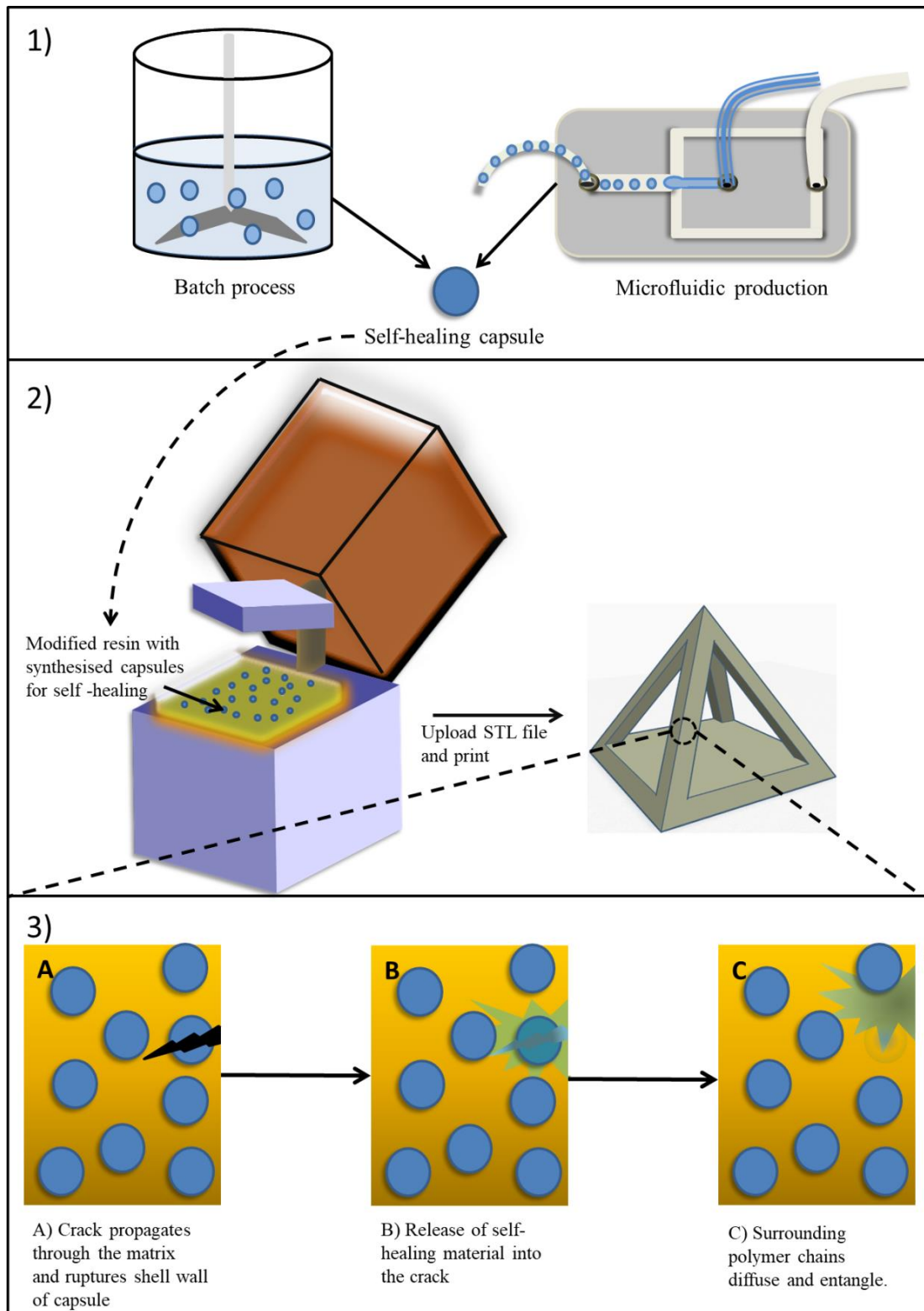


Figure 26: Overview of project aims. 1) A variety of capsules for extrinsic self-healing will be produced using either traditional batch or microfluidic routes. 2) Selected capsules will then be incorporated into 3D printable resins for the production of 3D printed structures. 3) Incorporation of capsules allows for the self-healing of micro-cracks in the material via a solvent welding mechanism.

2. EXPERIMENTAL

2.1 Chemicals

A list of all chemicals utilised during the research project and their respective suppliers can be found in Table 8. Aqueous solutions were prepared in double-filtered (0.05 m) water with a resistivity of 18.2 M Ω cm at 25 °C, obtained from an ELGA Option 4 that fed into an ELGA UHG PS water purification system (both devices from ELGA Process Water, Marlow Buckinghamshire, UK), unless otherwise stated.

Table 8: Chemicals and respective suppliers used within this body of work.

Chemical	Supplier
Solvents	
Anisole	Alfa Aesar, Heysham, UK
Ethyl phenyl acetate	Sigma-Aldrich, Dorset, UK
Acetone	Fisher Scientific, Loughborough, UK
Chloroform	Fisher Scientific, Loughborough, UK
Ethyl acetate	Fisher Scientific, Loughborough, UK
Toluene	Fisher Scientific, Loughborough, UK
Urea-formaldehyde encapsulation method	
Ammonium chloride (>99.5%)	Sigma-Aldrich, Dorset, UK
Formaldehyde (37 wt% in water)	Sigma-Aldrich, Dorset, UK
Poly(ethylene-alt-maleic anhydride) (100-500 kDa)	Sigma-Aldrich, Dorset, UK
Resorcinol (99%)	Alfa Aesar, Heysham, UK
Urea (>98%)	Alfa Aesar, Heysham, UK
Sodium hydroxide pellets	Alfa Aesar, Heysham, UK
Polymers	
Photocentric 3D Firm resin (mixture of (meth)acrylated monomers)	Photocentric Group, Peterborough, UK
Photocentric 3D Hard resin (mixture of (meth)acrylated monomers)	Photocentric Group, Peterborough, UK
Form Labs Resin Clear, Hard	RS Components, Corby, UK

(mixture of methacrylated monomers)	
Poly(methyl methacrylate) (~120 kDa)	Sigma-Aldrich, Dorset, UK
Polyvinyl alcohol (98-99% hydrolysed, high molecular weight)	Alfa Aesar, Heysham, UK
EPON 828 epoxy resin	Hexion, Peterlee, UK
Sylgard 184 (PDMS)	Farnell, Leeds, UK
Surfactants	
Sodium dodecyl sulphate (99 wt%)	Alfa Aesar, Heysham, UK
TWEEN 61	Croda, Goole, UK
Hexadecyltrimethylammonium bromide	Sigma-Aldrich, Dorset, UK
Chip Cleaning	
Propan-2-ol	VWR, Leicester, UK
Ethanol	VWR, Leicester, UK

2.2 In-situ encapsulation of self-healing materials with urea-formaldehyde shell

A variety of microcapsules with urea-formaldehyde shell walls were prepared using a method adapted from the method originally described by Brown *et al.*⁹¹ (Figure 27).

Briefly, urea (2.5 g), resorcinol (0.25 g) and ammonium chloride (0.25 g) were dissolved in a 0.5 wt% poly(ethylene-alt-maleic anhydride) solution (125 mL). The pH was adjusted to 3.5 by addition of a saturated sodium hydroxide solution. The solution was mechanically stirred with a 3-pitched blade propeller (d = 50 mm, bore = 8 mm, Cole-Parmer) at 400 rpm. The selected core self-healing component (30 mL) was added to the solution during stirring, with the resulting emulsion allowed to stabilise for 10 min. Formaldehyde solution (6.39 g) was added, the solution covered and heated for 4 h at 55 °C with the same stirring parameters. The resultant capsules were washed with acetone (3 x 5 mL) and filtered under reduced pressure and air-dried for 24 h to yield the free-flowing UF self-healing capsules. The desired size range was obtained by passing through 300 µm and 38 µm laboratory sieves.

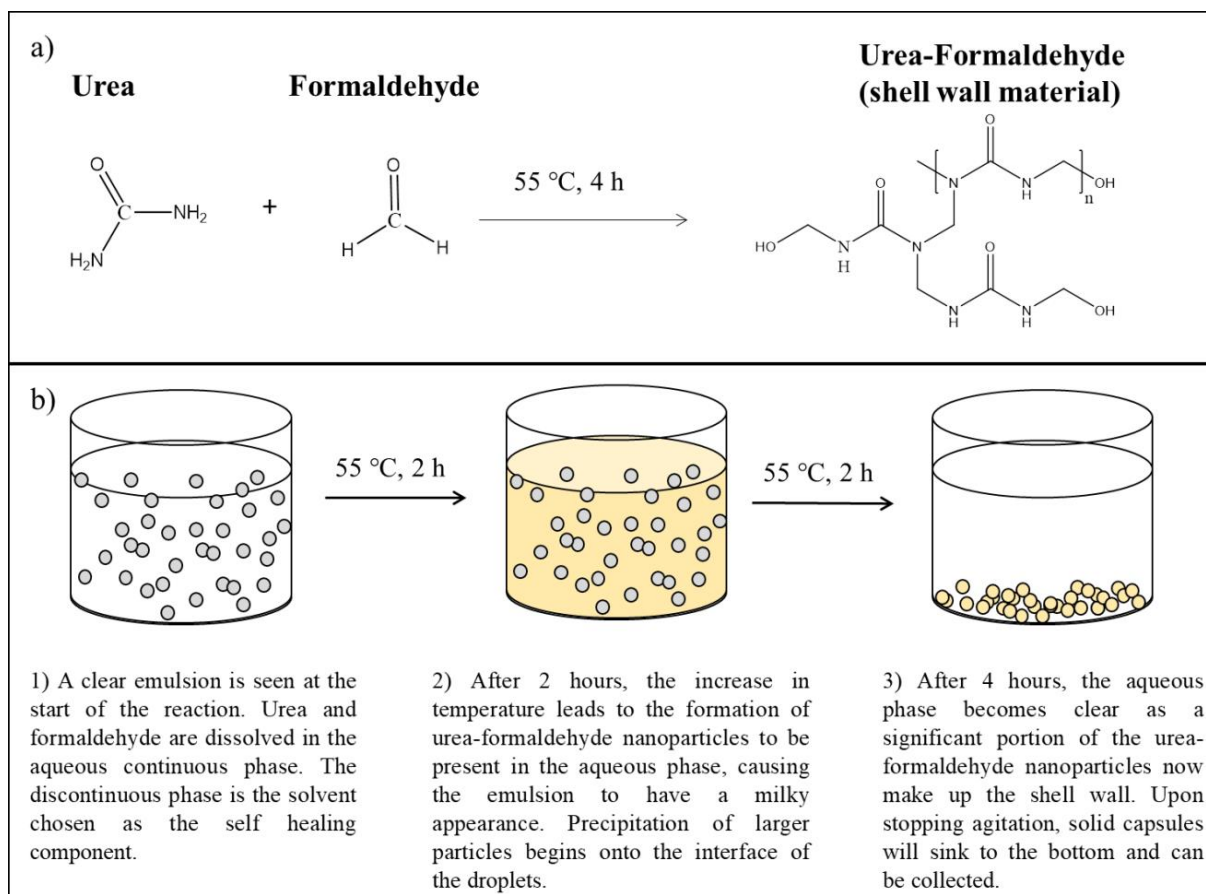


Figure 27: (a) Reaction scheme showing the formation of urea-formaldehyde which formed the shell wall. (b) Schematic showing the capsule formation steps.

2.3 In-situ encapsulation of self-healing materials with PMMA shell

A variety of microcapsules with PMMA shell walls were prepared using a solvent evaporation technique. This method utilised an emulsion template to achieve the spherical capsule shape. The continuous phase (CP) consisted of surfactant, sodium dodecyl sulfate, SDS, (10 g) dissolved in a 1 w% aqueous solution of polyvinyl alcohol (300 mL). The dispersed phase (DP) contained EPON 828 (3 g) and PMMA (1 g) dissolved in solvent (30 mL). Various solvents and ratios were investigated. The continuous phase (100 mL) was mechanically stirred with a 3-pitched blade propeller (d = 50 mm, bore = 8 mm, Cole-Parmer) at 400 rpm. The discontinuous phase was added to the solution during stirring and allowed to stabilise for 10 min. This concentrated emulsion was then added to the remaining continuous phase (200 mL) and the same stirring parameters were continued. The solution was heated to 40 °C to allow the solvent to evaporate (10-30 min). The capsules were then collected via filtration and centrifugation.

2.4 In-situ encapsulation of self-healing materials with commercial resin shell

A variety of microcapsules with a commercial UV polymerised resin as the shell walls were prepared using a UV polymerisation technique (Figure 28). An emulsion template was utilised, with the continuous phase comprising of deionised water (100-200 mL). Various surfactants and concentrations were investigated. The discontinuous phase consisted of commercial resin and liquid oligomer in various volume ratios (total volume of 5-10 mL). The discontinuous phase was added to the continuous phase with mechanical stirring utilising a 3-pitched blade propeller (d = 50 mm, bore = 8 mm, Cole-Parmer) at 400 rpm. The emulsion was allowed to form for 30 min before being irradiated with UV light for 20 min to instigate polymerisation of the resin to form the shell wall material. The capsules were then filtered and washed with water and isopropanol.

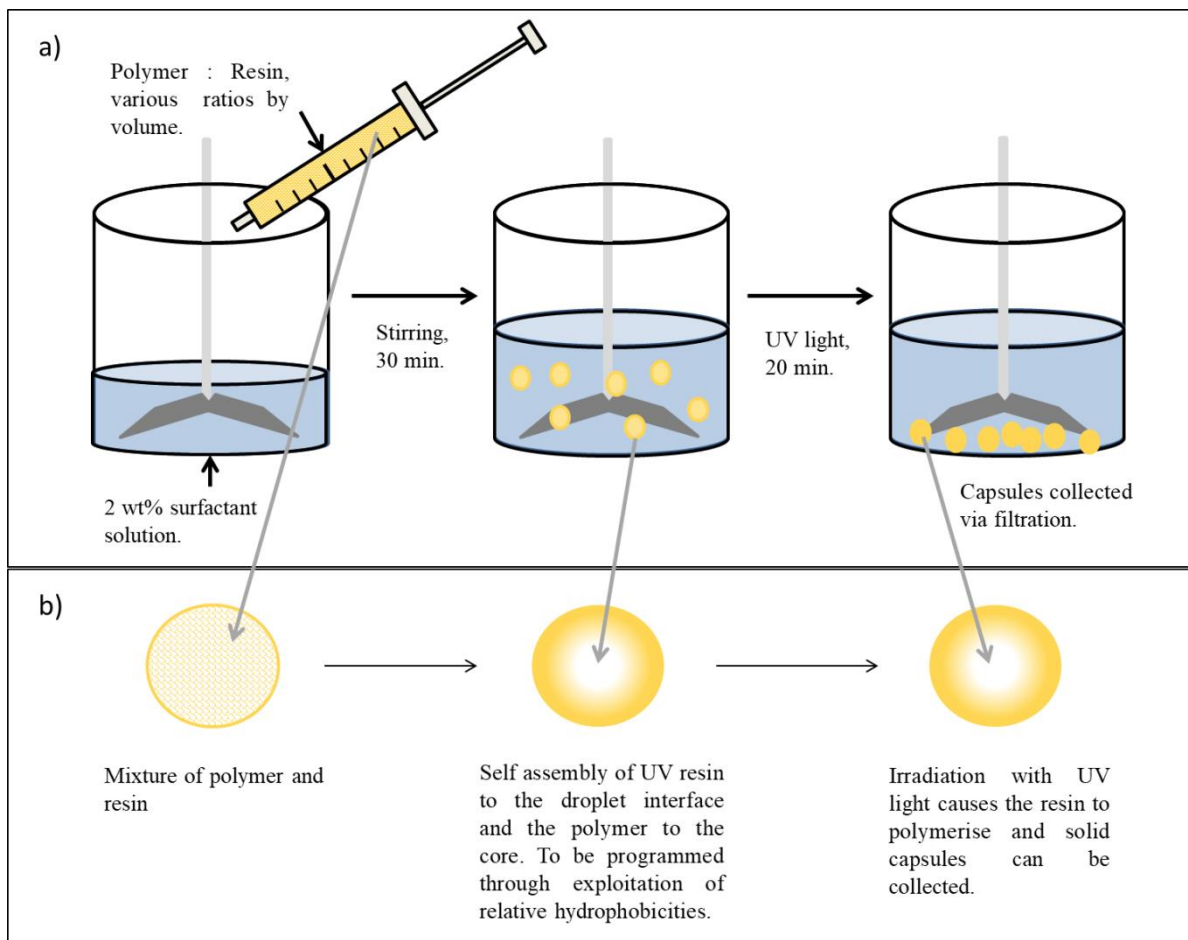


Figure 28: (a) Schematic representation of the UV polymerisation technique. (b) Schematic showing the assembly of the resin and polymer mixture within the droplet. The more hydrophilic polymerisable resin will migrate to the interface of the droplet while the more hydrophobic polymer will remain in the core of the droplet.

2.7 Preliminary healing agent plane welding screening tests

All proposed self-healing agents went through preliminary screening tests to identify their potential for use within the self-healing system. This was done through use of small 1 x 2 x 0.5 mm pieces of cured resin being used in ‘plane welding’ tests. Two pieces of the resin were coated with a thin layer of the proposed healing agent and then pressed together and left for 24 hours. If the polymer interface has sufficiently softened in order to achieve good bonding of the two pieces, then the screened agent was considered a good candidate to continue with the quantification of self-healing.

2.6 Preliminary studies for microfluidic droplet generation

Initial droplet studies were carried using the device MD1 (device details found in section 2.15.1). The continuous phase consisted of 2 wt% SDS in water. A few drops of blue food dye were added in order to enhance visualisation. The discontinuous phase was chloroform.

The discontinuous flow rate was maintained at $1 \mu\text{L min}^{-1}$ and the continuous phase was varied between 10 and $30 \mu\text{L min}^{-1}$. An optical microscope was used to capture images for size analysis (details outlined in section 2.8).

2.7 Generation of capsules for self-healing using droplet microfluidic devices

Devices MD2, MD3 and MD4 (device details provided in section 2.15) were investigated for use in production of self-healing capsules (Figure 29).

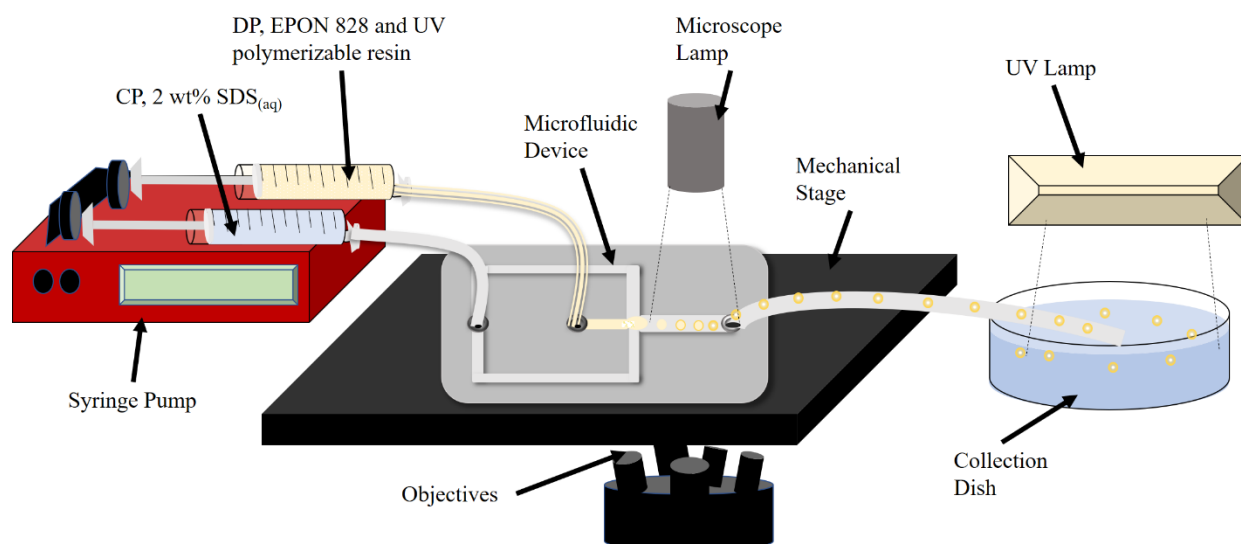


Figure 29: Schematic of the set-up utilised for the production of self-healing capsules. Syringe pumps were utilised to pump the CP, 2 wt% SDS (aq) and the DP, EPON 828 and UV polymerizable resin (in various volume ratios) into the microfluidic device to produce emulsion droplets. Droplet generation and size analysis was monitored using an inverted microscope. The droplets were polymerised upon exiting the device in a collection dish.

The CP consisted of 2 wt% SDS in water. The DP was a mixture of EPON 828 and Photocentric 3D printing hard resin in various volume ratios. The two phases were pumped into the microfluidic device using a syringe pump, New Era 300 Infusion Only pump (New Era Pump Systems, New York, United States). Droplet generation and size analysis was carried out using an inverted optical microscope (detail provided in section 2.8).

For MD2, polymerisation of the droplets occurred in the outlet tubing (more device details provided in section 2.15.1). For MD4, polymerisation of the droplets occurred in the device with continuous exposure to UV in the collection dish (more device details provided in section 2.15.2). Cardboard screens covered in aluminium foil were used to prevent exposure of the EPON : Resin mixture within the syringe from being exposed to the UV light source prematurely before emulsion has occurred. Polymerisation was achieved using a 12 W UV light source (XX-15S, Ultra-Violet Products Ltd, UK) at 365 nm wavelength. A thick black cloth was used to cover the experimental set-up and protect the user.

2.8 Microfluidic devices – Fabrication and interfacing

2.8.1 Glass microfluidic devices

All designs were created and drawn by myself unless otherwise stated using AutoCAD software. A range of device designs were employed, namely MD1, a T-junction based device for preliminary studies and MD2, a fluid focusing device for generation of droplets using the materials required for the self-healing capsules.

Design MD1 – The design featured a T-junction (discussed in section 1.4.1) for droplet generation with a long channel (10 mm) for the continuous phase and a shorter channel (5 mm) at right angle for the dispersed phase (Figure 30a). All channels were 200 μm wide. Chip devices with this design were fabricated from glass in house by Dr Iles using photolithography and wet etching.^{199,200} The MD1 device was etched to a depth of 50 μm . Inlet and outlet holes

of 300 μm diameter were drilled with an 1 mm diamond tipped tool on a CNC machine (Datron M7). Finally the channels were sealed by bonding to a blank glass wafer; this bonding was achieved by applying light pressure using weights and heating in a furnace to 570 $^{\circ}\text{C}$.

Capillary tubing (150 μm i.d., 363 μm o.d., Polymicro Technologies) was glued directly into the inlets holes using Araldite 2014 epoxy (Figure 30b). PEEK connectors (Upchurch Scientific, flangeless nut and ferrule system, for 1/16 o.d. tubing) were used for interfacing the capillary to a glass syringe (Figure 31). Polytetrafluoroethylene tubing (0.8mm i.d., 1.58mm o.d., Supelco) was used for the outlet. These devices had been designed for a previous project by another researcher, Dr Lu and were utilised in this project for preliminary studies on droplet generation.

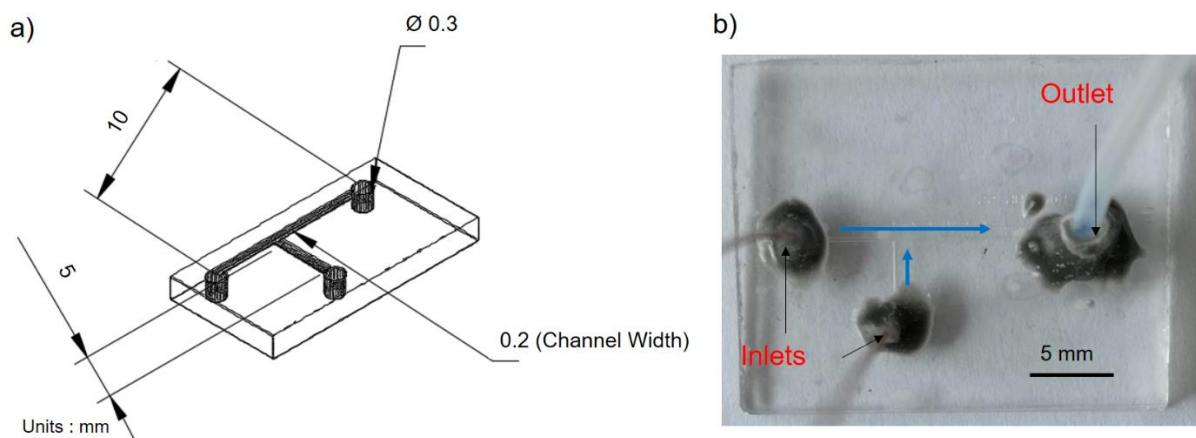


Figure 30: (a) Schematic design of preliminary device MD1 (Not to scale) (b) Photo of a glass device with design MD1 including the capillary inlet tubing. Blue arrows show the direction of flow within the device.

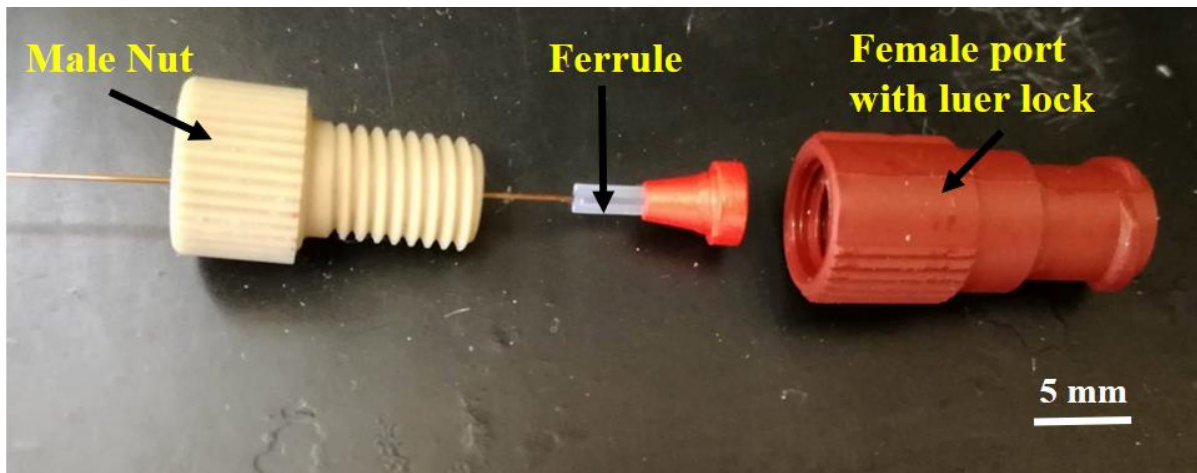


Figure 31: Components for the PEEK style connectors including ferrule and luer connector for attaching to syringes.

Design MD2 – The design featured a flow focussing junction (see section 1.4.1) for droplet generation (Figure 32). The three channels feeding the flow focussing junction were all 1 mm wide, merging into a 2 mm wide droplet channel. The devices were precision milled (Datron M7) in soda lime glass to a depth of 1 mm. Inlet and outlet holes were 3 mm in diameter. A photograph of a complete device is shown in Figure 32b. The devices were bonded to a flat piece of glass as outlined for MD1.

The MD2 devices were interfaced by first cutting syringe tips from the syringe body and inserting them into the inlet and outlet holes. TYGON tubing (i.d. 0.05 inch, o.d. 0.09 inch, Cole Parmer) was then inserted into the syringe tips. This created a ‘snug’ fit to minimise dead volume. The tubing was glued with Araldite 2014 epoxy to secure it in place (Figure 33). For interfacing the tubing with the syringes, barbed luer lock fittings (Figure 34) were used which were matched the internal diameter of the TYGON tubing.

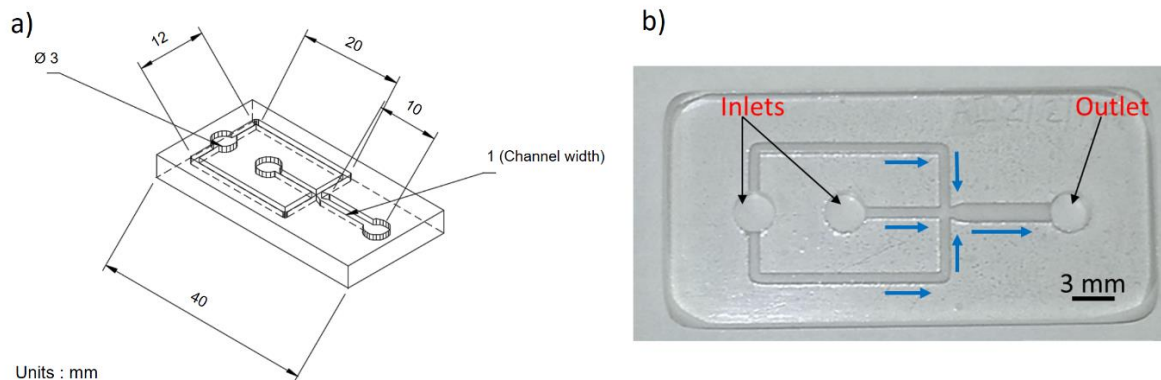


Figure 32: (a) AutoCAD drawing of design MD2 and (b) photo of fabricated MD2. Blue arrows show the direction of flow within the device.

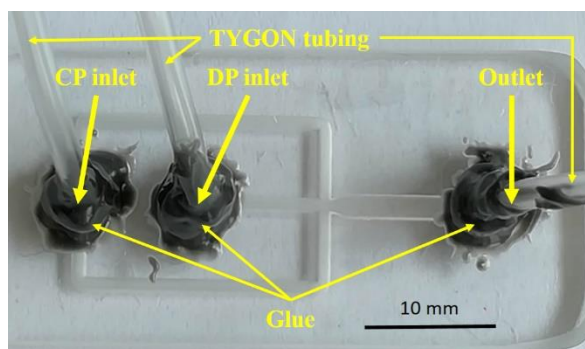


Figure 33: For both MD2 syringe tips that had been cut from the body of the syringe were inserted into the inlet and outlet holes. TYGON tubing was then inserted into the syringe tips to produce a snug fit. The whole thing was secured with araldite 2014.

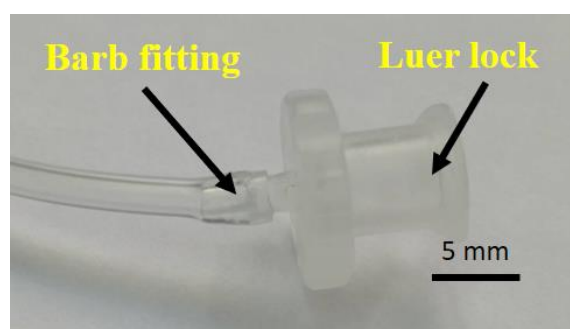


Figure 34: Barbed fittings that were used with the TYGON tubing. The fittings have a luer lock adapter for fitting syringes securely.

2.8.2 PDMS microfluidic devices

For PDMS devices, a mould was created via 3D printing. All mould designs were drawn using AutoCAD and then 3D printed using the Form 2, Formlabs printer. Formlabs, Hard resin was utilised. After printing, the moulds were placed in an oven at 60°C overnight to complete the curing process.

The design of MD3 is shown in Figure 35. The dimensions are the same as those for MD2. The inverse design shown in 38a was first 3D printed to serve as the mould. PDMS was poured into the mould and left to cure for 24 hours at room temperature to generate the device shown in Figure 35b.

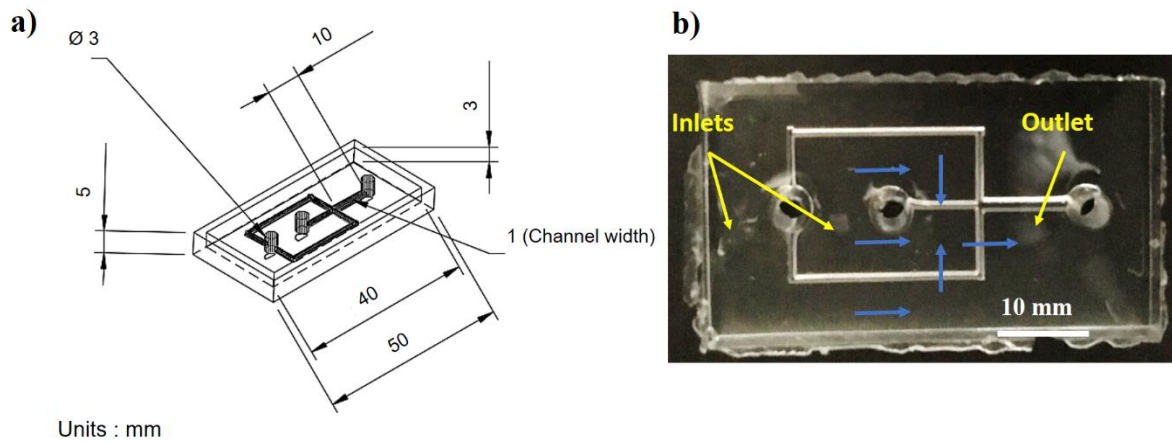


Figure 35: The design of MD3. a) CAD design of the 3D printed mould showing the dimensions. b) PDMS cast of MD3 created using the 3D printed mould. Blue arrows indicate the direction of flow in the finished device.

The design of MD4 is shown in Figure 36. The inverse design shown in Figure 36a was first 3D printed to serve as the mould. PDMS was poured into the mould and left to cure for 24 hours at room temperature to generate the device shown in Figure 36b.

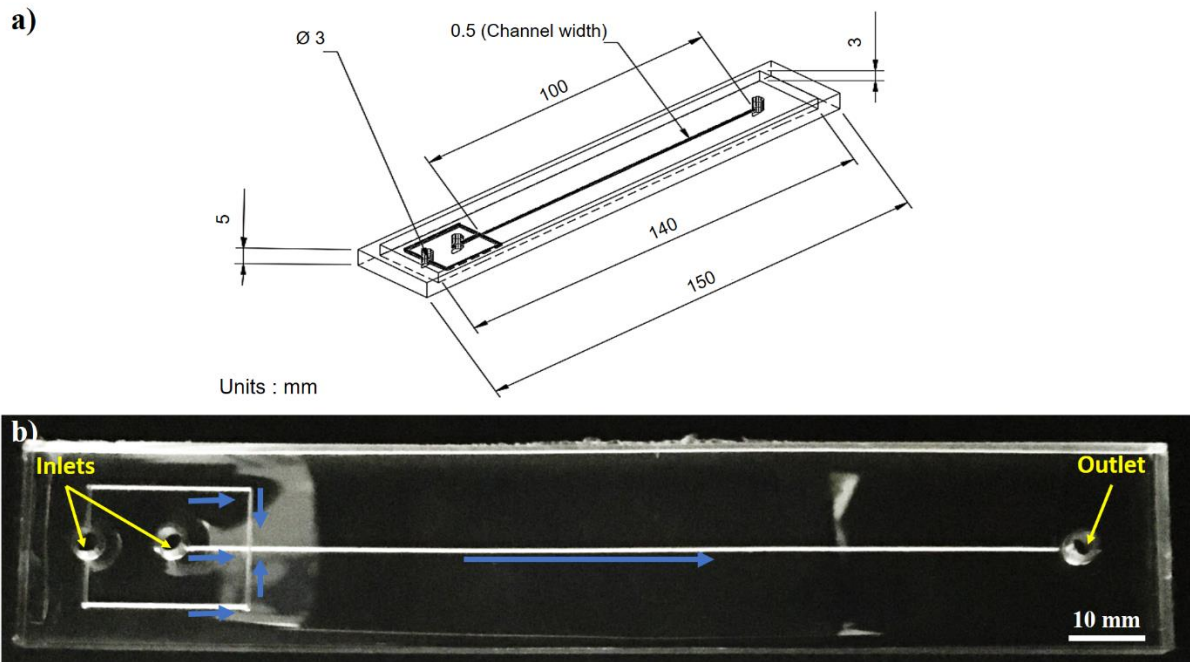


Figure 36: The design of MD4. a) CAD design of the 3D printed mould showing the dimensions. b) PDMS cast of MD4 created using the 3D printed mould. Blue arrows indicate the direction of flow in the finished device.

The full PDMS fabrication process is outlined in Figure 37. Sylgard 184 PDMS was mixed as instructed on the kit with the curing agent and degassed via vacuum.²⁰¹ The degassed mixture was then poured into the 3D printed moulds and left to cure in an oven at 60°C overnight. The cured PDMS devices were then bonded to a blank plate of cured PDMS. This was achieved by treating the devices and blank plates of PDMS in a plasma oven HPT-300 benchtop plasma treater, Henniker Plasma, Warrington, UK). 50% power for 90 seconds were the treatment settings utilised. The treated surfaces were then be sealed together with light pressure and left for 24 hours to ensure a good bond is achieved. Care was taken when bringing the device and the blank wafer together to do so in a ‘rolling’ fashion in order to minimise any trapped air between the two surfaces.

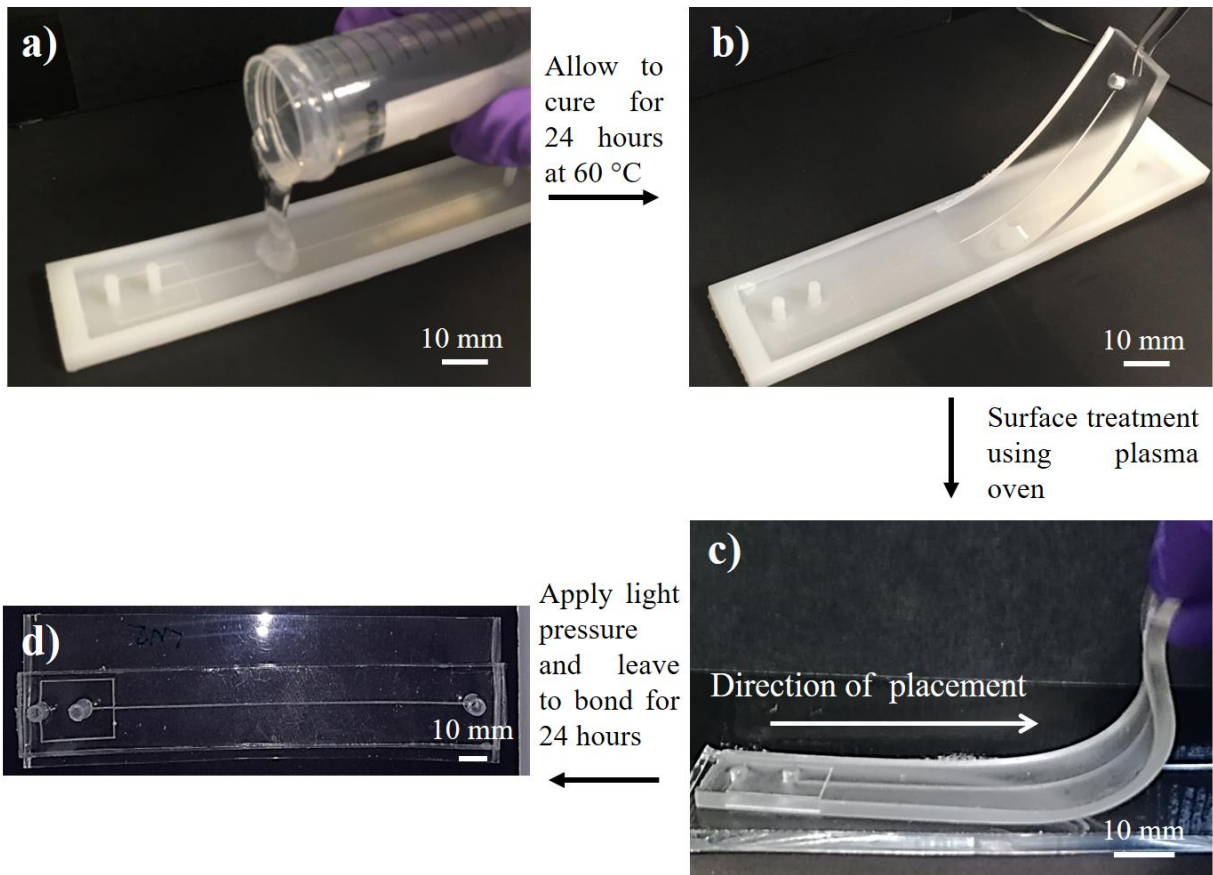


Figure 37: Fabrication process for the production of the PDMS devices MD3 and MD4. a) The mixed Sylgard 184 was poured into the 3D printed mould. And placed in an oven at 60°C for 24 hours. b) The cured PDMS was removed from the moulds and placed, with 'blank' PDMS wafers, in a plasma oven for surface treatment. c) The treated PDMS surface of the device was then brought together with a blank wafer. Care was taken to place the treated surfaces carefully in a 'rolling' fashion to minimise trapped air. d) After lightly pressing the two pieces together and being left for 24 hours, the final bonded device.

2.9 Size distribution analysis

Size distribution analysis was carried out by collecting optical microscope images. Between 10-100 microcapsules or droplets were measured to obtain a representative average and standard deviation.

Images were captured using a Nikon TE-2000 inverted microscope (Nikon Instruments Europe B.V., Surrey, UK) equipped with five objectives (2x, 4x, 10x, 20x, 40x). A high resolution black and white digital CCD camera (Retiga-EXL, QImaging, Media Cybernetics UK, Buckinghamshire, UK) was connected to the microscope and Image-Pro Plus software (Media Cybernetics, UK) was used to capture the images. Measurements were taken using the analysis software ImageJ. The size measurements for droplets are based on a scale from a micro ruler, imaged at the same magnification as the droplets to be analysed. A scale was then applied using a pixels per distance unit using the micro ruler. This scale could then be applied to all images at that magnification, with an accurate droplet diameter obtained through drawing a line across the diameter of each droplet and using the 'measure' function.

2.10 SEM analysis

Scanning electron microscope (SEM) images were captured by a Zeiss Supra 55 VP electron microscope. Samples were sputtered with gold prior to imaging.

2.11 IR analysis

Fourier transform infrared (FTIR-ATR) analysis was carried out on a ThermoScientific Nicolet iS5 fitted with a Pike Miracle diamond ATR attachment. Samples were directly loaded onto the diamond window of the ATR instrument for characterisation.

2.12 TGA analysis

Thermogravimetric analysis (TGA) was carried out using either, a Perkin Elmer TGA 4000 instrument or a Mettler Toledo TGA/SDTA851° equipped with a TS0801RO autosampler. Testing was carried out using a temperature range of 25 – 900 °C under a nitrogen atmosphere, with a heating rate of 10 °C·min⁻¹. The specific instrumentation, temperature range and heating rate is specified when discussed.

2.13 Generation of formulations for stereolithographic printing resins

For the SLA printing of extrinsically self-healing materials, the generated capsules were mixed into commercial UV resins by hand for 2 min and subsequently degassed under vacuum. These formulations were then cured into the desired shape either via use of silicone moulds (for the self-healing efficiency, method outlined in 2.13) or poured into resin tanks to be utilised in 3D printing, as outlined in section 2.14.

2.14 Tapered double cantilever beam (TDCB) measurements and quantification of self-healing

All tapered double cantilever beam (TDCB) measurements were taken using the EZ50 Universal Testing Machine (Lloyd Instruments, UK). Mechanical testing of the virgin and healed materials was achieved by pre-cracking samples within the notched section of the samples, loading into the instrument and performing mode 1 tensile fracture testing using a TDCB geometry (Figure 38).

The required geometry was first drawn as a 3D model (Figure 38) and then printed in PLA using an Ultimaker 2+ 3D printer (Ultimaker B.V., Utrecht, Netherlands) to generate a master (Figure 38b), from which the two-part silicone moulds were cast. The silicone moulds were prepared using the Sylgard 184 kit that was mixed according to the manufacturer's instructions and degassed via centrifugation at 10,000 rpm for 5 min. The formulations were cured in the moulds to achieve the desired geometry through utilisation of a 365 nm wavelength UV light source at a fixed distance of 15 cm from the curing stage for 10 min. the samples were flipped after 5 minutes to prevent the capsules from settling to the bottom of the mould before the samples could fully cure.

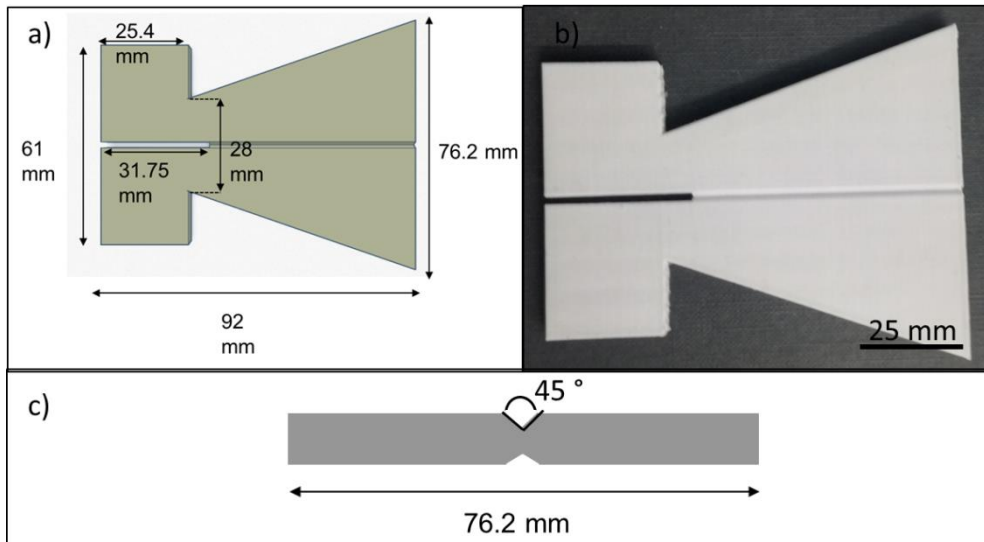


Figure 38: (a) Graphical representation of the TDCB sample dimensions as seen from above. (b) Photograph of 3D printed master from which the silicone moulds were cast. (c) Graphical representation of the TDCB sample as seen from the side. The 45 ° angle groove promotes linear crack propagation within the sample.

Samples have a 45° angle groove along the centre line of the sample (Figure 38c). A sharp pre-crack was introduced at the start of the groove using a new scalpel blade to each sample just before testing. The displacement rate was fixed at 0.5 mm min⁻¹ for all tests and the clamped samples were pulled until the propagated crack length ranged from 15-20 mm (Figure 39). After the initial fracture event, the self-healing samples were unloaded, and the cracked surfaces allowed to come back together. The samples were then left to heal at 25 °C for various healing times before being reloaded and undergoing fracture again. An example of the load displacement curves that were produced is shown in Figure 40. From this the % healing efficiency was calculated from the ratio of the critical loads of the virgin and healed samples. All tests were performed in triplicate, with sets of three samples.

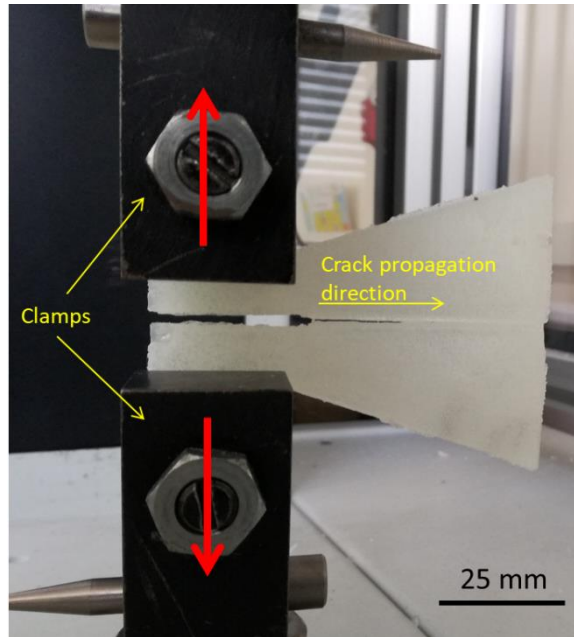


Figure 39: Photograph showing a TDCB sample loaded into the universal testing instrument. The red arrows indicate the direction of the pulling force.

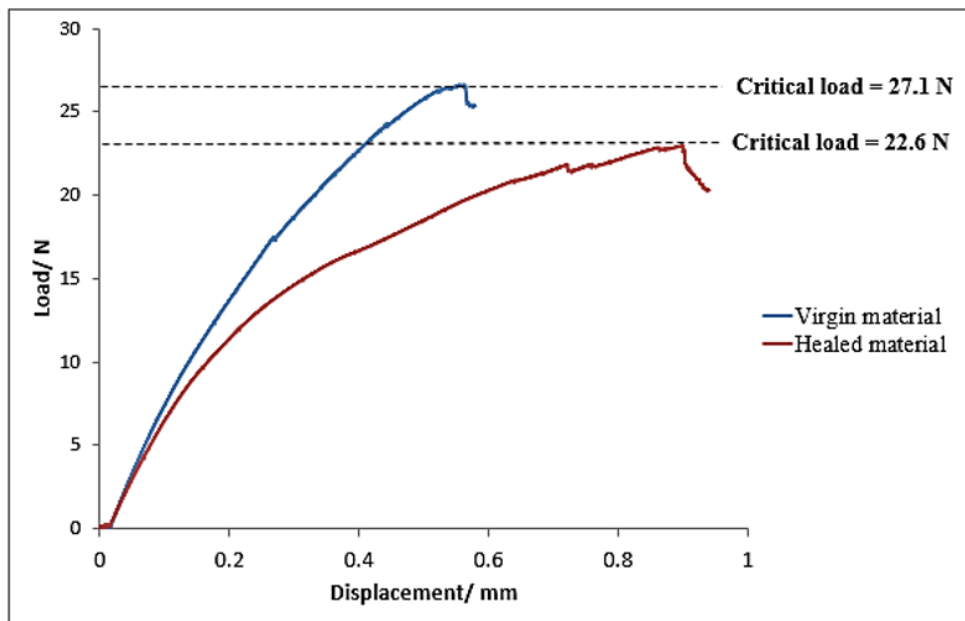


Figure 40: An example of the load displacement graphs produced during the mechanical testing. It can be seen that fracture is more unstable and at a lower critical load, P_c , for the healed samples.

2.15 3D printing

3D printing of the composite materials was carried out using a Form 1+ 3D printer, (Formlabs, Berlin, Germany). The Form 1+ is a SLA printer utilises a laser ($\lambda = 405 \text{ nm}$) to spatioselectively polymerise and crosslink resin according to a computer aided design (CAD). All G-codes were generated using the Preform software (Formlabs, Berlin, Germany) before being uploaded to the printer. The printer utilised in this work is shown in Figure 41a. The composites were printed by use of resin tanks that were filled with commercial SLA resins that had been modified as outlined in section 2.9, to provide the desired functionality. All printing tests for the resin formulations utilised the same pyramid design shown in Figure 41b.

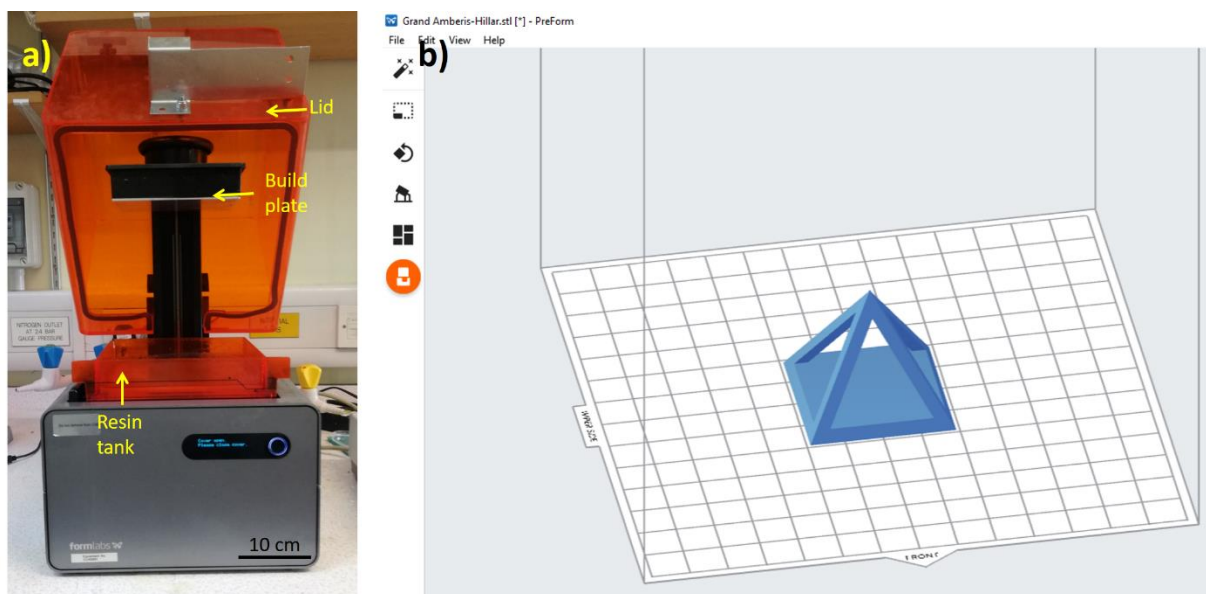


Figure 41: a) Formlabs 1+ printer. The build plate on which the polymerised resin adheres to during printing is shown and the resin tank which is filled with the modified resins. During printing the lid is closed which stops the user from being exposed to harmful UV light. b) The pyramid STL file used for the printing tests loaded into the slicing software Preform.

3. STEREOLITHOGRAPHIC 3D PRINTING OF EXTRINSICALLY SELF-HEALING MATERIALS

A technique of combining UV-curable resin embedded with solvent-containing microcapsules in conjunction with SLA 3D printing was used to construct user-defined 3D structures with self-healing capability. The self-healing employed in this work follows a solvent welding mechanism, as illustrated in Figure 5. When a crack occurs and ruptures a capsule along the propagation pathway, the solvent within the capsule is released into the matrix. Solvent release promotes polymer diffusion and entanglement across cracks formed in the matrix, leading to crack healing.^{86,93} Such a method is advantageous in its simplicity and cost-effectiveness, with no need for expensive metal catalysts²⁰² or the preparation of multiple types of microcapsules containing different healing reagents.²⁰³

Anisole and ethyl phenylacetate (EPA), which are widely used in both the fragrance industry and as a food additive, were selected due to their low toxicity.^{93,123,204} The high boiling point and immiscibility of these solvents with water also allows for them to be easily encapsulated using the in situ polymerization of urea-formaldehyde in an oil-in-water emulsion.⁹¹ Furthermore, these solvents have been shown to be good candidates for solvent welding based self-healing in materials such as PMMA.^{87,123} As many commercially available SLA 3D printing resins are acrylate based, and thus contain functionalities similar to those of PMMA, anisole and EPA were therefore selected as the solvent for these investigations.

3.1 Capsule synthesis, characterisation and size distribution analysis

Capsules were synthesised using a technique modified from that described by Brown⁹¹ as outlined in section 2.2. EPA, anisole or anisole with dissolved 5 wt% PMMA was used as the core material; a schematic outlining the method of capsule production is shown in Figure 42a.

The synthesised capsules were analysed utilising SEM, TGA and FTIR-ATR and their size was determined via image analysis from optical microscopy.

For all three types of capsules, SEM images showed spherical microcapsules with a rough surface morphology (Figure 42b). This observation is also described within the literature^{92,122,205} ; the surface roughness being attributed to the precipitation of urea-formaldehyde nanoparticles onto the surface of the droplets. The capsules were crushed and washed with acetone to remove any of the solvent contents and again studied via SEM imaging (Figure 42c). The crushed capsules showed the hollow void previously occupied by the encapsulated solvent and the shell wall thickness could be estimated to be 7 μm .

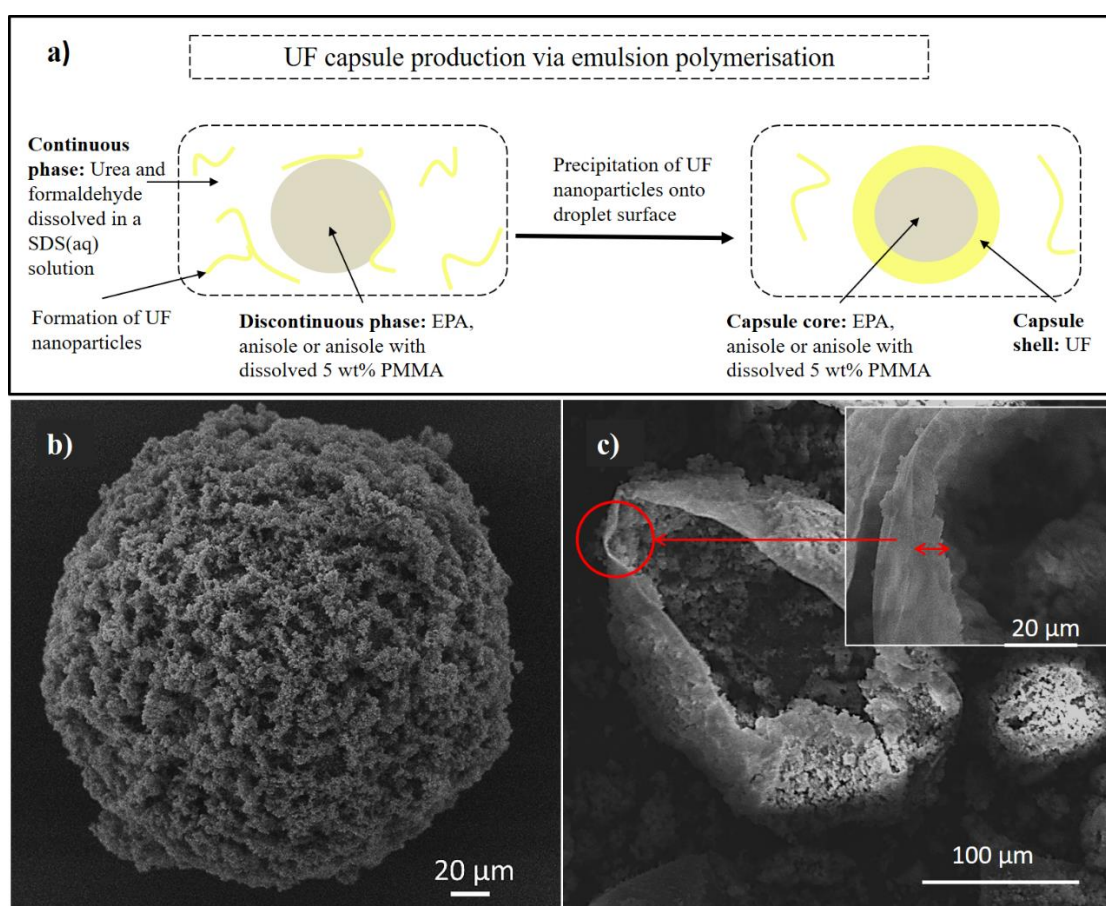


Figure 42: a) Schematic of UF capsule production via emulsion polymerisation, followed by precipitation of UF nanoparticles onto the surface of emulsion droplets. b) SEM images of capsules generated using this method, showing a spherical structure possessing rough surface morphology. c) After crushing the capsules to release the encapsulated solvent, SEM imaging shows the empty cavity left by the released solvent and the shell wall can be observed.

TGA analysis was carried out on the three types of capsule (Figure 43). As seen in the figure, all three capsules showed large weight loss between 250-280 °C. This can be attributed to the deterioration of the urea-formaldehyde shell material. The loss of the shell sometimes manifested in an unusual spike, as seen in Figure 43a. This observation can be attributed to the expansion of the solvent within the capsules and the subsequent explosion of the capsules as has been described within the literature previously.^{92,205} Reducing the heating ramp rate and the sample size lead to a reduction in this phenomenon. The data collected for the anisole with PMMA capsules was therefore ran at different conditions to the other capsules (Figure 43c).

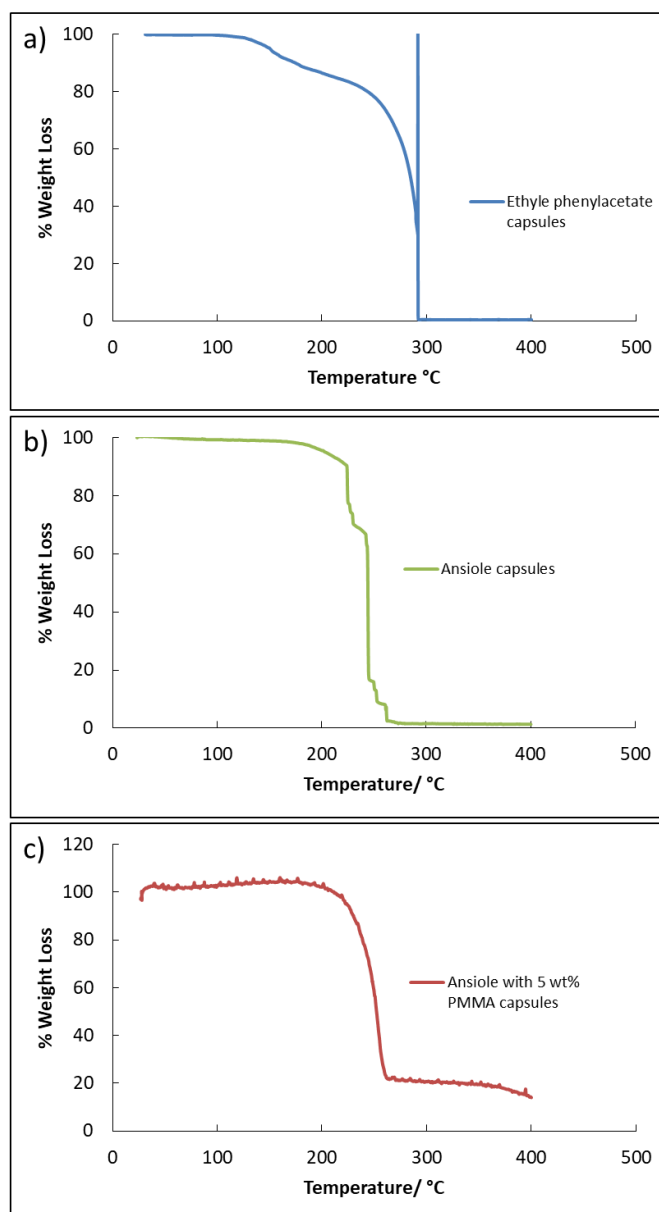


Figure 43: TGA curves for various capsules. (a) Capsules containing EPA which shows a large spike at 280 °C, which has been attributed to the expansion of solvent within the capsules. (b) Capsules containing anisole. (c) Capsules containing anisole with 5 wt% PMMA. All capsules show a large weight loss step at 250-280 °C which indicates the loss of the shell wall material. Note, the anisole with 5 wt% PMMA was ran with a very small sample size, ~0.9 mg and a reduced heating rate, in an effort to reduce the effects of solvent expansion which had a severe impact on the quality of the data obtained for this capsule type. The deterioration of the shell wall can now be seen clearly however the small sample size has led to an increase in noise present in the data.

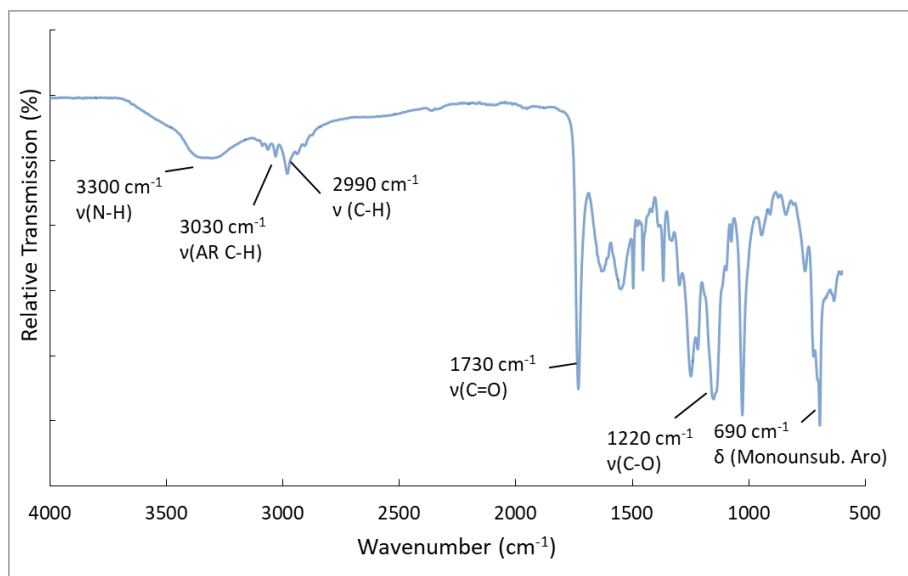


Figure 44: FTIR-ATR spectrum of the urea-formaldehyde capsules. The N-H stretching frequency can be seen at 3300 cm^{-1} which is expected to be present from the urea-formaldehyde shell.

FTIR-ATR analysis was carried out and the urea-formaldehyde shell was confirmed through the presence of N-H stretching mode at 3300 cm^{-1} shown in Figure 44.

Throughout the literature, for emulsions, droplet size (and therefore the resulting capsule size) is heavily dependent on mixing speed.^{206,207} Generally, increasing shear rate (mixing speed) of the agitation leads to a greater chance of droplet breakup,²⁰⁸ which in turn produces smaller droplet diameter size. EPA and anisole containing capsules were both investigated at different mixing speeds. Images were taken via optical microscopy (see section 2.8), capsule size was determined using ImageJ software. 100 capsules were measured to derive an average and standard deviation (Figure 45).

Capsules were synthesised within the size range of 61-263 μm . The size range of microcapsules utilised for extrinsically self-healing materials in the literature ranges from a few micrometers⁷⁴

to a few hundred micrometers⁷⁵. The synthesised microcapsules were therefore within a promising size range. As discussed in section 1.2.2, larger capsules produce higher healing efficiencies but for use within the 3D printer with a layer height of 200 μm , the microcapsules utilised should not exceed this size. Therefore, a mixing speed of 400 rpm was utilised producing capsules with an average diameter of 191 μm and 130 μm for the EPA and anisole containing capsules respectively.

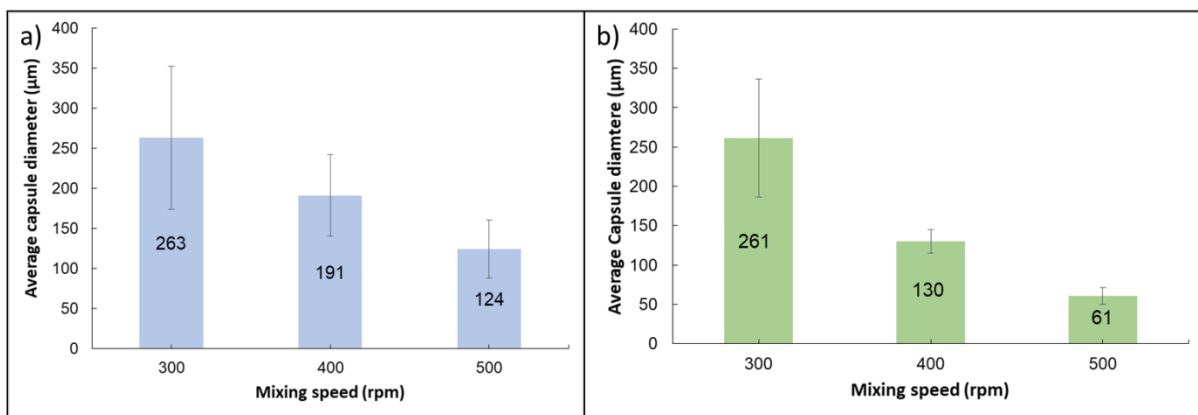


Figure 45: Size distribution dependence on mixing speed for capsules containing (a) EPA and (b) anisole. Generally, as mixing speed is increased, the capsules generated decreased in size. ($n=100$)

3.2 Formulation of self-healing composites

A range of formulations were generated using the method outlined in section 2.13. Composites were made with varying, capsule core material, matrix material and with different wt% loading of capsules as shown in Table 9.

The decomposition of the formulations was studied via TGA. The cured Photocentric 3D Firm resin was found to decompose at 390 $^{\circ}\text{C}$ as shown in the yellow trace in Figure 46. The cured resin samples containing capsule loadings of 5, 10 and 15wt% are plotted in Figure 46 as green, blue and red traces, respectively. These showed weight losses of 5, 10 and 15% when the temperature had reached 290 $^{\circ}\text{C}$, which indicated the point of capsule decomposition. The bulk

weight loss occurs at 390 °C, which corresponds to the decomposition temperature of the resin matrix material.

Table 9: The different formulations studied. Core material, matrix material and loading (by wt%) were all investigated. Blue indicates samples which were loaded with EPA containing capsules. Green indicates those loaded with anisole containing capsules and orange indicates those loaded with anisole with 5 wt% PMMA.

	Matrix material	
Core material	Firm Resin	Hard resin
	0 wt%	0 wt%
EPA	5 wt%	
	10 wt%	
	15 wt%	
Anisole	5 wt%	
Anisole with 5 wt% PMMA	5 wt%	
		2.5 wt%
		5 wt%
		10 wt%

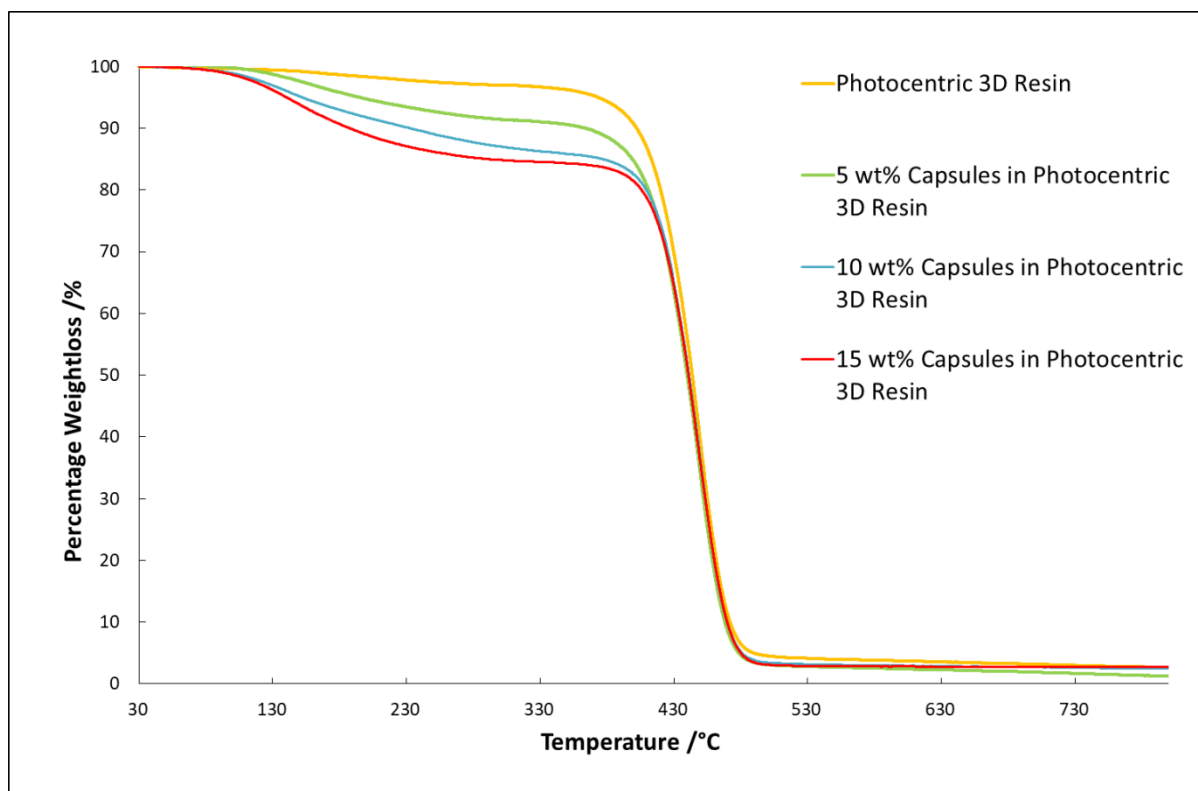


Figure 46: TGA curves for composites with increasing wt% capsule loadings. The pure resin sample (yellow) showed only a single sharp loss in weight at 390 °C indicating the temperature at which the resin decomposes. The samples containing 5, 10 and 15 wt% urea-formaldehyde capsules showed a significant weight loss step at 290 °C (at which point full decomposition of capsules should have occurred) which correspond to losses of 5, 10 and 15 wt% respectively.

3.3 Quantification of self-healing efficiency

The formulations prepared as per Table 9 underwent mechanical testing using the method outlined in section 2.14. Materials with capsules containing EPA were first investigated. Pc values were obtained for both virgin samples and healed samples (Figure 47). There was a noticeable increase in Pc, and therefore Kc with increasing capsule loading, suggesting a toughening effect upon capsule addition.¹¹⁶ This effect seemed to diminish beyond 15 wt% loading of capsules where Pc dropped back to previous levels, which matches the effect seen in the literature.¹¹⁶

The healing efficiencies were calculated using Equation 6 for different capsule loading (Figure 48a) and healing times (Figure 48b). As can be seen in the figure, an increase in healing efficiency was found with an increase in both these parameters until a maximum healing efficiency was reached. This is in line with trends reported for healing of polymers via solvent welding.^{98,209–211}

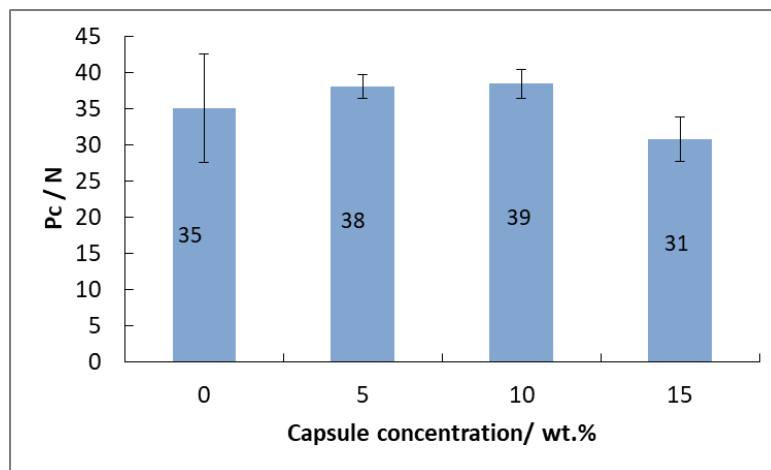


Figure 47: Critical loads of Photocentric firm resin loaded in EPA filled capsules at different loadings. There is an initial increase in critical load upon addition of capsules which suggests that a toughening effect is taking place. This effect is not further increased by addition of further capsules and the critical load falls again at 15 wt% loading.

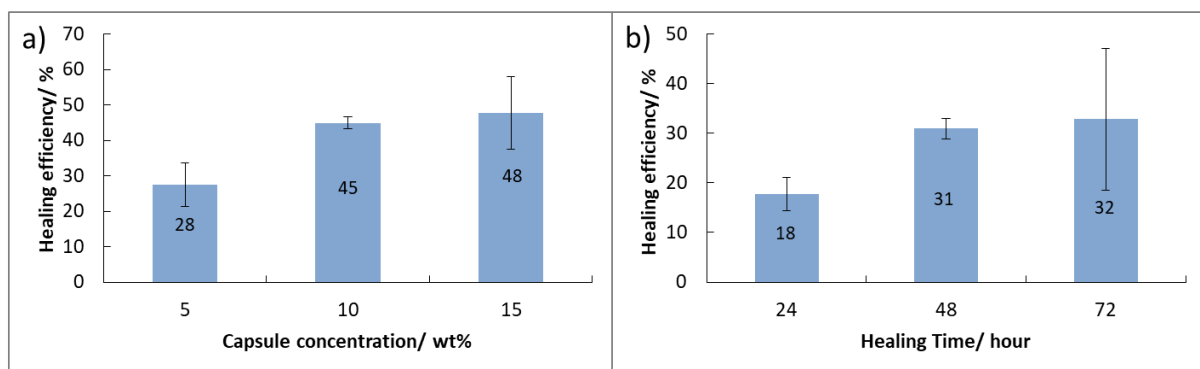


Figure 48: The healing efficiencies of materials loaded with capsules with EPA cores. (a) The effect of increasing capsule concentration on healing efficiency. (b) The effect of increasing

healing time on healing efficiency. At 15 wt% loading and with a healing time of 48 hours, the best self-healing efficiency of 48% was achieved.

In a following series of experiments, different core materials were tested. The matrix material, Photocentric 3D Firm resin was maintained. The self-healing efficiencies of samples containing EPA, anisole and anisole with 5wt% PMMA capsules are shown in Figure 49. Efficiencies were far higher when using anisole compared to EPA. The introduction of PMMA polymer chains dissolved in anisole lead to a further improvement of the self-healing efficiency. The inclusion of dissolved polymer within the solvent used in these types of composites has previously been shown to improve solvent welding mechanisms.⁸⁷ It is thought the additional polymer dissolved in the solvent enhances the self-healing effect as the polymer chains can diffuse readily in the solvent; enhancing the chain entanglement process and therefore the self-healing mechanism.

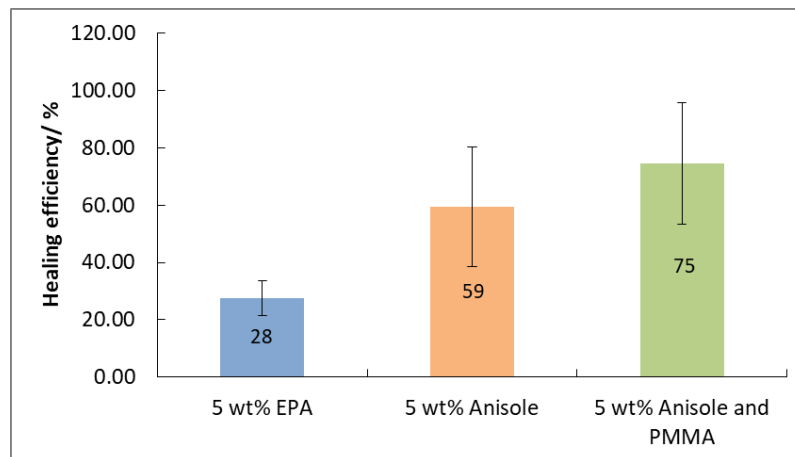


Figure 49: Healing efficiencies of materials which contain the same concentration of capsules but with different core materials. It was shown that anisole produces better rates of self-healing; the addition of polymer chains such as PMMA enhances this effect further.

Further optimisation required investigation into the matrix material. Previous experiments were carried out with Photocentric 3D Firm resin. A harder matrix material, Photocentric 3D hard resin, was studied in comparison. The properties of the hard resin can be seen from the load displacement curves (Figure 50). For the hard resin a higher load was required to fracture the sample compared to the firm resin, however the extension that can occur before fracture was much lower than that of the firm resin. This indicated a hard but brittle material.

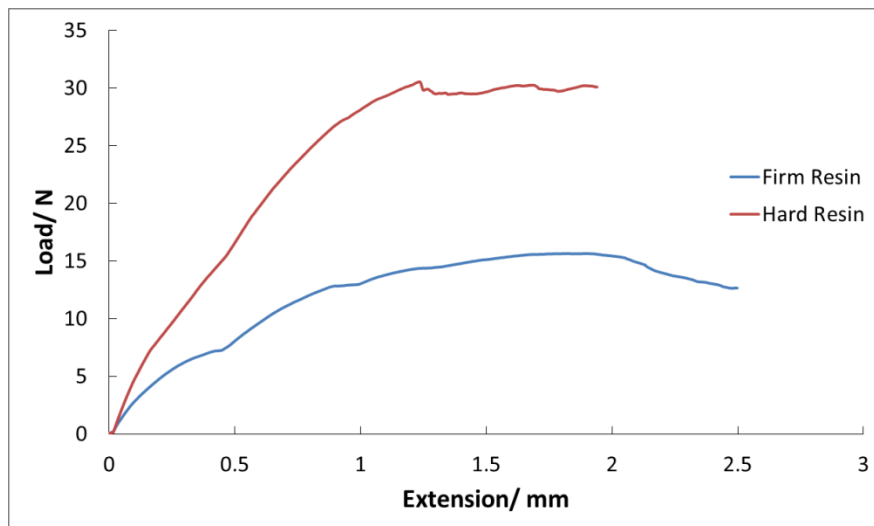


Figure 50: Load displacement curves for the Photocentric firm and Photocentric hard resins. It can be seen that the hard resin (red) requires a much higher load in order for failure to occur, however the material is more brittle as failure occurs at a lower extension. The brittleness of the material compared to the firm resin suggests that the toughening effect that is seen upon introduction of capsules could be more enhanced if this material was used as the matrix as opposed to the firm resin.

It was theorised, that at the same capsule loading, the toughening and healing effects upon capsule addition would be enhanced when the harder, but more brittle, resin was utilised. Composites with capsules containing anisole and PMMA were investigated at a range of healing times and capsule loadings. As with EPA, there was an initial increase in P_c with increasing capsule loading (Figure 51) although this effect seemed to be limited to smaller capsule loadings (2.5 wt%), compared to what was seen with the previous material (10 wt%, Figure 47). This is contrary to what was theorised, although the toughening effect is dependent upon core content as well as size and loading wt% of capsules. The inherently higher P_c associated with the hard resin however did mean that the healing effect was more pronounced than with the firm resin. This was seen when both matrix resins were loaded with the same capsules (5 wt% anisole and PMMA): the healing efficiencies rose from 75% in the firm resin (Figure 49) compared to 82% for the hard resin (Figure 52).

The efficiency of the anisole capsules within this self-healing system were then investigated at various loading and healing times. The hard Photocentric resin was used as the matrix material. Enhanced healing efficiency with increasing healing time and capsule loading were seen with the anisole capsule loaded composites (Figure 52). This result was as expected, the same trend was seen with the EPA capsule loaded composites and is well documented in the literature for similar solvent welding based self-healing composites.²¹² Overall, anisole with PMMA as the core material, in the hard Photocentric resin, at 10 wt% loading and with a healing time of 72 h produced the best self-healing efficiency of 87%.

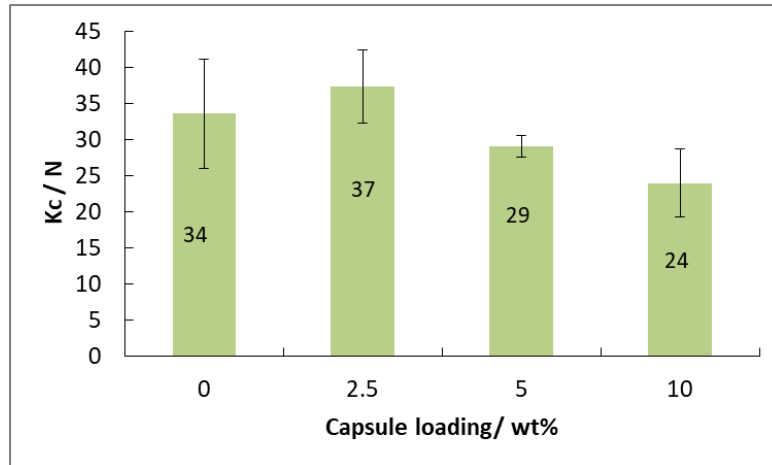


Figure 51: The effect of capsules loading on the critical loads of hard resin. There is an initial increase in critical load upon addition of capsules which suggests that a toughening effect is taking place. This effect is not as effective as seen with the firm resin and diminishes after exceeding 2.5 wt% capsule loading.

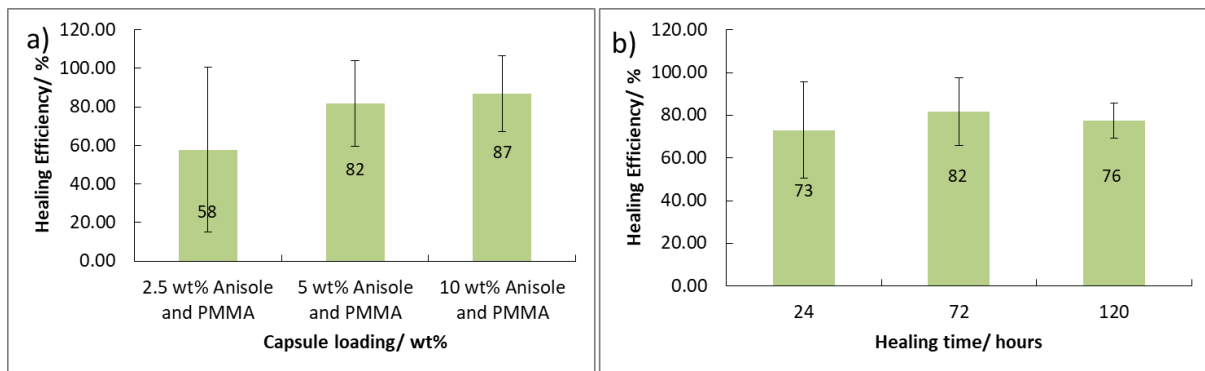


Figure 52: The healing efficiencies of composites made with hard resin matrices and loaded with capsules with anisole and PMMA cores. (a) The effect of increasing capsule concentration on healing efficiency. (b) The effect of increasing healing time on healing efficiency. At 10 wt% loading and with a healing time of 72 h, the best self-healing efficiency of 87% was achieved.

The fracture planes of these materials were also investigated using SEM to study the fracture patterns and show the embedding of the capsules within the resin. Embedded capsules within the matrix material can be seen in Figure 53a and a broken capsule as a result of fracture is shown in Figure 53c. This confirms that upon fracture of the material, rupture of the capsules and release of the self-healing agent occurs.

As shown in Figures 47 and 51 the material experiences an initial increase in critical load and therefore, (as discussed in section 1.2.4), fracture toughness upon addition of the microcapsules. This indicates a toughening effect is taking place upon addition of capsules to the matrix. The fracture patterns observed on the surface of the plane can also be indicative of the type of fracture that occurs and analysis of this could provide an explanation for the increase in fracture toughness observed. Fracture planes of material that contain no capsules are smooth (Figure 53b) which is indicative of brittle fracture. The presence of tail like structures in the wake of the microcapsules in the fracture plane (Figure 53a) suggests that crack pinning could contribute to the observed fracture toughening.⁸⁰ Hackle markings, which tend to form during violent fracture when both plastic deformation and branching of the crack front occur,²¹³ can also be observed. Both the tail and hackle markings increase the surface area of the crack plane, and thus the energy absorbed by the composite during crack growth, thereby increasing the resulting fracture toughness. This fracture toughening mechanism as a result of incorporation of urea-formaldehyde capsules is supported in the literature for a number of capsule based containing composites.^{80,87,116}

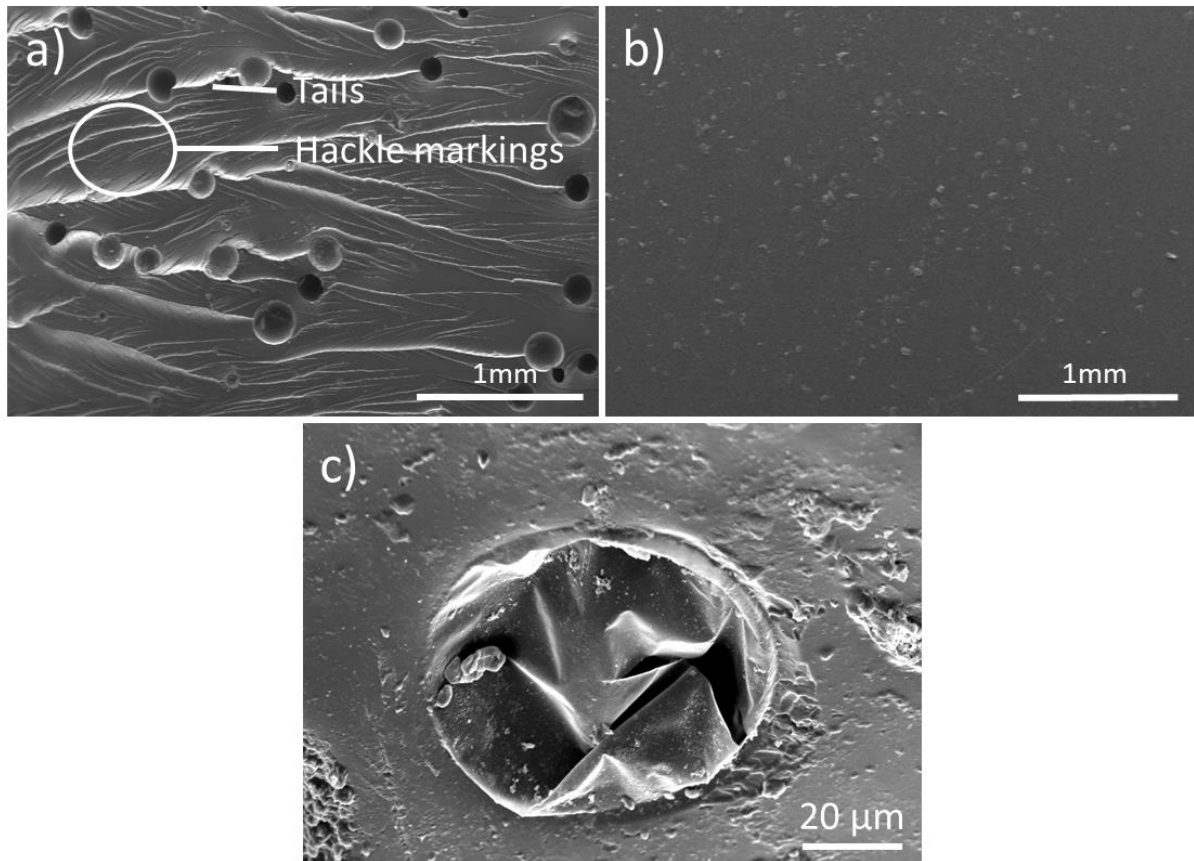


Figure 53: SEM images of fracture planes. a) Fracture plane of cured resin which contains capsules. The fracture plane is rough showing hackle markings and tail structures can be seen following the capsules which suggests some fracture toughening mechanism is occurring. b) Fracture plane of cured resin which contains no capsules. The fracture plane is smooth which suggests brittle fracture. c) Detailed image showing an embedded capsule within the resin that ruptured upon fracture.

3.4 3D printing

Incorporation of the modified resins into a 3D printer allowed for 3D printed samples to be produced. A pyramid shape (details provided in section 2.14) was printed from resins with various loadings and capsule content using the method outlined in section 2.15.

It can be seen that 3D printed samples could be generated at the loadings required to achieve good self-healing for both EPA (Figure 54) and anisole (Figure 55) containing capsules. There was a concern that the light scattering effect of the capsules would cause poor quality prints to be produced but this was not the case even at higher loadings such as 15 wt%. This observation is further supported with the knowledge that commercial resins on the market currently already have pigments and other particulates in them and show no ill effects to print quality.

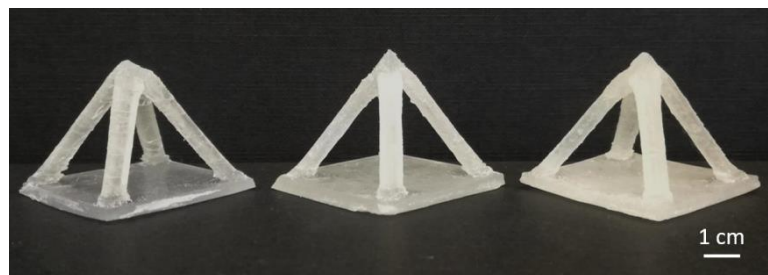


Figure 54: 3D printed samples containing capsules with EPA cores, printed at 5, 10 and 15 wt% loading.



Figure 55: 3D printed samples containing capsules with anisole cores, printed at 0, 5 and 10 wt% loading.

The 3D printed samples were then subjected to damage via manually fracturing one of the legs of the pyramid (Figure 56a). The two fracture planes were then allowed to come back together and left to heal for 72 h at 25 °C, *i.e.* the conditions previously used for the fracture experiments. After this time the fracture had healed (Figure 56b) with only some ‘scarring’ remaining at the location of the fracture.

The ability to heal a fracture like this suggests that the processing condition the capsules undergo during printing does not compromise the capsules’ structural integrity, solvent core content and the resulting composite structures self-healing capability.

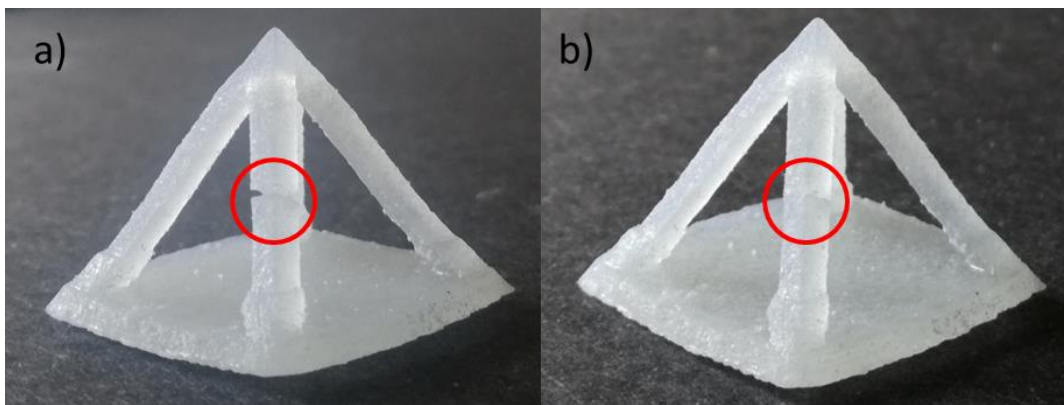


Figure 56: 3D printed sample with a) showing fracture to the leg of the pyramid (damaged area highlighted with a red circle) and b) showing the fracture after the planar faces were brought back together and left for 72 hours. This suggests that the processing conditions the capsules undergo during the 3D printing process does not affect their ability to function as part of the self-healing mechanism.

3.5 Conclusion to stereolithographic 3D printing of extrinsically self-healing materials

A material which was shown to possess some self-healing ability was successfully utilised in a 3D printer to produce structures. Through the use of mode I fracture testing on samples which possess the TDCB geometry, the capability of fracture toughness recovery after healing via a classic solvent welding mechanism was shown to be 48-59% depending on which solvent and concentration was used. The addition of PMMA into the core of the capsules and increasing the healing time to 72 h enhanced the self-healing ability of the solvent anisole. Under these conditions, mechanical testing showed a capability for fracture toughness recovery of 87%.

The utilisation of these formulations within an SLA 3D printer allowed for the printing of self-healing composites. The addition of capsules to the resins did not impact the capability to produce structures via 3D printing. The ability of a 3D printed structure to recover from damage was shown through manual fracture of the 3D printed composite and showed autonomous recovery after 72 h.

4. INVESTIGATION INTO THE PRODUCTION OF MICROCAPSULES FOR USE IN TRANSPARENT SELF-HEALING MATERIALS VIA TRADITIONAL MIXING METHODS

A technique for the production of microcapsules with refractive index (RI) matched core and shell materials was investigated. These microcapsules could then be combined with 3D printing resins in order to produce transparent 3D structures with self-healing capability. Through RI matching of all components; matrix, shell wall and encapsulated material, a transparent extrinsically self-healing material could be produced with 3D printing capability. Previous attempts to create transparent extrinsically self-healing materials were based on a PMMA matrix utilising a solvent-welding technique which used urea-formaldehyde as the shell wall material.⁷⁷ This work addressed the need to RI match the matrix and the self-healing component. However, urea-formaldehyde was still utilised as the shell wall material which is not a transparent material. The capsule size was therefore limited to being very small (maximum of 75 μm) in order to reduce light scattering effects of the urea-formaldehyde shell material. In this example, the smaller capsule size utilised, means that these materials were suitable only for coatings/thin films in which only barrier healing is necessary and the ability of this material to recover mechanical damage was not shown.⁷⁷ In general, smaller capsules limit the size of the crack that can be healed.²¹⁴ In order to produce a transparent self-healing material with the ability to heal larger damage, larger capsules with a transparent shell wall material, which is ideally RI matched with the matrix is required.

The self-healing approach employed in this work is an adaption of the solvent welding mechanism similar to that used in chapter 3. However, rather than employing a solvent as the encapsulated self-healing agent, liquid oligomers were utilised. The wide range of liquid oligomers available would allow for easier RI matching with the matrix material. The higher

molecular weight of oligomers compared to most solvents increases molecular friction and viscosity of the oligomer, which should reduce premature diffusion of the polymer shell wall material (which would be susceptible to rapid attack from most organic solvents). A polymer shell wall material is required in order to achieve RI matching with the polymer matrix material. (Figure 57)

A new capsule synthesis method utilising either PMMA or a commercial 3D printing resin as the shell wall material is outlined in sections 2.3 and 2.4. PMMA was chosen as many commercially available SL 3DP resins are acrylate-based, and thus contain properties similar to those of PMMA including RI. PMMA has also been used as an alternative to urea-formaldehyde as the shell wall material for the encapsulation of various self-healing agents in the literature.^{125,215} The commercial resin was chosen for investigation as the shell would then be the same material as the matrix and should therefore result in perfect RI matching.

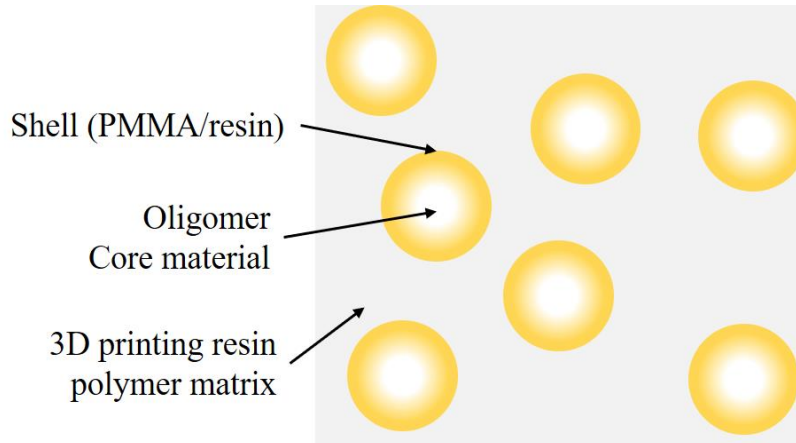


Figure 57: The 3 components for consideration when designing a transparent, extrinsic self-healing mechanism. By developing an encapsulation method which replaces the traditional UF shell with a transparent material, coupled with matching the RI of the shell, core material and the matrix; a transparent self-healing material could be achieved.

4.1 PMMA capsules

Capsules with PMMA shells were synthesised using a solvent evaporation technique outlined in section 2.3. The capsules produced were very small and collection was difficult. A number of methods including filtration and centrifugation were tried. The capsules collected by filtration produced a low yield and filtration was slow and cumbersome. Centrifugation produced higher yields however centrifugation speeds needed to be adjusted in order to reduce breakage of capsules (Figure 58).

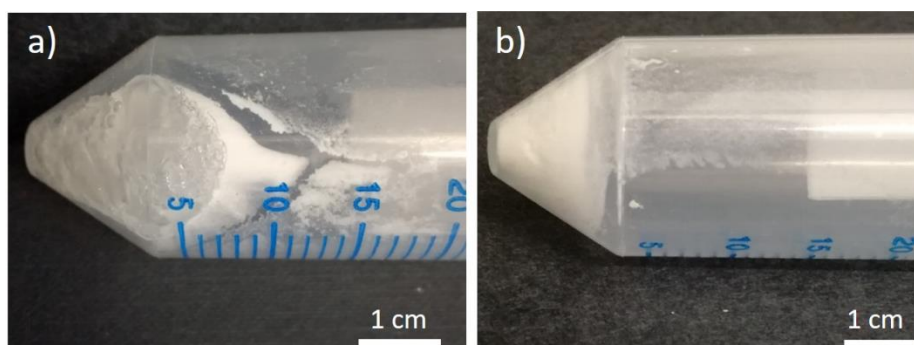


Figure 58: Collection of capsules via centrifugation. (a) An example of capsules rupturing and releasing the epoxy caused by centrifugation at higher speed (2000 rpm). (b) At lower centrifugation speeds (500 rpm), capsules could be collected successfully without rupture and release of contents.

The capsules however were found to not be transparent. The literature suggested that a number of factors including core/ shell ratio,²¹⁶ evaporation temperature^{217,218} and the solvent utilised in solvent evaporation¹³⁵ can have a significant impact on the surface morphology of capsules produced using this method. These parameters determine the speed at which the solvent (and the dissolved PMMA) migrates to the droplet surface and the subsequent solvent evaporation. Incomplete phase separation and rapid evaporation of the solvent can lead to uneven shell thickness and ‘pitting’ on the surface. The surface morphology of the capsules is important, as

a smoother surface reduces the amount of resultant light scattering and therefore the capsules will be transparent.¹³⁵

Coupled with the inconsistency in producing transparent capsules, the final issue when using this technique was the small size and agglomeration of the capsules. (Figure59)

Capsule size was measured to be $9 \pm 5 \mu\text{m}$. The size range of microcapsules utilised for extrinsically self-healing materials in the literature can range from a few micrometers⁷⁴ to a few hundred micrometers⁷⁵. As highlighted in the introduction section of this chapter however, small capsules (below $75 \mu\text{m}$) struggle to heal crack damage and are mostly limited to the coating applications.^{76,77} Ideally, the capsules for this application should be $100\text{-}200 \mu\text{m}$. Within this range they would be useful for crack healing but below the layer height of $200 \mu\text{m}$ required for the 3D printing process.

Figure 59 also shows the agglomeration of the capsules using this synthesis method, this would lead to poor distribution of the capsules within the matrix for the final material. This could also explain why initial filtration was difficult.

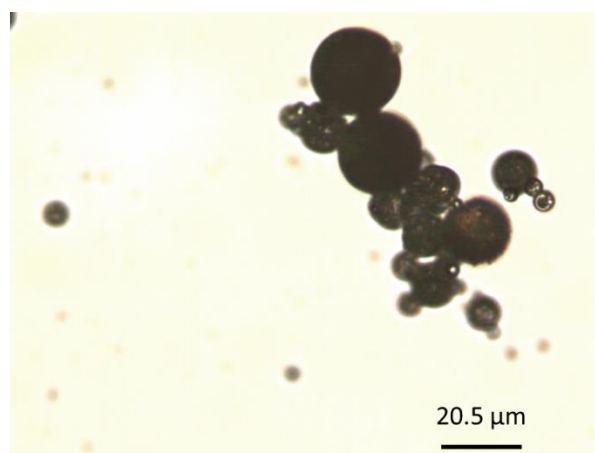


Figure 59: Optical image of capsules generated using the solvent evaporation technique. Microcapsule size was measured to be $9 \pm 5 \mu\text{m}$. The capsules were not transparent and were agglomerated.

4.2 Commercial resin capsules

Due to the complex parameters and unreliable production of transparent capsules using the solvent evaporation technique, capsules were synthesised using the method outlined in section 2.4. This involves the utilisation of the same resin for both the polymer matrix and the shell wall of the embedded capsules. This should satisfy the requirements for transparency highlighted in Figure 57 as the two components will have perfectly matched RI values. This synthesis method relies on a self-assembly mechanism outlined in Figure 60.

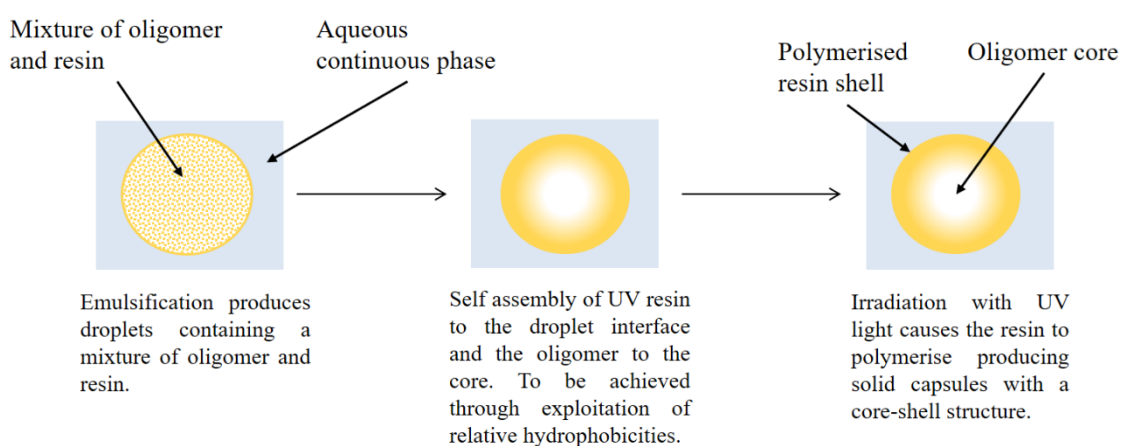


Figure 60: Schematic method for capsules with core-shell structure via a self-assembly mechanism. Through utilisation of UV polymerizable resin which preferentially assembles at the droplet interface, solid capsules with a more hydrophobic polymer core can be attained through irradiation with UV light.

The main issue left for consideration of this synthesis method resides in the selection of the self-healing core material; the material needs to be more hydrophobic than the unpolymerized resin to allow for the assembly of a core shell structure upon emulsification. Also, the RI value for the core material also needs to closely match that of the polymerised resin so that all three components now satisfy the requirements for transparency highlighted in Figure 57.

Various steps were taken during the optimisation process in an effort to solve various issues with the synthesis method including, problems with emulsion stability, agglomeration, capsule size and transparency of the capsules, which are summarised in Figure 61.

The best surfactant with regards to emulsion stability and lowest aggregation rate was found to be SDS. Increased surfactant concentration and an increase in phase volume ratios were also considered for these issues as increasing these parameters can increase emulsion stability.

The core material chosen was EPON 828; key factors for consideration in this aspect were a higher relative hydrophobicity of the core material compared to the intended shell material (unpolymerized resin) and the RI matching of the core material with the shell material (polymerised resin).

The mixing method for emulsification was the final consideration, the emulsification method thus far had utilised a propeller mixer. The capsule size was just too large, with the produced capsules ranging from 500-1000 μm . Investigation into the use of higher shear mixing such as the use of a homogeniser was done but the inability to continue mixing using this method during the polymerisation of the shell wall (as the high shear could break the solid shell that would be produced) and therefore the emulsion falls to the bottom of the mixing vessel and therefore capsules could not be produced. High shear homogenisation during emulsification with subsequent low shear during the polymerisation step was also tested but the small droplets aggregated into larger droplets during the polymerisation resulting in capsules polydisperse in size (100-500 μm). The capsule size range required for this application is between 100-200 μm .

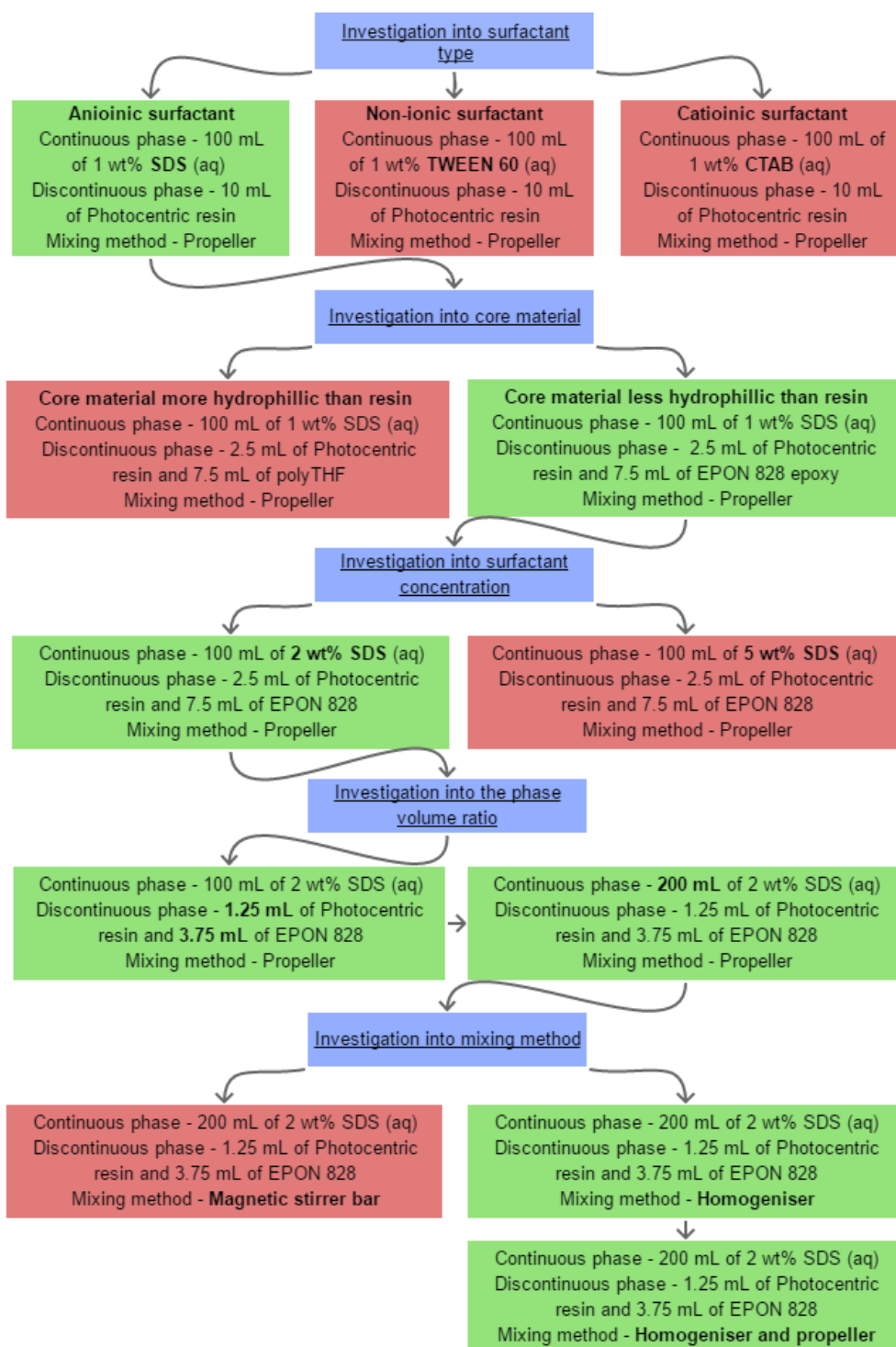
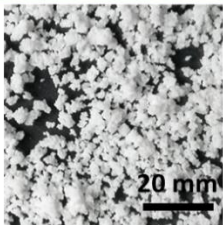
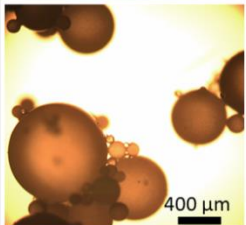
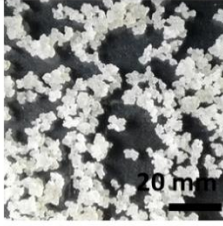
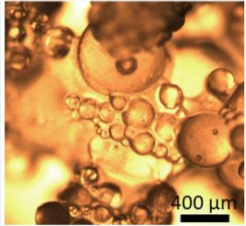
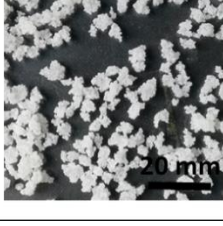
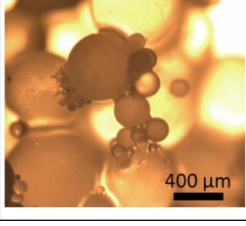


Figure 61: Flow scheme showing the optimisation process for capsule production. Green boxes indicate a positive result, red indicates negative. The changes made to the synthesis at each step are in **bold**.

4.2.1 Investigation into type of surfactant

Different surfactants were investigated in order to gain a more stable emulsion and reduce aggregation rate. SDS, CTAB and TWEEN 61 were chosen due to their varying ionic properties and hydrophilic-lipophilic balance (HLB) values. SDS was found to produce the lowest levels of agglomeration (Table 10). A low level of agglomeration is required in order to produce discrete capsules rather than large lumps of agglomerated droplets. As SDS has the highest HLB value of 40, this would mean it has the greatest solubility in water and therefore produce the desired o/w emulsion. This could explain why the best results (small discrete spheres with the lowest level of agglomeration) were seen with SDS.

Table 10: A summary of the different surfactants explored and their properties. Observation by eye and via optical microscopy showed SDS had the most promise as it produced small discrete spheres with the lowest level of agglomeration.

Surfactant	Charge	HLB		
Sodium dodecyl sulfate	Anionic	40		
Cetyltrimethylammonium bromide	Cationic	10		
TWEEN 61	Non-ionic	9.6		

4.2.2 Investigation into core material

Polytetrahydrofuran (polyTHF) was first used as the discontinuous phase and showed good miscibility with the resin. Upon addition to the aqueous phase, a white emulsion was formed. Very few capsules were collected and the resulting filtrate was milky suggesting that much of the polyTHF was lost in the aqueous phase as an emulsion (Figure 62).

An epoxy resin EPON 828 was then used as the discontinuous phase and as with polyTHF, It too showed good miscibility with the resin. Upon addition to the aqueous phase, a clear emulsion was formed. The yield of capsules was much higher and the resulting filtrate was clear suggesting that only a small amount of the epoxy was lost in the aqueous phase as an emulsion (Figure 62).



Figure 62: (a) Filtrate obtained when epoxy was used as the encapsulated material. (b) Filtrate obtained when polyTHF was used as encapsulated material. This filtrate was found to be much milkier in appearance and which suggest that more polymer is present in the aqueous phase.

The preference for the polymer to mix with the resin or have a higher relative affinity for the aqueous phase than the resin can be explained by the chemical structure of the polymers, as shown in Figure 63. Polarity of the molecules, and the resulting hydrophilicity/ hydrophobicity, can be estimated from the prevalence of high electronegative atoms within the structure. The oxygen content of the polymers is shown in Figure 63. Not only does polyTHF have a higher

ratio by weight of oxygen, but the primary –OH groups terminating each end of the polymer chain allow for hydrogen bonding. This further increases the hydrophilicity of the polymer.

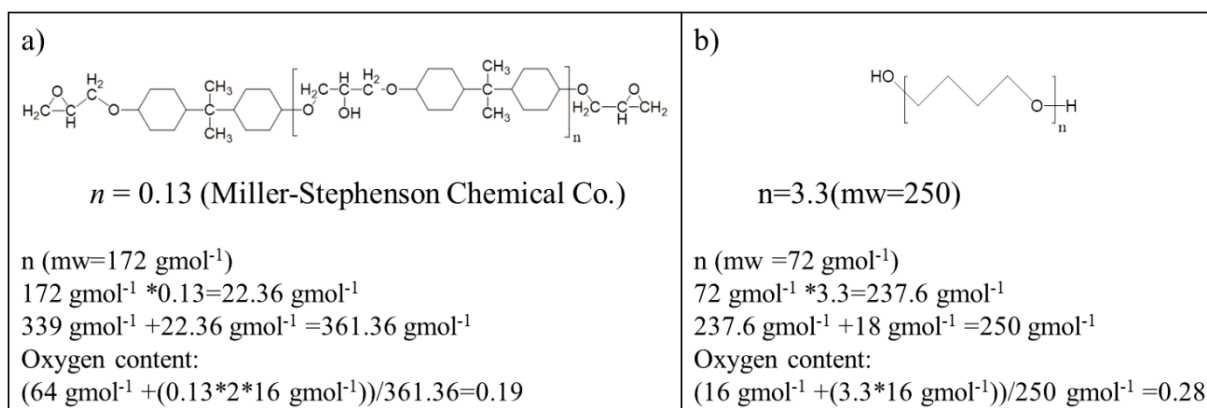


Figure 63: Chemical structure of a) EPON 828 epoxy resin and b) polyTHF mw-250. The oxygen content using weight ratio is shown for each molecule. The higher content of oxygen, an electronegative atom increases the relative polarity if the molecule. In addition, the –OH groups terminating each end of the polymer allow for hydrogen bonding which further increases the hydrophilicity of the polymer.

The capsules collected when using epoxy as the encapsulated material were transparent, however there was some clumping and the capsules were on the mm scale length in size, and thus far in excess of the target size of 100-200 μm diameter (Figure 64). Washing with isopropanol helped to remove any un-polymerised resin residue on the capsules which reduced the stickiness of the capsules. Further investigation of surfactant concentration and phase volume ratios could help improve the aggregated nature of the capsules and reduce the size.

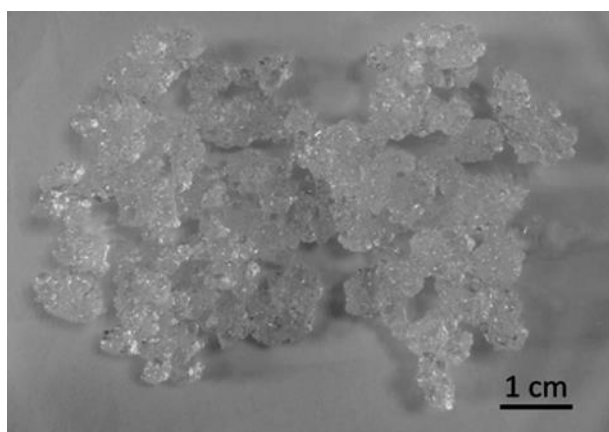


Figure 64: Capsules generated using EPON 828 as the encapsulated material. The capsules were transparent, but large ($>1000\ \mu\text{m}$) and aggregation was still an issue.

4.2.3 Investigation into surfactant concentration

The concentration of SDS was increased from 1 wt% to 2wt% and 5 wt%, to see if any improvement could be seen in aggregation rate. More discrete capsules could be isolated when using 2 wt% than 1 wt%, but there was still significantly large capsules collected with similar size and appearance to those shown in Figure 64. Increasing the concentration to 5 wt% however did not provide any significant improvement. An increase in surfactant concentration decreases the interfacial tension between the two phases, therefore coalescence of droplets is decreased and subsequent aggregation should also decrease.

4.2.4 Investigation into phase volume ratio

Alongside surfactant type and concentration, the volume ratio of the two phases can have an influence on the emulsion that will be formed. Generally the stability of the emulsion decreases with increasing volume ratio of the dispersed phase. If the volume of the dispersed phase is too high, phase inversion can occur. Therefore, the volume of the disperse phase was first decreased from 10 mL to 5 mL, followed by an increase in the volume of the continuous phase from 100 mL to 200 mL. More discreet capsules were produced however, the capsules were still large ($>1000\ \mu\text{m}$) with similar sizes to those described previously.

4.2.5 Investigation into mixing method

For the batch process the main issues were a lack of mechanical energy to break up the viscous mixture into discrete droplets, with low aggregation rates and a smaller droplet size.^{219,220} The main issue is that the capsules generated are too large, 500-1000 μm (ideally 100-200 μm needed). The mixing speed of the propeller method is limited by the max speed of the mechanical mixer and therefore other mixing methods need to be considered to produce smaller droplets. A magnetic stirrer bar was utilised. However, the resin mixture collected around the stirrer bar and was not effectively 'cut' by this mixing method. Homogenisation is a mixing method which utilises much higher shearing rates. A comparison of the different shear flow regimes of the mixing methods investigated is shown in Figure 65. Homogenisation alone provided the energy required to break up the viscous mixture, however the emulsion was unstable and after removing the homogenisation to place under the UV light, aggregation began to occur²⁰⁶ and the droplets fell to the bottom of the beaker (Figure 66). Aggregation began to occur upon stopping agitation. Use of the homogenisation mixing tool cannot be continued during the polymerisation process due to the high shear effect of this mixing method. In order to maintain some level of agitation, the propeller mixer was then used in conjunction with the homogenisation. This helped deter the droplets from falling to the bottom of the mixing vessel although the emulsion droplets still aggregated, and the resulting capsules were very polydisperse with many of the small droplets ($\sim 100 \mu\text{m}$) produced using homogenisation merging to form larger droplets (up to 500 μm). The size range required for this application is 100-200 μm . The majority of the capsules that were produced were therefore still too large.

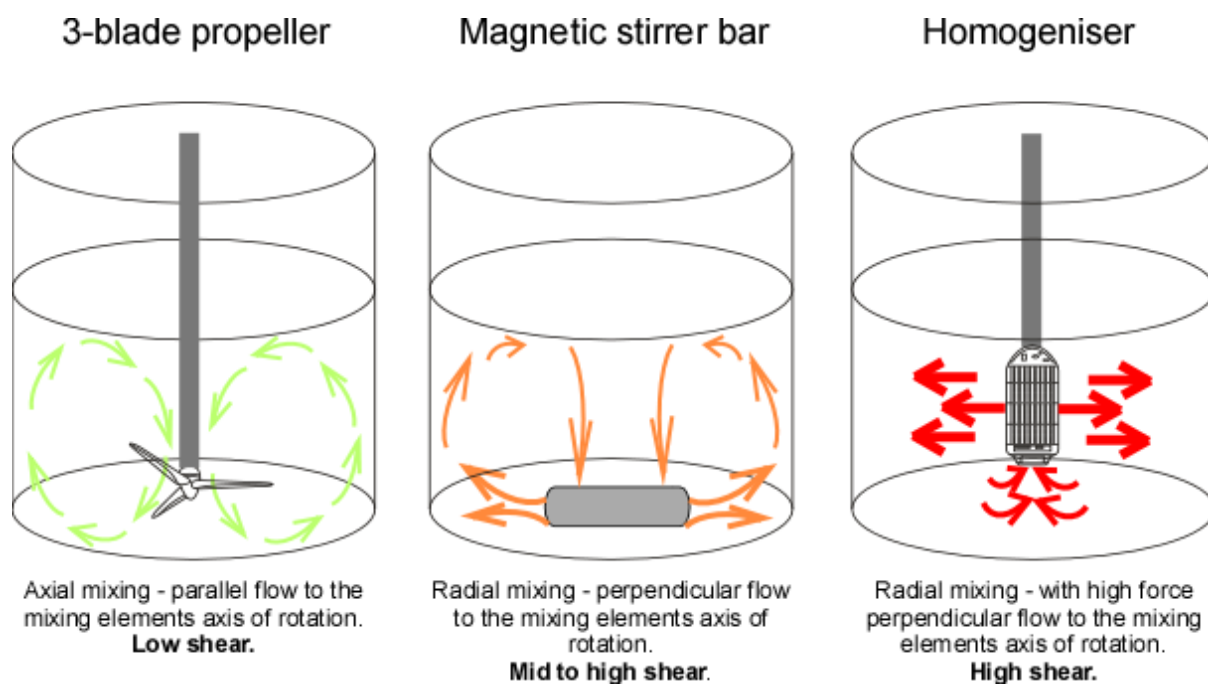


Figure 65: The shear flow regimes of different mixing methods. The propeller method resulted in the lowest shear due to axial mixing where the resulting flow is parallel to the mixing elements axis of rotation. Perpendicular flow from the mixing elements axis of rotation results in high shear with the homogeniser producing the largest level of shear.

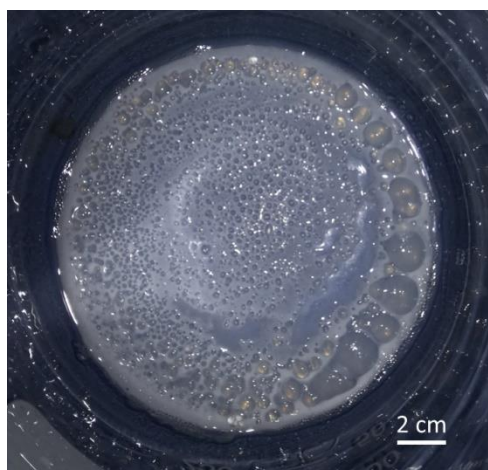


Figure 66: The capsules produced through homogenisation. Due to the lack of agitation during curing the emulsion fell to the bottom of the beaker and did not produce discrete capsules.

4.4 Conclusion to investigation into the production of capsules for transparent self-healing materials via traditional mixing methods

A method has been developed which can be optimised for different polymers which can be used to produce transparent microcapsules. If the polymer encapsulated using this method is RI matched to the shell and matrix material this could produce materials with embedded capsules which are optically transparent. Further experiments could show how this method could be produce extrinsically self-healing materials. It is also to be explored that due to the fast UV induced polymerisation of the matrix material; these materials could also be used in SLA 3D printers.

5. INVESTIGATION INTO THE PRODUCTION OF MICROCAPSULES FOR USE IN TRANSPARENT SELF-HEALING MATERIALS THROUGH UTILISATION OF MICROFLUIDIC DEVICES

In this chapter, the utilisation of microfluidic devices to generate capsules in conjunction with 3D printing to produce self-healing materials is reported. The use of microfluidic devices to produce microcapsules has many possible advantages over the batch methods described in chapters 3 and 4. These include the possibility to produce homogeneous capsule sizes through precisely controlled droplet production on-chip. The sequential nature of droplet production and extrusion may also provide an elegant solution to agglomeration problems noted in the batch processes explored in Chapter 4.

5.1 Preliminary droplet studies

Preliminary studies were carried using design MD1 (device details provided in section 2.15.1) to demonstrate the control afforded when utilising microfluidic devices for droplet generation. For these preliminary experiments, the continuous phase consisted of water, sodium dodecyl sulfate (SDS) surfactant and blue food dye (details provided in section 2.7). The dispersed phase was chloroform and was kept at a constant flow rate of $1 \mu\text{L min}^{-1}$. The flow rate of the continuous phase was increased from 10 to $30 \mu\text{L min}^{-1}$ (Figure 67). As can be seen in the figure good correlation was seen increasing continuous phase flow rate and a decrease in droplet size. This shows that droplets size that be tightly controlled when using this production method. This trend is expected from the literature.²²¹

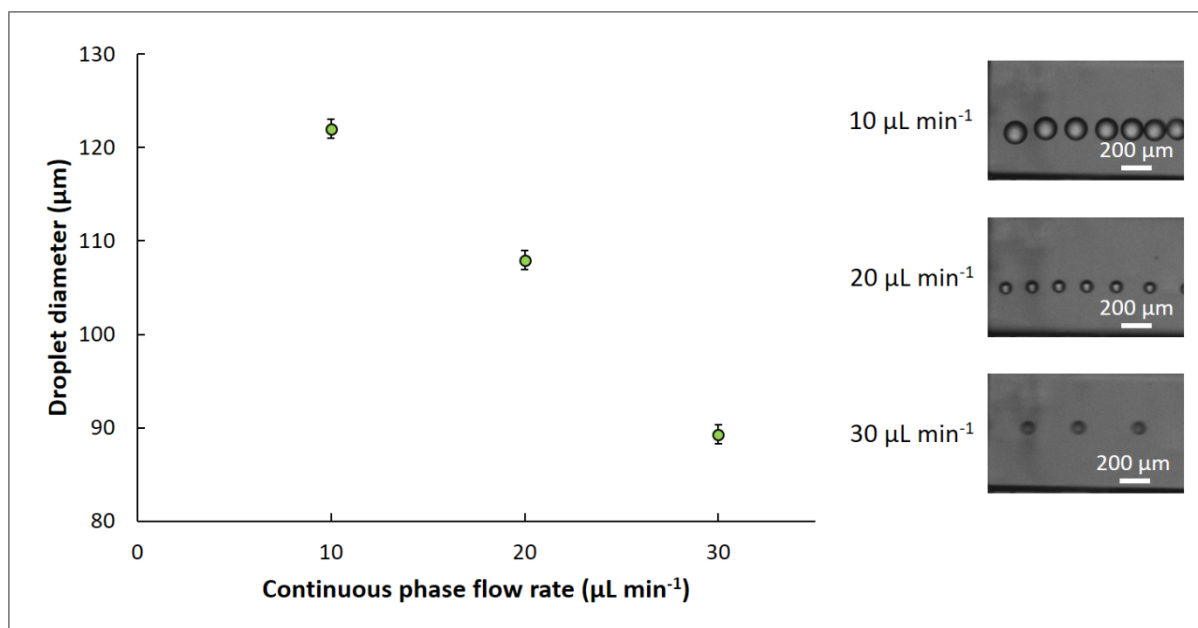


Figure 67: The effect increasing the continuous phase flow rate on droplet size. As expected from the literature, the droplet size can be tightly controlled through the flow rate ratio of the continuous and discontinuous phases. ($n=10$)

5.2 Utilisation of glass microfluidic devices for production of self-healing capsules

It was hypothesised that capsule production using the combination of the self-assembly core-shell structure and UV polymerisation chemistry described in Chapter 4 for batch reactions could be improved upon when working with microfluidic droplet devices (Figure 68). The major issue with regards to the production of transparent self-healing capsules for the batch process was the agglomeration of capsules. Flow focussing microfluidic channel structures produce droplets of controlled size and inter-droplet distance, one at a time, by the exploitation of the droplet generating mechanism described in section 1.3. This could therefore be a solution for the agglomeration problems.

Figure 68 shows the production of droplets consisting of a mixture of polymerisable resin and an epoxy monomer. Emulsification in an aqueous continuous phase allows for a core-shell

structure to form within the droplets, with the UV polymerisable resin preferentially moving to the water interface. This is accomplished due to the relative hydrophobicity of the Photocentric resin and the core polymer. Exposure to a UV light source will polymerise the resin to form the shell wall material of the capsules.

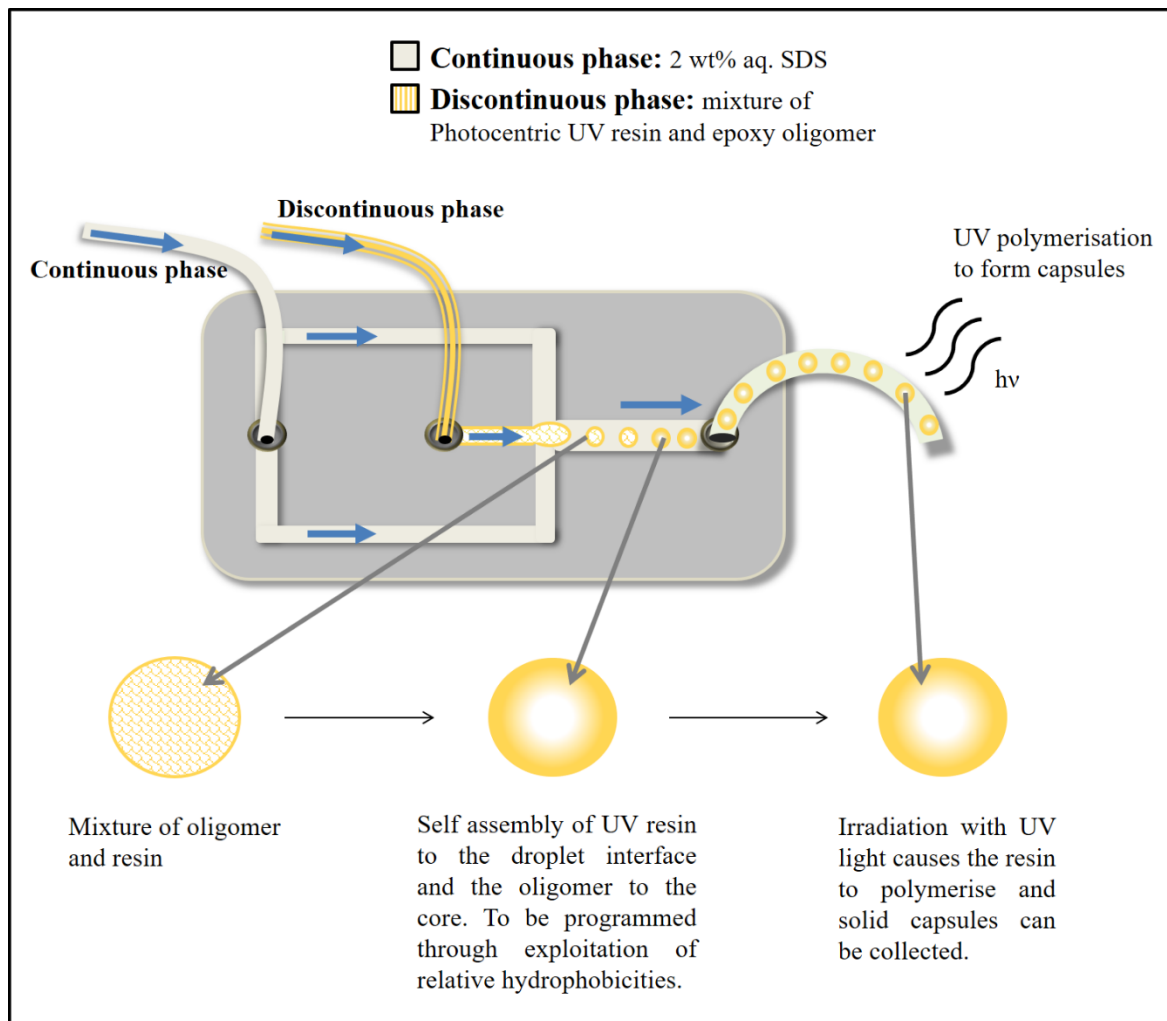


Figure 68: Schematic representation of microfluidic production of capsules, using design MD2; blue arrows show the direction of flow. MD2 is a glass device with flow focusing junction to produce droplets. The phase separation reaction chemistry described in chapter 4 was to be applied here. The relative hydrophobicity of the Photocentric resin and the core polymer allows for the self-assembly of the core shell structure within the droplet. Exposure to a UV light source will polymerise the resin to form the shell wall material of the capsules.

5.2.1 Investigation into flow rate

Droplets were produced using design MD2 (device details provided in 2.15.1, experimental details provided in section 2.7). The first experiments involved the use of a discontinuous phase with a mixture of EPON 828 epoxy and Photocentric resin at a set ratio of 1:4. The continuous phase was a 2 wt% SDS aqueous solution. Examples of droplets generated on this device using this ratio are shown in Figure 69. Droplet generation was stable, with the produced droplets being spherical and homogeneous in size and shape.

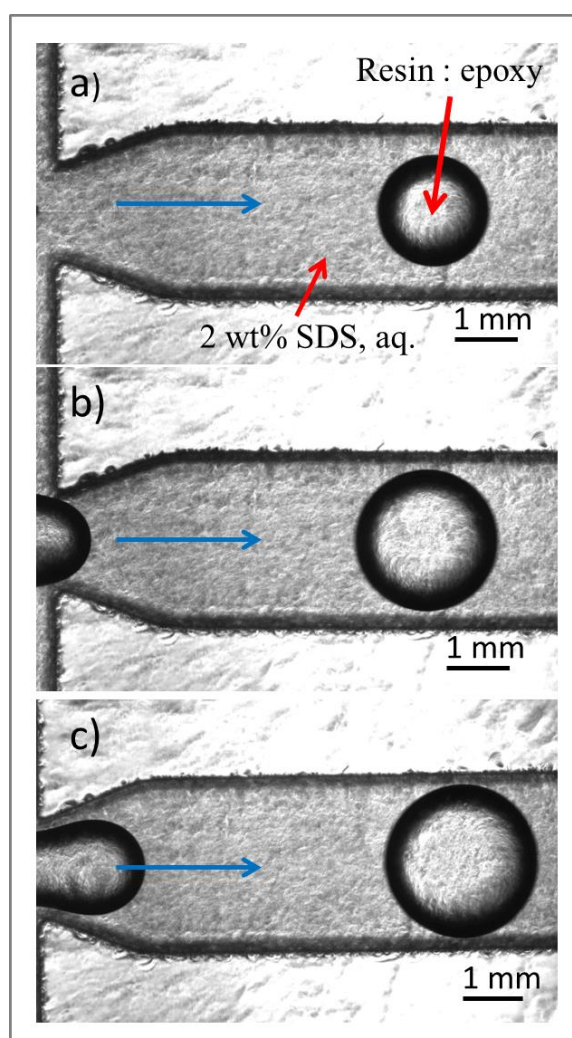


Figure 69: Examples of the droplets generated using MD2 with a discontinuous phase consisting of EPON 828 epoxy resin and Photocentric resin at a ratio of 1:4 and a continuous phase of 2 wt% SDS aqueous solution. Blue arrows indicate the direction of flow. For the droplets shown, the continuous flow rate was fixed at 40 mL h^{-1} . The discontinuous flow rate was varied, a) 0.25 mL h^{-1} b) 1 mL h^{-1} and c) 1.75 mL h^{-1} . With increasing flowrate of the discontinuous phase, it can be seen that the droplets generated get larger in diameter.

The effect of changing the flow rates has on the obtained droplet sizes was investigated. In an initial set of experiments, the DP flow rate was increased between 0.25 mL h^{-1} and 1.75 mL h^{-1} , whilst maintaining the CP flow rate at 20 mL h^{-1} , 30 mL h^{-1} or 40 mL h^{-1} . The obtained droplet sizes are plotted in Figure 70. It can be seen, that droplet size increased with increasing discontinuous flow rate. This is in line with what is reported throughout the literature with other less viscous materials.²²¹ This suggests that droplet generation is still largely dependent on Ca . As seen in Equation 6, which shows droplet size is inversely proportional to the velocity of the continuous phase and therefore an increase in the discontinuous phase will decrease the flow rate ratio with regards to the continuous phase leading to larger droplet size.

As can also be seen from Figure 70, when keeping the dispersed phase flow rate fixed, the droplet size was found to decrease with increasing the continuous flow rate. As previously discussed with regards to changing the dispersed phase flow rate (section 1.4.4), this is in line with what is expected for droplet generation which is controlled by Ca . This agrees with what is reported in the literature for other viscous (18 mPas) discontinuous liquids in droplet devices.²²²

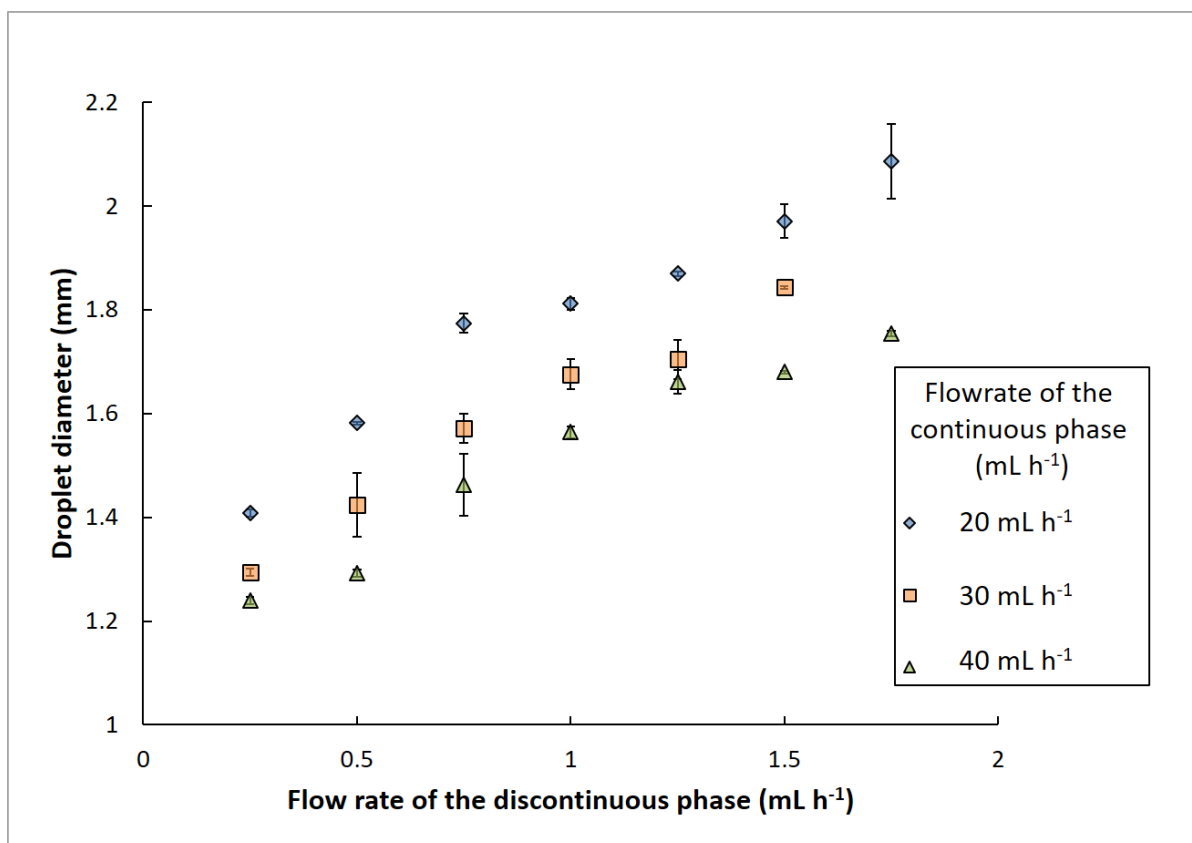


Figure 70: Droplet size dependence on the continuous and discontinuous flow rates. The droplet size increased with increasing discontinuous flow rate. The continuous flow rate was also investigated, the droplet size decreased with increasing continuous phase flowrate at any fixed discontinuous phase. The continuous phase was a 2 wt % SDS aqueous solution. The discontinuous phase was an EPON 828 and Photocentric firm resin using a 1:4 ratio ($n = 10$).

5.2.2 Investigation into composition and viscosity of discontinuous phase

Droplets were produced using design MD2 (device details provided in section 2.15.1, experimental set-up described in section 2.7). The Photocentric resin has a viscosity of 230 mPa s, however upon addition of the epoxy resin this vastly increases due to the far higher viscosity of the EPON 828 epoxy resin which is 11,000 mPa s. Despite the relatively high viscosity of the dispersed phase, coupled with a large difference in viscosities between the dispersed and continuous phases, droplet generation followed the same pattern of behaviour seen throughout the literature using liquids with low viscosities as discussed in section 1.3.

As well as having a high viscosity, the droplet regime of this particular mixture is of interest as the complex rheological behaviour found in polymer blends has been studied relatively little in the literature. High viscosity liquids investigated so far have been limited to single component phases¹⁹⁶ and Newtonian liquids¹⁹⁸ both of which simpler rheological properties compared to the polymer mixture studied in this project. Our initial findings suggest that the theory on droplet generation using microfluidic devices could be extended to cover liquids with a much wider range of viscosities and rheological properties than previously seen in the literature; at least, when the high viscosity component is the discontinuous phase as in this case.

As well as exploring the effect of the discontinuous and continuous flow rate regimes on droplet generation, the effect of composition of discontinuous phase was also investigated. In order to use these devices to produce microcapsules with liquid polymer cores, the core to shell ratio may need to be adjusted for optimisation. The effect of increasing the core content on droplet generation was therefore investigated. The ratio of Photocentric UV curable resin to EPON 828 epoxy resin was varied between 1:4, 1:2 and 3:4 and the resulting droplet size was studied. The flow rate of the continuous phase was maintained at 30 mL h⁻¹. From Figure 71 it can be seen that, for a given ratio of resin to epoxy, the size of the droplets can be tuned by varying the flow rates of the incoming phases; increasing the flow rate of the dispersed phase led to the generation of larger droplets as found before (see Figure 71). More importantly, it was found that increasing the ratio of epoxy to resin from 1:4 to 1:2 led to an increase in average droplet size. This increase in droplet size with increasing epoxy content is most likely due to the increase in viscosity of the mixture. As discussed in section 1.3.4, due to the channels and small amounts of liquid, droplet generation within microfluidic devices, even with more viscous liquids, is widely controlled by the dimensionless capillary number, Ca . Looking at Equation 6, Ca is proportional to the viscosity of the continuous phase, μ . This viscosity ratio of the continuous phase to the discontinuous phase will decrease with increasing discontinuous phase

viscosity. Therefore, the increase in epoxy within this mixture and subsequent increase in viscosity will cause the value of Ca to decrease. This would explain why the change in viscosity has such a dramatic effect on the droplet size generated as seen in Figure 71. This was further shown when the ratio of epoxy to resin was increased to 3:4. The discontinuous phase became very viscous; the blend of polymers also expressed more non-Newtonian flow behaviour, showcasing viscoelastic properties. Stable droplet generation was very difficult to achieve at the flow rates previously used, with either laminar flow or long threading before droplet pinch could be achieved (Figure 72).

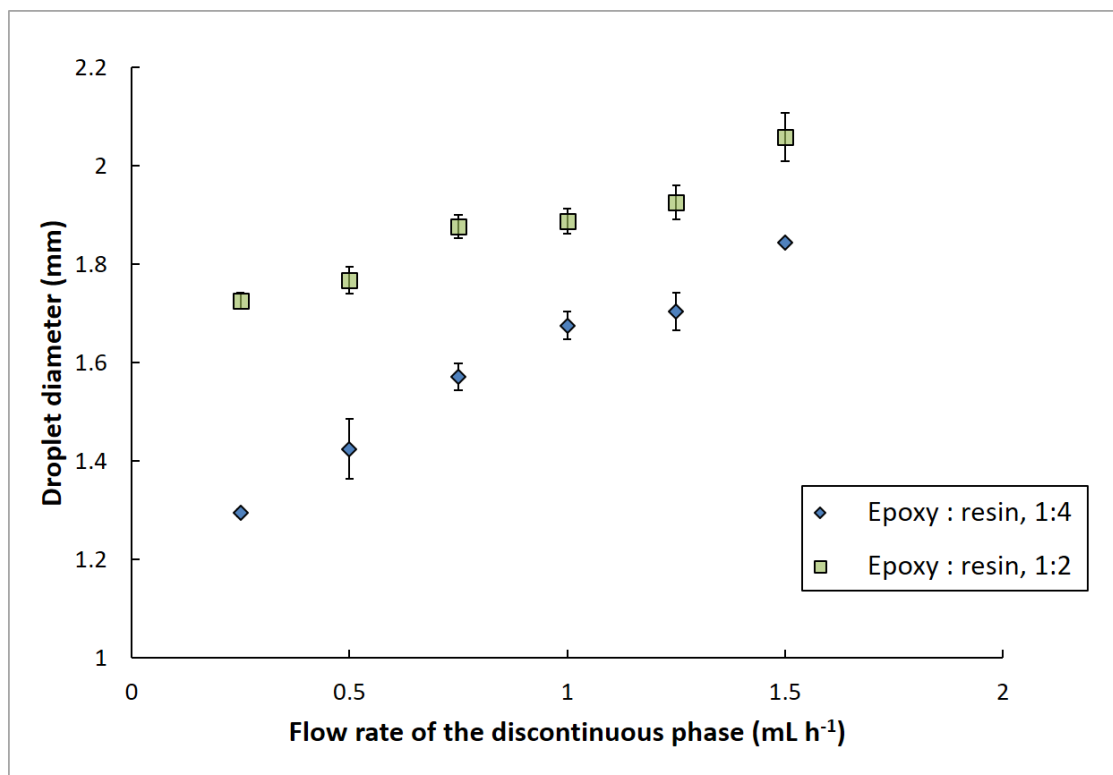


Figure 71: Droplet size dependence on the discontinuous flow rates and the resin : epoxy mixture ratio. The droplet size increased with increasing discontinuous flow rate. The mixture ratio was also investigated, the droplet size increased with increasing epoxy content at any fixed discontinuous phase. The discontinuous phase was an EPON 828 and Photocentric firm resin using a 1:4 or 1:2 ratio. The continuous phase was a 2 wt % SDS aqueous solution with a flow rate of 30 mL h⁻¹. (n = 10)

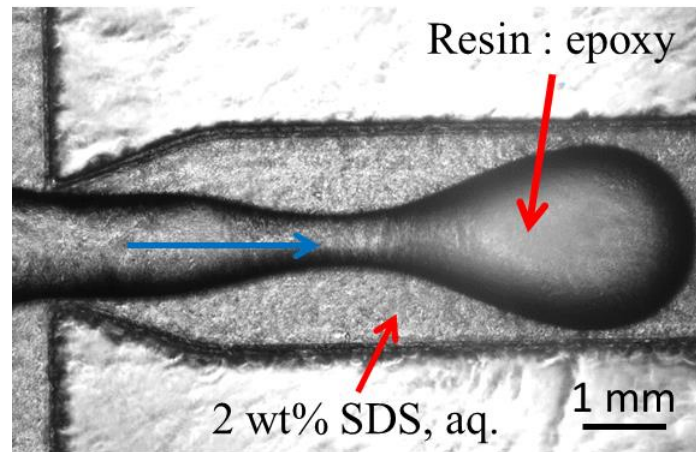


Figure 72: Unstable droplet generation seen with increased viscosity of discontinuous phase. Blue arrow indicates direction of flow. The threading effect can be seen which delays the ‘pinch off’ point for droplet generation beyond the junction and into the channel. This leads to unstable droplet generation with little control over droplet size. The discontinuous phase was an EPON 828 and Photocentric firm resin mixture with 3:4 ratio, with a flow rate of 0.5 mL h^{-1} . The continuous phase was a 2 wt % SDS aqueous solution with a flow rate of 30 mL h^{-1} . ($n = 10$)

To counteract the negative effect of increased viscosity of the discontinuous phase on stable droplet generation, the flow rate of the continuous phase was increased to observe if stable droplet generation could be achieved. Again when looking at the equation for Ca (Equation 6), as well as a proportional relationship with the viscosity of the continuous phase, there is a proportional relationship to the flowrate. Increasing flow rate should therefore produce smaller droplets and more stable droplet generation. The flow rate of the continuous phase was therefore increased to 50 mL h^{-1} , the flowrate of the discontinuous phase was carried used between $0.25 - 1 \text{ mL h}^{-1}$. Droplets were produced in a more stable fashion and the sizes shown in Figure 73. For comparison, the resin mixture with a ratio of 1:2 was also repeated at these flow rates. The results show a continuation of the trends observed previously in this work and in the literature; mainly that upon increasing the flow rate of the discontinuous phase the droplet size increased.

Increasing the assumed viscosity of the discontinuous phase mixture by increasing the volume ratio of the viscous epoxy also resulted in higher droplet diameter at comparable flow rates when compared to lower viscosity mixtures.

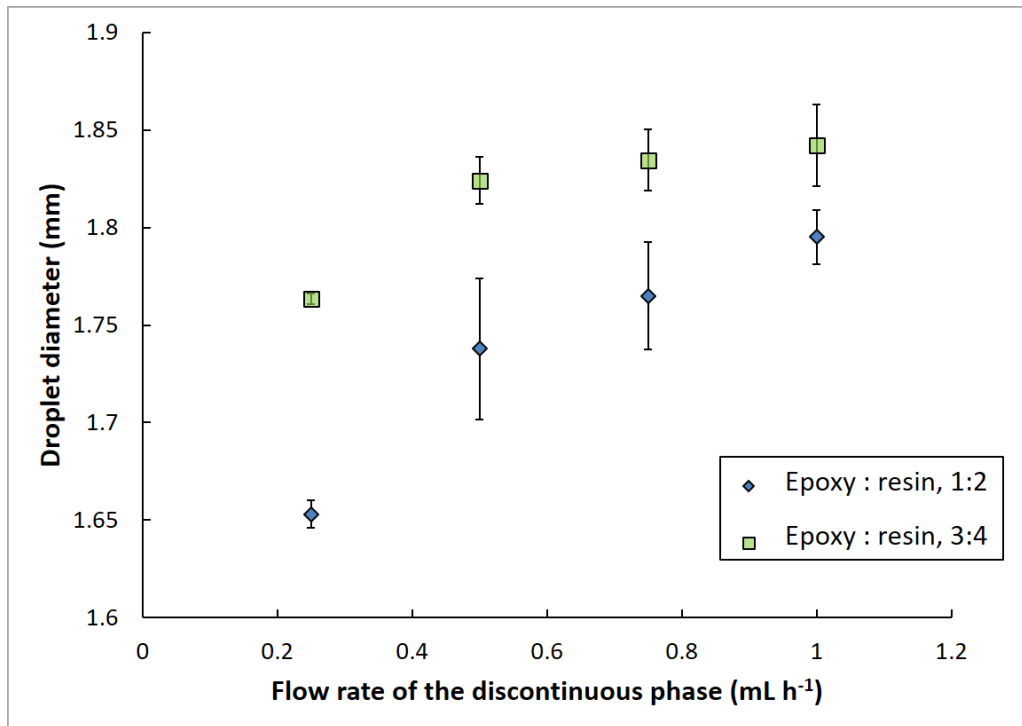


Figure 73: Droplet size dependence on the discontinuous flow rates and the resin : epoxy mixture ratio. The droplet size increased with increasing discontinuous flow rate. The mixture ratio was also investigated, the droplet size increased with increasing epoxy content at any fixed discontinuous phase. The discontinuous phase was an EPON 828 and Photocentric firm resin mixture using a 1:2 or 3:4 ratio. The continuous phase was a 2 wt % SDS aqueous solution and the flow rate was maintained at a higher flow rate when compared with previous experiments at 50 mL h⁻¹. This was necessary due to the increased viscosity of the discontinuous phase and the disruption of droplet generation this caused. (n=10)

5.2.3 Investigation into the viscosity of the continuous phase

Until this point, droplet generation has been controlled by variation of low rates alone. Considering the effect observed upon increasing the viscosity of the discontinuous phase only, it was thought that increasing the viscosity of the continuous phase in order to bring the viscosities of the two phases back to being more closely matched could increase the stability of droplet generation.

Therefore, droplets were produced using chip design MD2 (device details provided in section 2.15.1, experimental set-up shown in section 2.7). The non-Newtonian nature of the polymer blend within the discontinuous phase means that no fixed viscosity can be measured. It was assumed that an overall increase in viscosity is experienced upon addition of more epoxy which is why an increase in droplet size and break-off instability as described in 5.2.2 was observed. The threading also suggests that the viscoelastic properties have become too great to overcome through flow rate variation alone. Fixing the flow rates and polymer mixture ratio allowed us to investigate the effect of increasing the viscosity of the continuous phase as well.

Through addition of poly(ethylene glycol) (PEG) to the continuous phase different viscosities were investigated (0.89-129 mPa s). The discontinuous phase polymer blend ratio was fixed at 1:2. 0.25 and 50 mL h⁻¹ were used for the flow rates of discontinuous and continuous phases, respectively (Figure 74). Droplet size was found to decrease with increasing continuous phase viscosity (0.89 - 129 mPa s) which agrees with what was predicted when looking at Equation 6.

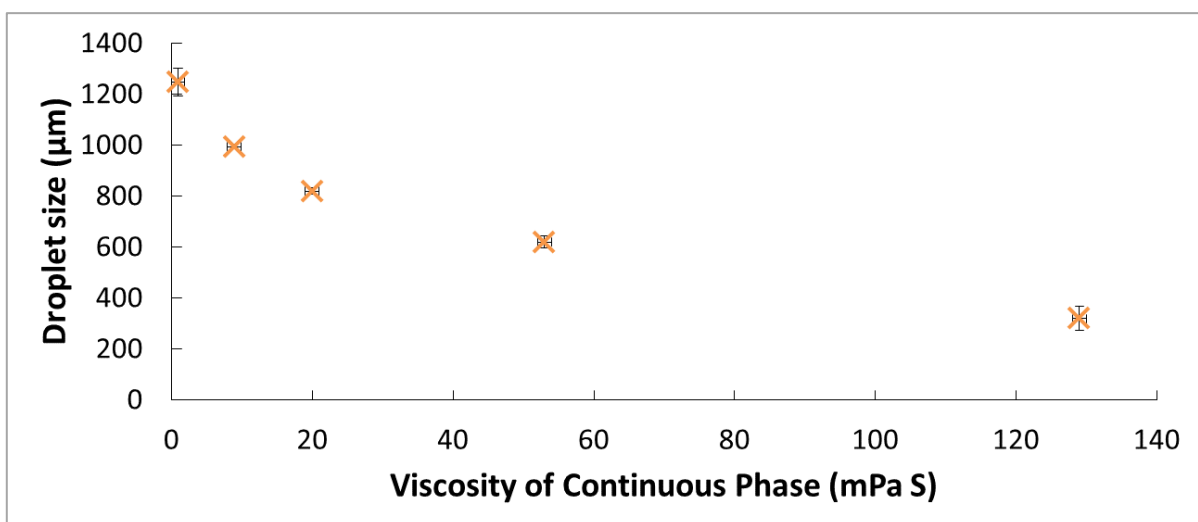


Figure 74: Effect of varying viscosity of the continuous phase (0.89-129 mPa s) via addition of PEG. The discontinuous phase polymer blend ratio was fixed at 1:2. 0.25 and 50 mL h⁻¹ were used for the flow rates of discontinuous and continuous phases, respectively. The polydispersity of the droplets increased with increasing viscosity as the formation of satellite droplets increased. (n=10)

It was noted, that as the viscosity of the continuous phase approached the assumed viscosity of the polymer blend (50 wt% PEG with viscosity 330 mPa s) droplet break-off occurred further down the channel and the formation of satellite droplets was seen (Figure 75).

The resulting satellite droplets completely broke from the parent droplets resulting in a higher polydispersity (Figure 76). Looking at figure 74, it can be seen that the standard deviation in droplet size increased with increasing continuous phase viscosity as the prevalence of satellite droplet formation increased.

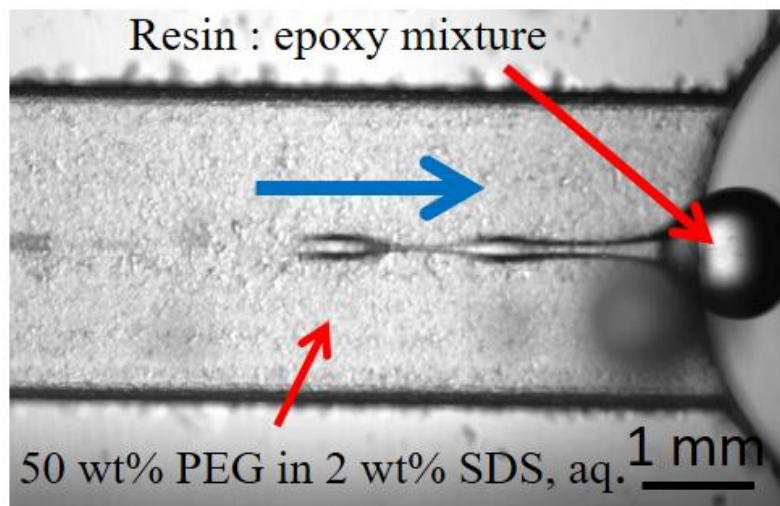


Figure 75: Satellite formation observed when the viscosity of the continuous phase (330 mPa s) approached that of the polymer blends. Blue arrow indicates the direction of flow. The discontinuous phase polymer blend ratio was fixed at 1:2. 0.25 and 50 mL h⁻¹ were used for the flow rates of discontinuous and continuous phases, respectively.

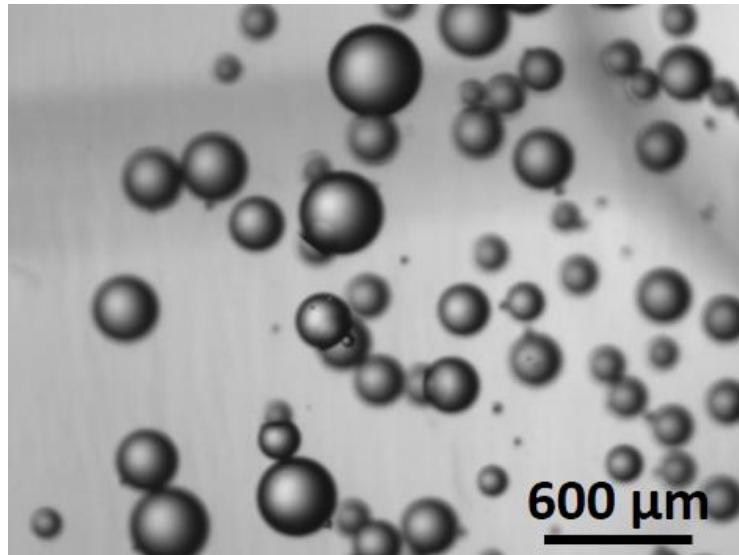


Figure 76: A mixture of parent and satellite droplets collected when a high viscosity continuous phase was utilised. An average droplet size of 300 μm . The discontinuous phase polymer blend ratio was fixed at 1:2. 0.25 and 50 mL h^{-1} were used for the flow rates of discontinuous and continuous phases, respectively.

5.2.4 Conclusion into the use of glass devices for the production of self-healing capsules

As outlined in 5.2.2 and 5.2.3, a series of experiments varying flow rates and phase viscosity ratios were carried out to try and address the issues raised during the batch process in Chapter 4. These included too large capsule size and agglomeration of droplets before the polymerisation step can take place.

For the self-healing applications intended for these materials the polydispersity introduced by the satellite droplets is not too much of an issue and with an average droplet size of 300 μm , this is a good size for self-healing. Within the literature, capsules utilised in self-healing materials vary in size from 1~350 μm . However, for SLA 3D printing, a layer height of 200 μm is utilised. Therefore, the capsules are still too large.

A second issue was identified when polymerisation of the droplets for capsule formation was attempted. The Photocentric resin utilised can be very quickly polymerised and it was hoped that polymerisation could occur on the chip or shortly after exiting the chip within the outlet

tubing, in order to avoid the agglomeration issues seen when using a batch process (Chapter 4). However, it was found that polymerisation within the glass channels resulted in blockages as the polymerised resin would stick to the glass channel walls. Polymerisation within the outlet tubing was also found to lead to similar blocking problems.

5.3 Utilisation of PDMS microfluidic devices for production of self-healing capsules

Previously within this chapter, all droplets were generated using a glass flow device (design MD2). This proved to be unsuitable for polymerisation of the droplets on-chip due to the prevalence of the polymerised resin sticking to the glass channel walls. It was theorised, that a flow cells fabricated from PDMS might overcome these issues. PDMS is gas permeable, which should therefore allow a cushioning layer of oxygen to be present at the channel walls of the microfluidic device when in use (Figure 77). Oxygen inhibition of radical polymerisation^{223,224} (which is the process utilised here) should mean that polymerisation of the droplets using a PDMS device may prevent polymerisation occurring at the channel walls²²⁵ and therefore reducing the sticking effect seen when using glass. This concept is utilised within SLA printers, which use a thin layer of PDMS at the bottom of the build tanks to prevent sticking of the polymerised resin.^{226,227}

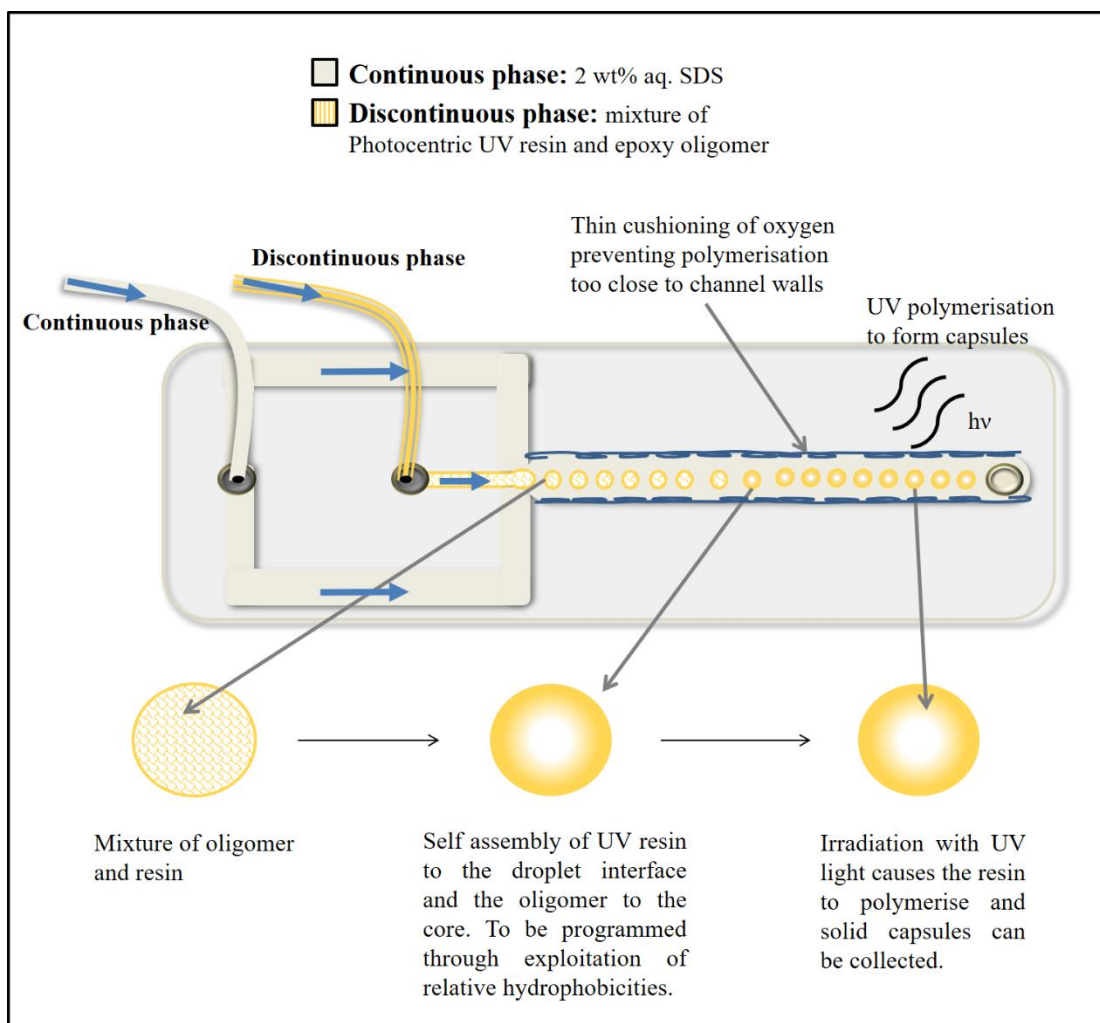


Figure 77: Schematic representation of microfluidic production of capsules, using MD4; blue arrows indicate the direction of flow. MD4 is a PDMS device which utilises a fluid focusing junction to produce droplets. The same chemistry used in chapter 4 is applied here. The relative hydrophobicity of the Photocentric resin and the core polymer allows for the self-assembly of the core shell structure within the droplet. Exposure to a UV light source will polymerise the resin to form the shell wall material of the capsules. The application of a PDMS device should prevent polymerisation of the resin to occur too close to the channel walls. A longer outlet compared to that of MD2 outlined in Figure 43 should also allow for more time for the phase separation process to occur.

5.3.1 Utilisation of a PDMS device with the same dimension as MD2

A design which mimicked the dimensions of the glass device previously used (MD2) was investigated (MD3). The design and fabrication of which is outlined in the experimental section (found in section 2.15.2). The experimental set-up was the same as those for previous microfluidic droplet generation experiments and is found in section 2.7. The discontinuous phase polymer blend ratio was fixed at 1:2, epoxy to UV polymerisable resin. The same flow rates, 0.25 and 50 mL h⁻¹ were used, and the droplet size compared with glass device (Figure 78). A slightly smaller average droplet size was produced with MD3, probably due to the channel shape which is determined from the manufacturing process, *i.e.* CNC milling for MD2 and the Form 2 printer for MD3. There was also a much larger standard deviation observed for droplets generated in the MD3. This could be due to the nature of PDMS as it is a flexible material and therefore the channel shape could become deformed when under pressure. Within these margins of error, the droplet size produced by the devices was comparable at the same flow rates. As discussed at the end of section 5.2, it was therefore deduced that the same issue with regards to too large of a droplet size would be seen within these devices too.

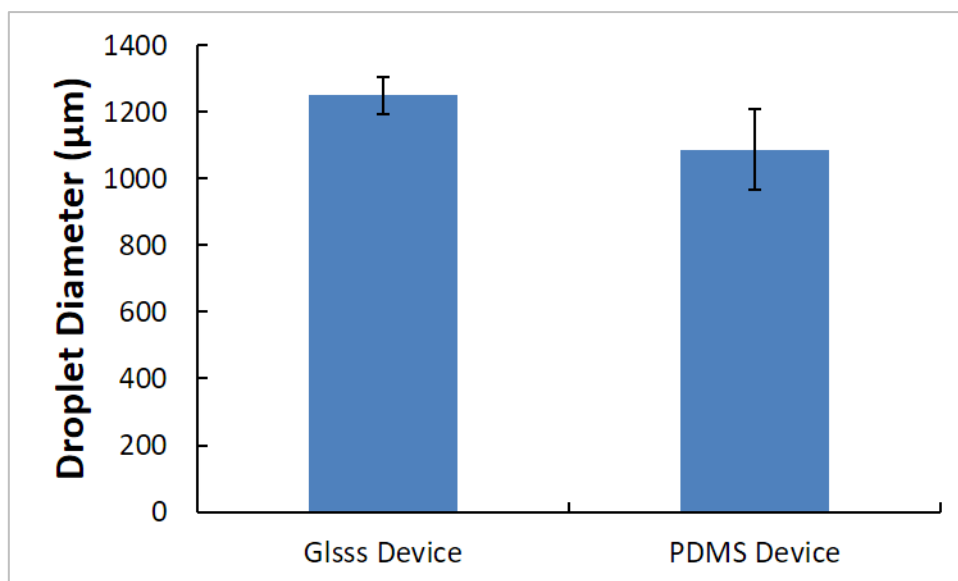


Figure 78: Average droplet size of droplet produced using a CNC milled glass device (MD2) and a PDMS device with the same dimensions (MD3). Continuous phase flow rate was 50 mL hr⁻¹ and the discontinuous phase flow rate was 0.25 mL hr⁻¹. The discontinuous phase polymer blend ratio was fixed at 1:2, epoxy to UV polymerisable resin. A smaller droplet size was produced using the PDMS device, which could be due to a slightly different channel shape occurring due to the different manufacturing methods. A much larger error was also observed for the PDMS device opposed to the glass, possibly due to the flexibility and deformation of the PDMS. (n=10)

A large droplet size would not only limit the use of these capsules within 3D printing, but another issue for the large droplet was the phase separation within the polymer blend. Within the literature, this phase separation process is size dependant; larger droplets will require more time for the phase separation to take place.^{228,229} As described in Figure 77, the self-assembly of the polymerisable resin towards the water droplet interface and the epoxy resin at the core is required for successful capsule formation. Observation of the large droplets show the phase separation process, with the UV resin ‘coating’ the more hydrophobic epoxy, this process is seen in Figure 79. For further optimisation of these devices, we required a PDMS chip, with narrower channels to produce much smaller droplets, combined with a longer outlet channel. This should produce smaller droplets which can be utilised in the 3D printing and allow the phase separation to take place before UV polymerisation.

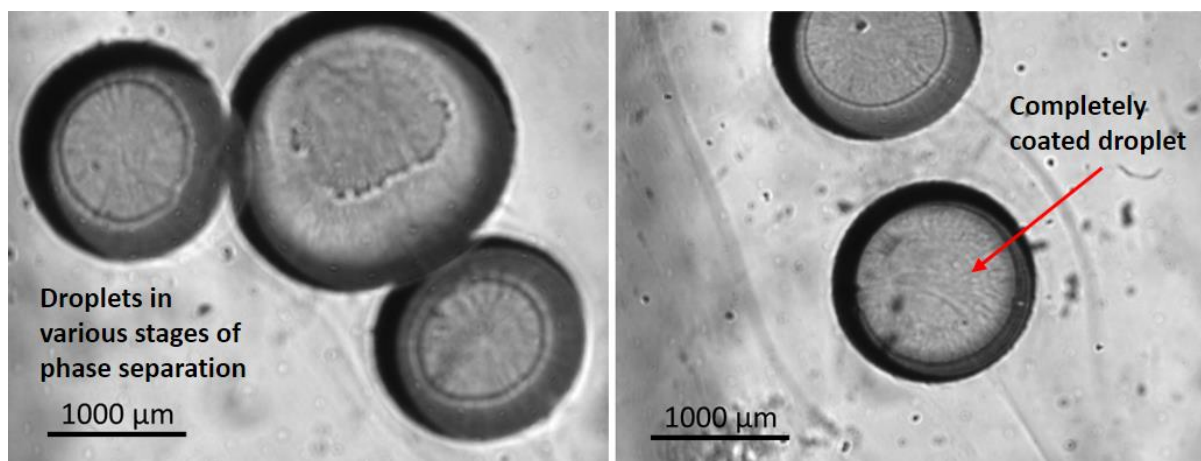


Figure 79: Optical microscope images of droplets produced with epoxy and UV resin mixture. Development of core-shell structure was noted through the phase separation of the epoxy and the less hydrophobic UV resin. The discontinuous phase polymer blend ratio was fixed at 1:2, epoxy to UV polymerisable resin. Dispersed and continuous flow rates used were 0.25 and 50 mL h⁻¹.

5.3.2 Utilisation of a PDMS device with narrower channels and longer outlet

A final microfluidic device was designed with narrower channels and a long outlet channel, MD4 (device details provided in section 2.15.2). The device dimensions were reduced by a factor of 2 when compared to the dimensions of MD2 and MD3.

The device was tested with the flow rate of the discontinuous phase maintained at 0.35 mL h⁻¹ and the flow rate of the continuous phase varied between 20 and 30 mL h⁻¹ (experimental set-up described in section 2.7). The polymer blend ratio was maintained at 3:4, epoxy to UV polymerisable resin. The results are plotted in Figure 80. As expected, the smaller channel dimensions produced much smaller droplets. For example, at 20 and 0.35 mL h⁻¹ for the continuous and discontinuous flow rates respectively, a droplet size of 250 μm was measured. Comparatively, with MD2 at similar flow rates, a droplet size of 1,400 μm was measured.

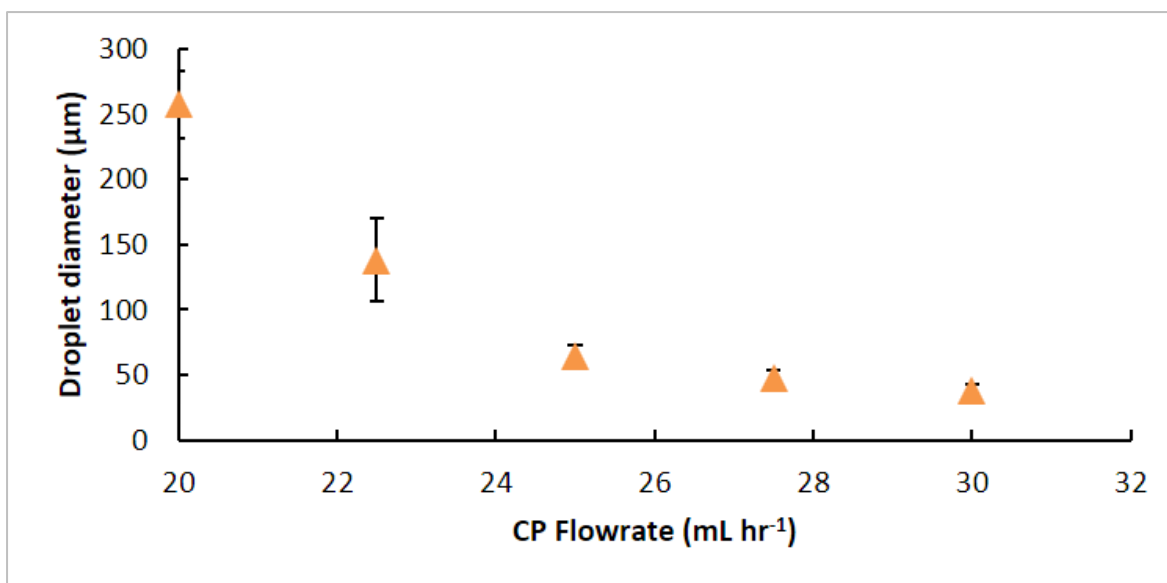


Figure 80: The effect increasing the continuous phase flow rate on droplet size using MD4. The droplet size is much smaller than those produced by devices utilised previously. The flow rate of the discontinuous phase was maintained at 0.35 mL h⁻¹. and the flow rate of the continuous phase varied between 20 and 30 mL h⁻¹. The polymer blend ratio was maintained at 3:4, epoxy to UV polymerisable resin. (n=10)

The droplets were observed within the channel of the PDMS devices. Compared to the glass device MD2, the PDMS devices, MD3 and MD4 both produced droplets with a much larger size variation. For example, looking at Figure 78, where both MD2 and MD3 used the same flow rates, droplet size had a 4% standard deviation error in MD2 and an 11% standard deviation error in MD3. This increased variation within the PDMS devices was theorised to be due to the manufacturing process and the flexibility of the PDMS material. Figure 81 shows the uneven channel walls within these devices.

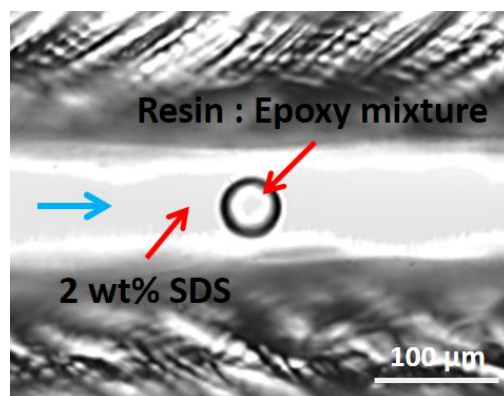


Figure 81: Droplet produced using MD4. The uneven channel walls can be seen clearly in this image.

The phase separation issues described in Figure 79 were not observed when using MD4. This could be due to this effect occurring much more rapidly due to the small droplet size. The effect was noted over a time period of a few seconds when the droplets were over 1,000 μm . The droplets produced by MD4 were only 40-250 μm . The phase separation would therefore occur much more rapidly.

The use of MD4 most importantly allowed for the production of droplets that would be compatible with the 3D printing process. All previous synthesis methods produced droplets that were larger than the 200 μm layer height. By utilising a continuous flow rate of 22.5 mL h^{-1} and a discontinuous flow rate of 0.35 mL h^{-1} an ideal droplet size of 138 μm was achieved.

5.3.3 UV Polymerisation of microfluidic produced droplets

The experimental set-up for the polymerisation of droplets to produce capsules is described in the experimental section 2.7. Flow rates of 22.5 mL h^{-1} and 0.35 mL h^{-1} were used for the continuous and discontinuous phases, respectively. Using these conditions, capsules with an average diameter of 138 μm were produced. The capsules were successfully polymerised within the outlet channel of MD4. There have been some issues noted with the light scattering properties of PDMS with regards to UV polymerisation within the literature.^{230,231} This could lead to undesirable polymerisation of the polymer within the inlet before droplet formation can

occur leading to clogging of the device. Aluminium foil was utilised around the inlet tubing and at the junction area, as well as foil covered screens which ensured that polymerisation of the resin only occurred within the outlet channel and collection dish. Capsules could be produced for at least one hour continuously using this set-up.

5.4 Conclusion to investigation into the production of capsules for transparent self-healing materials through utilisation of microfluidic devices

Droplets which contain a high polymeric content have been generated on microfluidic devices and it has been shown that a large degree of control over droplet size is possible. Various devices made of glass and PDMS were investigated for their suitability with regards to droplet size and application for polymerisation of capsules using a UV light source. Using the PDMS device MD4, transparent solid capsules with a diameter of 138 μm were generated, which were a suitably sized candidate for use in a transparent self-healing materials.

The use of these capsules within SLA 3D printing resins would be desirable due to their transparent properties which could improve the resolution of the prints by decreasing any light scattering that could be caused by the presence of self-healing capsules. This could also improve the final look of the print which would retain its transparent optical properties which upon addition of urea-formaldehyde capsules utilised previously, is lost significantly.

6. MICROFLUIDIC-ASSISTED PRODUCTION OF TRANSPARENT EXTRINSICALLY SELF-HEALING MATERIALS FOR 3D PRINTING

A technique of combining UV-curable resin embedded with microfluidically produced microcapsules containing RI matched liquid oligomers in conjunction with SLA 3D printing was used to construct transparent user-defined 3D structures with self-healing capability (Figure 82).

The self-healing employed in this work follows a solvent welding mechanism, as illustrated in Figure 82 and is described in full detail in section 1.2.3. When a crack occurs and ruptures a capsule along the propagation pathway, the oligomer within the capsule is released into the crack interface. Diffusion of the liquid oligomer promotes molecular chain entanglement across the crack interface, leading to crack healing.^{86,93} The ‘one capsule system’ is advantageous in its simplicity with no need for expensive metal catalysts²⁰² or the preparation of multiple types of microcapsules containing different healing reagents.²⁰³ The advantages of this method are particularly attractive when considering the production of transparent materials, as the reduced number of components means that the required RI matching is simplified. Previous attempts at producing the transparent extrinsic self-healing materials, reported in the literature, utilised a mechanism with incomplete RI matching of all the components;⁷⁷ where a traditional urea-formaldehyde shell material was utilised for the capsules. This shell wall is not transparent which limited the capsule size and self-healing capability of this material.⁷⁷ As a result this material was only shown for coating applications.

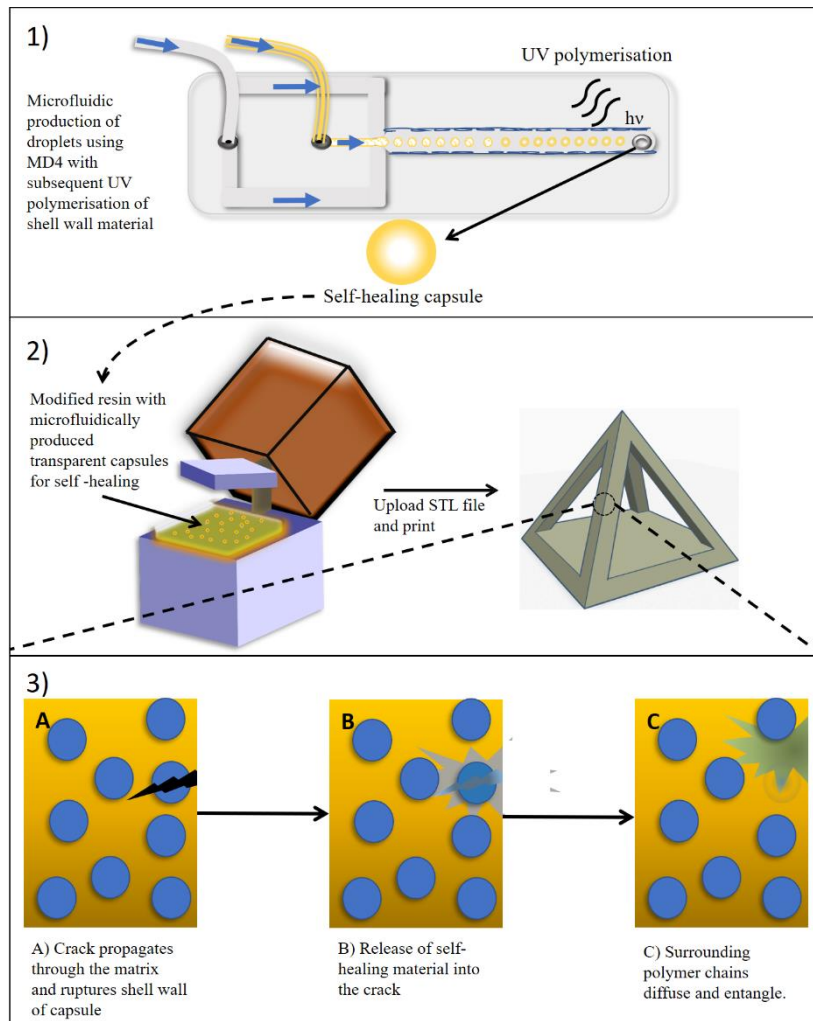
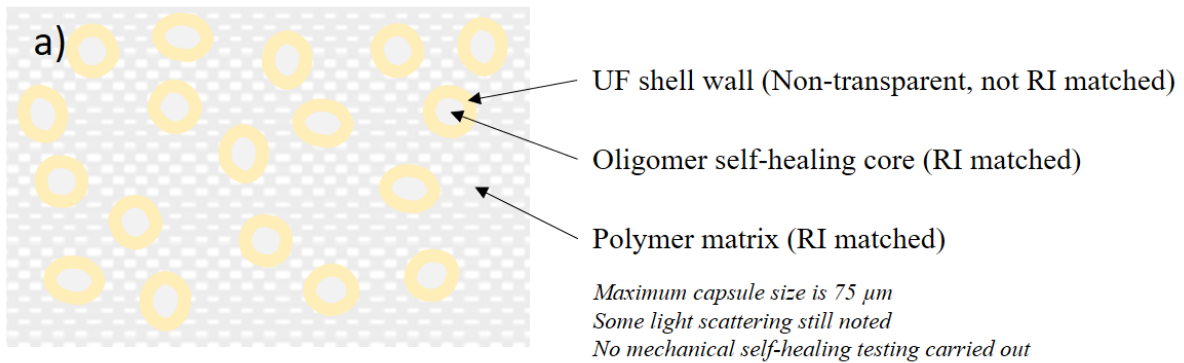


Figure 82: Overview of the fabrication process for 3D printed transparent extrinsically self-healing material. 1) Production of self-healing capsules produced using microfluidic device MD4 and shell polymerisation through exposure to the UV. 2) Addition of capsules to the 3D printing resin and 3D printing of structures. 3) Outline of the self-healing mechanism utilised here which follows a solvent welding mechanism.

In order to produce a transparent self-healing material with greater self-healing capability, larger capsules are required. Here a method which utilises an RI matched oligomer and matrix material is described. For complete RI matching and improved transparency, the shell wall material of the capsules and the matrix polymer are the same. (Figure 83)

Current example of transparent extrinsically self-healing composite



Proposed transparent extrinsically self-healing composite

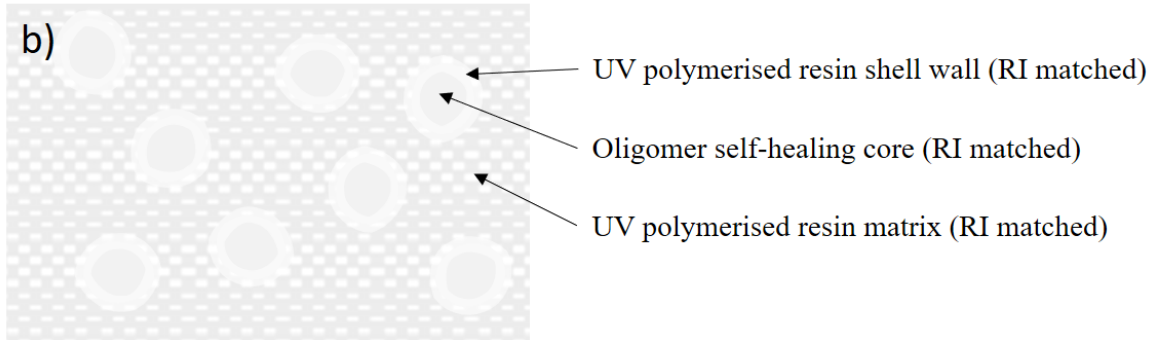


Figure 83: Comparison of a transparent self-healing mechanism within the literature (a) and the proposed mechanism in this project (b). The utilisation of UF as the shell wall material limited the size of the capsules and the possible applications.

Capsules containing an epoxy oligomer were prepared using a microfluidic device, as described in chapter 5. Using the device design MD4 (device details in section 2.15.2 and experimental set-up in section 2.7) with flow rates of 22.5 mL h⁻¹ for the CP and 0.35 mL h⁻¹ for the DP, transparent microcapsules with epoxy core, which had an average diameter of 138 ± 32 μm, were collected.

6.1 Self-healing preliminary trials

The viability of using Epon 828 epoxy oligomer as the core material for self-healing of the polymer matrix was screened in preliminary tests as detailed in section 2.7. This was carried out by addition of a thin layer of oligomer to the interface of two flat pieces of polymerised 3D printing resin, after which the surfaces were brought back together, and the sample was left for 24 h. After that time, good adhesion of the surfaces was noted (Figure 84) where the pieces were essentially bonded together. This indicates that the Epon 828 oligomer was a good candidate to be used as the core material for microcapsule based extrinsic self-healing of the 3D printing resin matrix.

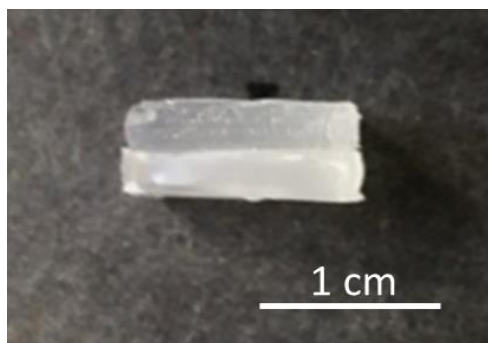


Figure 84: A preliminary plane adhesion test, utilising the EPON 828, which successfully bonded the surfaces of the two pieces of polymerised 3D printing resin. This indicated that EPON 828 should perform well as a self-healing agent for this polymer matrix.

6.2 Formulation of self-healing composites

To quantify the healing capability of these composites, a range of formulations were generated using the method outlined in section 2.9. Samples containing, 0, 5, 10 and 15 wt% capsules were prepared. Similarly to the formulations described in chapter 3, these samples underwent degassing under vacuum before polymerisation. Not only was this to reduce the likelihood of air bubbles interfering with the self-healing tests, but also to improve the transparency of the samples. Air has a much lower RI than the polymers, and thus, it was expected that upon

degassing bubbles trapped at the interface of the capsules and surrounding unpolymerised material are removed and yielding in reduced light scattering and increasing the transparency of the composite material. An example of the effect of degassing is shown in figure 85. If the matrix was polymerised without degassing after addition of the capsules, it was noted that the light scattering was significant

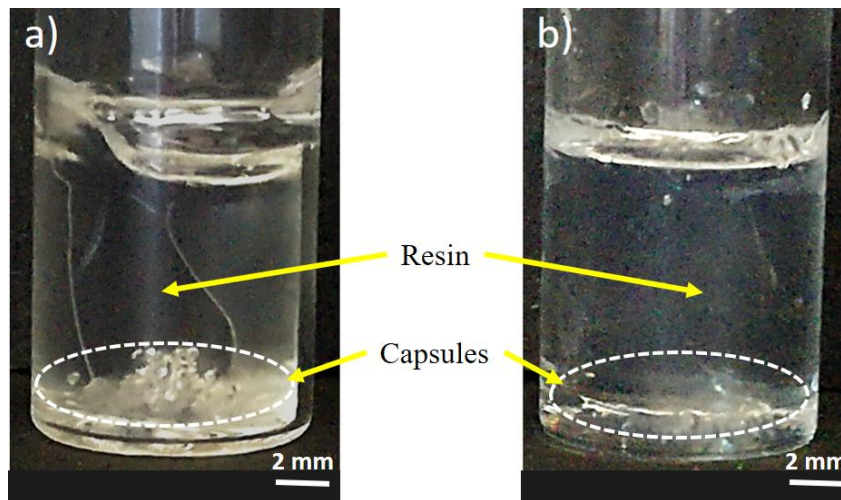


Figure 85: The appearance of samples containing capsules, (a) without a degassing step and (b) with a degassing step. Capsules were placed at the bottom of the vials with resin added above. The sample which underwent a degassing step has increased transparency, with the capsules appearing to ‘disappear’. The removal of air (which has a much lower RI compared to the polymers) at the capsule/resin interface allows for the RI matching effect to be seen much more clearly.

6.3 Quantification of self-healing

To quantify the extent of self-healing, the various formulations underwent mechanical testing using the method outlined in section 2.10. The critical load values (P_c) were obtained for both virgin samples and healed samples. For traditional UF capsule based self-healing composites, an increase in P_c (and therefore relative fracture toughness) with increasing capsule loading is often noted, suggesting that there is a toughening effect upon capsule addition.^{80,116} Looking at Figure 86 no notable change in fracture toughness was noted upon addition of microcapsules

for this mechanism. The main toughening mechanisms that are thought to contribute to the toughening effect of UF microcapsule addition in polymers is crack deformation and microcracking.¹¹⁶ The deformation of crack shape is due to crack pinning mechanisms thought to arise from the high strength but brittle UF shell and the inclusion of liquid cores causes enhanced subsurface microcracking mechanisms, which increase surface area at the crack tip, absorbing energy. The documented toughening of microcapsule based self-healing composites upon addition of the capsules is perhaps therefore not seen in this composite due to the lack of the hard, brittle UF shell.

The healing efficiencies were calculated using Equation 6. The effect of capsule loading, (Figure 87a) and healing time, (Figure 87b) were investigated. It can be seen that an increase in healing efficiency was seen with an increase in both these parameters until a maximum healing efficiency was reached which is in line with the trends reported for healing of polymers via solvent welding.^{98,209-211} A fracture toughness recovery of 83% is comparable to our previous formulations using the traditional urea-formaldehyde shell. This suggests good capsule rupture and good levels of released oligomer coating the fracture surfaces.

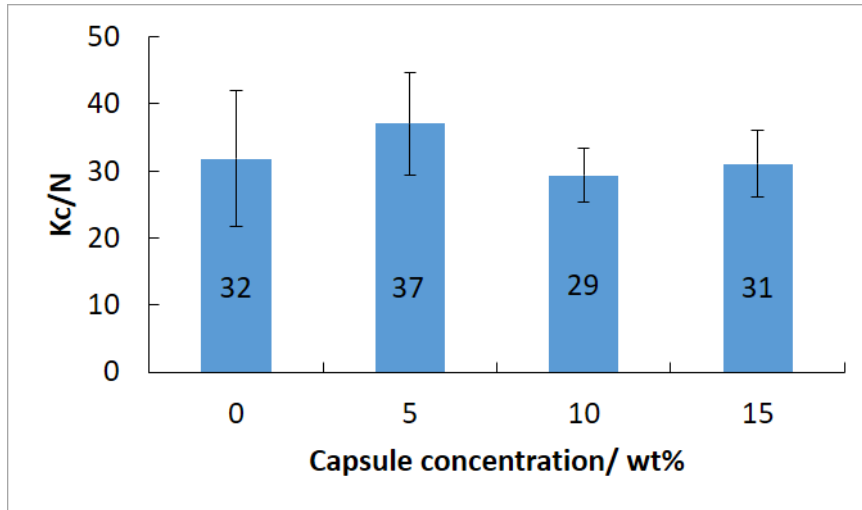


Figure 86: Critical loads of Photocentric firm resin loaded with the micro-fluidically produced epoxy capsules at different loadings. Unlike other microcapsule based self-healing composites, no significant change in critical load is seen. ($n = 3$)

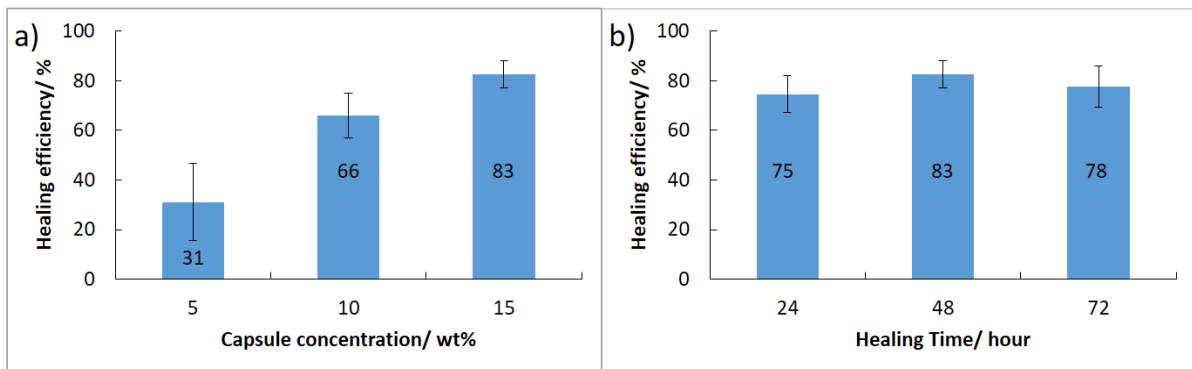


Figure 87: The healing efficiencies of materials loaded with the micro-fluidically produced capsules with epoxy cores. a) The effect of increasing capsule concentration on healing efficiency. b) The effect of increasing healing time on healing efficiency. At 15 wt% loading and with a healing time of 48 hours, the best self-healing efficiency of 83% was achieved. ($n = 3$)

When designing self-healing systems, the viscosity of the core material is often of importance. Generally, it is suggested that core materials of lower viscosity perform better.^{232,233} Considering the higher viscosity of the epoxy, the release of the material into the crack to sufficiently coat the surface was a concern. Our healing results with higher viscosity polymers are supported by previous studies using higher viscosities epoxies which resulted in up to 90% recovery.²³⁴

Furthermore, the direct comparison of high viscosity oligomers as self-healing agents is difficult due to the majority of examples in the literature using the traditional UF encapsulation method for self-healing agents.⁹¹ This method utilises a batch mixer to form an emulsion in which the discontinuous phase is the healing agent; the precipitation of urea-formaldehyde nanoparticles at the droplet interface then forms a solid shell wall. The high shear required to emulsify high viscosity polymers makes the traditional UF fabrication method unviable as the solid wall of the microcapsules are often ruptured by the mixing method.²³⁵ Our emulsification method utilising a microfluidic device has allowed for the production of capsules using these polymers and at a size not previously utilised in the self-healing literature. Therefore, there are few other examples for us to compare our results to.

6.4 3D Printing

Incorporation of the modified resins into a 3D printer allowed for 3D printed samples to be produced. Samples were generated using the method outlined in section 2.11. A print was produced using 15 wt% capsules in resin. Figure 88 shows this print compared to the 15wt% EPA UF capsules investigated in chapter 3. The use of the epoxy/resin capsules improves the transparency and the look of the final print.



Figure 88: 3D prints containing various capsule loadings. a) No capsules, b) 15 wt% epoxy capsules and c) 15 wt% EPA UF capsules. Despite both capsule containing prints having a 15 wt% loading, the appearance of the print containing the epoxy capsules is much closer to the non-loaded print.

6.5 Conclusion

Microcapsules produced using a microfluidic device were shown to possess self-healing capability and were successfully utilised in a 3D printer to produce structures.

Through the use of mode 1 fracture testing on samples which possess the TDCB geometry, the capability of fracture toughness recovery after healing via a classic solvent welding mechanism, depending on which solvent and concentration was used. Using 15 wt% loading of the capsules and allowing 48 h for self-healing, mechanical testing showed a capability for fracture toughness recovery of 83%.

The utilisation of these formulations within an SLA 3D printer allowed for the printing of self-healing composites. The addition of capsules showed a much-reduced effect on the aesthetic quality of the print when compared to prints produced using resin containing self-healing microcapsules produced using the traditional UF encapsulation method. This has can be attributed to the shell wall material being the same as the matrix material and polymer with a high RI matching that of the matrix material.

7. CONCLUSION

An extrinsically self-healing material was successfully utilised in a stereolithographic 3D printer to produce structures. Optimisation of capsule content (anisole with 5 wt% PMMA), capsule loading (5 wt%) and a healing time of 3 days allowed for fracture toughness recovery of 87%. It was noted however, that the inclusion of microcapsules with a urea-formaldehyde shell lead to a loss in optical clarity of the final material.

A method for the production of transparent self-healing capsules has been developed. Refractive index matching of shell wall material and the polymer matrix was considered. Both traditional batch mixing and droplet microfluidic methods were investigated.

Despite optimisation of the batch process, the capsules produced were too large (500 μm). Emulsion instability, aggregation problems and issues regarding removal of excess unpolymerised material were persistent problems during the optimisation process.

The utilisation of a microfluidic device proved a useful tool in overcoming the limitations encountered using the batch mixing process. Despite the high viscosity and rheological complexity of the polymer blends utilised, stable droplet generation was achieved within a flow focusing microfluidic device. It was shown that droplet size could be controlled using flow rate. Various device designs were investigated and an ideal droplet size of 138 μm was achieved. The material utilised for the microfluidic device was also investigated with the oxygen permeability of PDMS proving useful in reducing clogging issues see with continued use of glass devices. Using the optimised device MD4, UV polymerisation of the produced droplets allowed for continuous capsule production for over an hour. Utilising these capsules within the resin matrix and using mode 1 fracture testing, a fracture toughness recovery of 83% was seen, when a capsule loading of 15 wt% was used and allowed for 48 h for self-healing.

Finally, comparison of 3D printed structures when using urea formaldehyde and the transparent capsules was shown. When comparing prints with 15 wt% capsule loading, the improvement in optical clarity was evident when observing the prints produced using the microfluidically produced transparent capsules when compared to those loaded with traditional UF capsules.

Beyond this work, due to the higher degree of control afforded by the microfluidic device, further investigation into the generation of microcapsules with varying shell thickness would be beneficial. This could be achieved through variation of flow rates within the microfluidic device. Thinner shell walls could lead to a higher core content for healing, therefore increasing the self-healing capability. In addition, all self-healing TDCB samples underwent mechanical testing after being freshly prepared (1-2 days). It would be of interest to observe how the aging process (3, 6 and 12 months) would affect the self-healing process. Finally, further investigation into the material properties of the self-healing materials would be beneficial through use of standard mechanical testing geometries. Comparison of properties such as the Young's modulus would validate the use of the TDCB geometry, confirming that the change in fracture toughness is due to a change in material properties rather than an effect of the geometry.

8. REFERENCES

- 1 B. C. Gross, J. L. Erkal, S. Y. Lockwood, C. Chen and D. M. Spence, *Anal. Chem.*, 2014, **86**, 3240–3253.
- 2 A. R. Studart, *Chem. Soc. Rev.*, 2016, **45**, 359–376.
- 3 U.S Patent 6027324, 1998, 1–17.
- 4 K. Brans, *3D printing, a maturing technology*, IFAC, 2013, vol. 46.
- 5 H. Lipson and M. Kurman, *Fabricated: The New World of 3D Printing*, Wiley Publishing, 2013.
- 6 B. M. Tymrak, M. Kreiger and J. M. Pearce, *Mater. Des.*, 2014, **58**, 242–246.
- 7 R. Melnikova, A. Ehrmann and K. Finsterbusch, *IOP Conf. Ser. Mater. Sci. Eng.*, , DOI:10.1088/1757-899X/62/1/012018.
- 8 C. R. Garcia, J. Correa, D. Espalin, J. H. Barton, R. C. Rumpf, R. Wicker and V. Gonzalez, *Prog. Electromagn. Res. Lett.*, 2012, **34**, 75–82.
- 9 Q. Sun, G. M. Rizvi, C. T. Bellehumeur and P. Gu, *Rapid Prototyp. J.*, 2008, **14**, 72–80.
- 10 X. Wang, M. Jiang, Z. Zhou, J. Gou and D. Hui, *Compos. Part B Eng.*, 2017, **110**, 442–458.
- 11 R. D. Farahani, M. Dubé and D. Therriault, *Adv. Mater.*, 2016, 5794–5821.
- 12 B. G. Compton and J. A. Lewis, *Adv. Mater.*, 2014, **26**, 5930–5935.
- 13 B. N. Turner, R. Strong and S. A. Gold, *Rapid Prototyp. J.*, 2014, **20**, 192–204.
- 14 J. A. Lewis, *Adv. Funct. Mater.*, 2006, **16**, 2193–2204.

- 15 R. L. Truby and J. A. Lewis, *Nature*, 2016, **540**, 371–378.
- 16 A. Davoudinejad, L. C. D. Perez, D. Quagliotti, D. B. Pedersen, J. A. A. García, J. A. Yagüe-Fabra and G. Tosello, *Procedia Struct. Integr.*, 2018, **13**, 1250–1255.
- 17 G. Taormina, C. Sciancalepore, M. Messori and F. Bondioli, *J. Appl. Biomater. Funct. Mater.*, 2018, **16**, 151–160.
- 18 A. Bagheri and J. Jin, *ACS Appl. Polym. Mater.*, 2019, **1**, 593–611.
- 19 F. P. W. Melchels, J. Feijen and D. W. Grijpma, *Biomaterials*, 2010, **31**, 6121–6130.
- 20 R. Schwalm, *UV Coatings: Basics, Recent Developments and New Applications*, 2006.
- 21 J. Fu, H. Yin, X. Yu, C. Xie, H. Jiang, Y. Jin and F. Sheng, *Int. J. Pharm.*, 2018, **549**, 370–379.
- 22 R. J. Mondeschein, A. Kanitkar, C. B. Williams, V. S. S and T. E. Long, *Biomaterials*, 2017, **140**, 170–188.
- 23 A. Endruweit, M. S. Johnson and A. C. Long, *Polym. Compos.*, 2006, **27**, 119–128.
- 24 C. Mendes-Felipe, J. Oliveira, I. Etxebarria, J. L. Vilas-Vilela and S. Lanceros-Mendez, *Adv. Mater. Technol.*, 2019, **4**, 1–16.
- 25 S. C. Ligon, R. Liska, J. Stampfl, M. Gurr and R. Mülhaupt, *Chem. Rev.*, 2017, **117**, 10212–10290.
- 26 J. P. Fouassier and J. Lalevee, *Photoinitiators for Polymer Synthesis: Scope, Reactivity and Efficiency*, 2012.
- 27 A. Tiwari and A. Polykarpov, *Photocured Materials*, 2015.
- 28 A. Kajiwara, Y. Konishi, Y. Morishima, W. Schnabel, K. Kuwata and M. Kamachi,

- Macromolecules*, 1993, **26**, 1656–1658.
- 29 T. Sumiyoshi, W. Schnabel, A. Henne and P. Lechtken, *Polymer (Guildf)*., 1985, **26**, 141–146.
- 30 H. Itoh, A. Kameyama and T. Nishikubo, *J. Polym. Sci. Part A Polym. Chem.*, 1996, **34**, 217–225.
- 31 J. Xu, Y. Jiang, T. Zhang, Y. Dai, D. Yang, F. Qiu, Z. Yu and P. Yang, *Prog. Org. Coatings*, 2018, **122**, 10–18.
- 32 T. Scherzer, W. Knolle, S. Naumov and R. Mehnert, *Nucl. Instruments Methods Phys. Res. Sect. B Beam Interact. with Mater. Atoms*, 2003, **208**, 271–276.
- 33 C. Check, R. Chartoff and S. Chang, *React. Funct. Polym.*, 2015, **97**, 116–122.
- 34 V. Shukla, M. Bajpai, D. K. Singh, M. Singh and R. Shukla, *Pigment Resin Technol.*, 2004, **33**, 272–279.
- 35 1989, 1–5.
- 36 J. W. Choi, E. MacDonald and R. Wicker, *Int. J. Adv. Manuf. Technol.*, 2010, **49**, 543–551.
- 37 J. W. Choi, H. C. Kim and R. Wicker, *J. Mater. Process. Technol.*, 2011, **211**, 318–328.
- 38 J. Borrello, P. Nasser, J. c. Iatridis and K. D. Costa, *Addit. Manuf.*, 2018, **23**, 374–380.
- 39 G. Taormina, C. Sciancalepore, F. Bondioli and M. Messori, *Polymers (Basel)*., , DOI:10.3390/polym10020212.
- 40 M. Gurr, D. Hofmann, M. Ehm, Y. Thomann, R. Kubier and R. Mülhaupt, *Adv. Funct. Mater.*, 2008, **18**, 2390–2397.

- 41 J. Czyzewski, P. Burzyński, K. Gawel and J. Meisner, *J. Mater. Process. Technol.*, 2009, **209**, 5281–5285.
- 42 S. Kumar and J. P. Kruth, *Mater. Des.*, 2010, **31**, 850–856.
- 43 D. Cvetković, *3D Printing*, 2018.
- 44 J. Z. Manapat, J. D. Mangadlao, B. D. B. Tiu, G. C. Tritchler and R. C. Advincula, *ACS Appl. Mater. Interfaces*, 2017, **9**, 10085–10093.
- 45 D. Lin, S. Jin, F. Zhang, C. Wang, Y. Wang, C. Zhou and G. J. Cheng, *Nanotechnology*, , DOI:10.1088/0957-4484/26/43/434003.
- 46 J. H. Sandoval and R. B. Wicker, *Rapid Prototyp. J.*, 2006, **12**, 292–303.
- 47 J. H. Sandoval, K. F. Soto, L. E. Murr and R. B. Wicker, *J. Mater. Sci.*, 2007, **42**, 156–165.
- 48 H. Eng, S. Maleksaeedi, S. Yu, Y. Y. C. Choong, F. E. Wiria, C. L. C. Tan, P. C. Su and J. Wei, *Procedia Eng.*, 2017, **216**, 1–7.
- 49 M. Sušec, S. C. Ligon, J. Stampfl, R. Liska and P. Krajnc, *Macromol. Rapid Commun.*, 2013, **34**, 938–943.
- 50 D. W. Johnson, C. Sherborne, M. P. Didsbury, C. Pateman, N. R. Cameron and F. Claeysens, *Adv. Mater.*, 2013, **25**, 3178–3181.
- 51 I. Cooperstein, M. Layani and S. Magdassi, *J. Mater. Chem. C*, 2015, **3**, 2040–2044.
- 52 M. D. Hager, P. Greil, C. Leyens, S. Van Der Zwaag and U. S. Schubert, *Adv. Mater.*, 2010, **22**, 5424–5430.
- 53 J. C. Cremaldi and B. Bhushan, *Beilstein J. Nanotechnol.*, 2018, **9**, 907–935.

- 54 B. Bhushan, Y. C. Jung and K. Koch, *Philos. Trans. R. Soc. A Math. Phys. Eng. Sci.*, 2009, **367**, 1631–1672.
- 55 G. Bauer, A. Nellesen and T. Speck, *WIT Trans. Ecol. Environ.*, 2010, **138**, 453–459.
- 56 K. S. Toohey, N. R. Sottos, J. A. Lewis, J. S. Moore and S. R. White, *Nat. Mater.*, 2007, **6**, 581–585.
- 57 K. S. Toohey, C. J. Hansen, J. A. Lewis, S. R. White and N. R. Sottos, *Adv. Funct. Mater.*, 2009, **19**, 1399–1405.
- 58 Y. C. Yuan, T. Yin, M. Z. Rong and M. Q. Zhang, *Express Polym. Lett.*, 2008, **2**, 238–250.
- 59 S. J. Rowan, S. J. Cantrill, G. R. L. Cousins, J. K. M. Sanders and J. F. Stoddart, *Angew. Chemie Int. Ed.*, 2002, **41**, 898–952.
- 60 R. J. Wojtecki, M. A. Meador and S. J. Rowan, *Nat. Mater.*, 2011, **10**, 14–27.
- 61 S. R. White, B. J. Blaiszik, S. L. B. Kramer, S. C. Olugebefola, J. S. Moore and N. R. Sottos, *Am. Sci.*, 2011, **99**, 392–399.
- 62 P. Cordier, F. Tournilhac, C. Soulié-Ziakovic and L. Leibler, *Nature*, 2008, **451**, 977–980.
- 63 M. Burnworth, L. Tang, J. R. Kumpfer, A. J. Duncan, F. L. Beyer, G. L. Fiore, S. J. Rowan and C. Weder, *Nature*, 2011, **472**, 334–337.
- 64 Y. Amamoto, H. Otsuka, A. Takahara and K. Matyjaszewski, *Adv. Mater.*, 2012, **24**, 3975–3980.
- 65 H. Jiang, G. Zhang, X. Feng, H. Liu, F. Li, M. Wang and H. Li, *Compos. Sci. Technol.*,

- 2017, **140**, 54–62.
- 66 D. Y. Wu, S. Meure and D. Solomon, *Prog. Polym. Sci.*, 2008, **33**, 479–522.
- 67 A. Yousefpour, M. Hojjati and J. P. Immarigeon, *J. Thermoplast. Compos. Mater.*, 2004, **17**, 303–341.
- 68 R. P. Wool and K. M. O'Connor, *Polym. Eng. Sci.*, 1981, **21**, 970–977.
- 69 C. . Lin, S. Lee and K. S. Liu, *Polym. Eng. Sci.*, 1990, **30**, 1399–1406.
- 70 P. Wang, S. Lee and J. P. Harmon, *J. Polym. Sci. Part B-Polymer Phys.*, 1994, **32**, 1217–1227.
- 71 S. R. White, N. R. Sottos, P. H. Geubelle, J. S. Moore, M. R. Kessler, S. R. Sriram, E. N. Brown and S. Viswanathan, *Nature*, 2001, **409**, 794–797.
- 72 G. O. Wilson, J. S. Moore, S. R. White, N. R. Sottos and H. M. Andersson, *Adv. Funct. Mater.*, 2008, **18**, 44–52.
- 73 G. O. Wilson, M. M. Caruso, N. T. Reimer, S. R. White, N. R. Sottos and J. S. Moore, *Chem. Mater.*, 2008, **20**, 3288–3297.
- 74 P. Kardar, *Prog. Org. Coatings*, 2015, **89**, 271–276.
- 75 Y. Jinglei, M. W. Keller, J. S. Moore, S. R. White and N. R. Sottos, *Macromolecules*, 2008, **41**, 9650–9655.
- 76 P. Kardar, *Prog. Org. Coatings*, 2015, **89**, 271–276.
- 77 A. C. Jackson, J. A. Bartelt and P. V. Braun, *Adv. Funct. Mater.*, 2011, **21**, 4705–4711.
- 78 K. S. Toohey, C. J. Hansen, J. A. Lewis, S. R. White and N. R. Sottos, *Adv. Funct. Mater.*, 2009, **19**, 1399–1405.

- 79 E. N. Brown, N. R. Sottos and S. R. White, *Exp. Mech.*, 2002, **42**, 372–379.
- 80 E. N. Brown, S. R. White and N. R. Sottos, *J. Mater. Sci.*, 2006, **41**, 6266–6273.
- 81 J. D. Rule, N. R. Sottos and S. R. White, *Polymer (Guildf.)*, 2007, **48**, 3520–3529.
- 82 J. M. Kamphaus, J. D. Rule, J. S. Moore, N. R. Sottos and S. R. White, *J. R. Soc. Interface*, 2008, **5**, 95–103.
- 83 H. Li, R. Wang and W. Liu, *J. Reinf. Plast. Compos.*, 2012, **31**, 924–932.
- 84 B. J. Blaiszik, M. M. Caruso, D. A. McIlroy, J. S. Moore, S. R. White and N. R. Sottos, *Polymer (Guildf.)*, 2009, **50**, 990–997.
- 85 M. M. Caruso, D. A. Delafuente, V. Ho, N. R. Sottos, J. S. Moore and S. R. White, *Macromolecules*, 2007, **40**, 8830–8832.
- 86 M. M. Caruso, D. A. Delafuente, V. Ho, N. Sottos, S. White and J. S. Moore, *Am. Chem. Soc. Polym. Prepr. Div. Polym. Chem.*, 2008, **49**, 974–975.
- 87 A. D. N. Celestine, N. R. Sottos and S. R. White, *Polym. (United Kingdom)*, 2015, **69**, 241–248.
- 88 C. J. Hansen, W. Wu, K. S. Toohey, N. R. Sottos, S. R. White and J. A. Lewis, *Adv. Mater.*, 2009, **21**, 4143–4147.
- 89 S. R. White, J. S. Moore, N. R. Sottos, B. P. Krull, W. A. Santa Cruz and R. C. R. Gergely, *Science (80-.)*, 2014, **344**, 620–623.
- 90 S. Billiet, X. K. D. Hillewaere, R. F. A. Teixeira and F. E. Du Prez, *Macromol. Rapid Commun.*, 2013, **34**, 290–309.
- 91 E. N. Brown, M. R. Kessler, N. R. Sottos and S. R. White, *J. Microencapsul.*, 2003, **20**,

- 719–730.
- 92 L. P. Liao, W. Zhang, Y. Xin, H. M. Wang, Y. Zhao and W. J. Li, *Chinese Sci. Bull.*, 2011, **56**, 439–443.
- 93 M. M. Caruso, B. J. Blaiszik, S. R. White, N. R. Sottos and J. S. Moore, *Adv. Funct. Mater.*, 2008, **18**, 1898–1904.
- 94 P. Sanders, A. J. Young, Y. Qin, K. S. Fancey, M. R. Reithofer, R. Guillet-Nicolas, F. Kleitz, N. Pamme and J. M. Chin, *Sci. Rep.*, 2019, **9**, 1–6.
- 95 M. Nadgorny, Z. Xiao and L. A. Connal, *Mol. Syst. Des. Eng.*, 2017, **2**, 283–292.
- 96 D. L. Taylor and M. in het Panhuis, *Adv. Mater.*, 2016, **28**, 9060–9093.
- 97 Z. Wei, J. He, T. Liang, H. Oh, J. Athas, Z. Tong, C. Wang and Z. Nie, *Polym. Chem.*, 2013, **4**, 4601–4605.
- 98 R. P. Wool and K. M. O'Connor, *J. Appl. Phys.*, 1981, **52**, 5953–5963.
- 99 E. N. Brown, *J. Strain Anal. Eng. Des.*, 2011, **46**, 167–186.
- 100 A. M. Grande, S. J. Garcia and S. Van Der Zwaag, *Polym. (United Kingdom)*, 2015, **56**, 435–442.
- 101 B. Aïssa, D. Therriault, E. Haddad and W. Jamroz, *Adv. Mater. Sci. Eng.*, 2012, **2012**, 1–17.
- 102 K. Zhu, Q. Song, H. Chen and P. Hu, *J. Appl. Polym. Sci.*, , DOI:10.1002/app.45929.
- 103 E. Tsangouri, D. Aggelis and D. Van Hemelrijck, *Prog. Polym. Sci.*, 2015, **49–50**, 154–174.
- 104 D. Garoz Gómez, F. A. Gilabert, E. Tsangouri, D. Van Hemelrijck, X. K. D. Hillewaere,

- F. E. Du Prez and W. Van Paepegem, *Int. J. Solids Struct.*, 2015, **64**, 145–154.
- 105 D. H. Kafagy, S. S. Khajotia and M. W. Keller, *Polym. Test.*, 2017, **59**, 152–159.
- 106 R. J. Lemmens, Q. Dai and D. D. Meng, *Theor. Appl. Fract. Mech.*, 2014, **74**, 23–29.
- 107 B. W. Greenland and W. Hayes, *Healable Polymer Systems*, Royal Society of Chemistry, 2013.
- 108 D. Roylance, *Int. J. Rock Mech. Min. Sci. Geomech. Abstr.*, 1988, **25**, A201.
- 109 A. A. Griffith, *Philos. Trans. R. Soc. London. Ser. A, Contain. Pap. a Math. or Phys. Character*, 1921, **221**, 163–198.
- 110 K. Van Tittelboom and N. De Belie, *Materials (Basel)*, 2013, **6**, 2182–2217.
- 111 J. Wang, K. Van Tittelboom, N. De Belie and W. Verstraete, *Constr. Build. Mater.*, 2012, **26**, 532–540.
- 112 S. J. García, H. R. Fischer and S. Van Der Zwaag, *Prog. Org. Coatings*, 2011, **72**, 211–221.
- 113 M. Huang and J. Yang, *J. Mater. Chem.*, 2011, **21**, 11013–11440.
- 114 Y. Du, D. Li, L. Liu and G. Gai, *Polymers (Basel)*, 2018, **10**, 1–25.
- 115 J. W. C. Pang and I. P. Bond, *Compos. Sci. Technol.*, 2005, **65**, 1791–1799.
- 116 E. N. Brown, S. R. White and N. R. Sottos, *J. Mater. Sci. Vol.*, 2004, **39**, 1703–1710.
- 117 H. Zhang and Y. Zhao, *ACS Appl. Mater. Interfaces*, 2013, **5**, 13069–13075.
- 118 P. Reutenauer, E. Buhler, P. J. Boul, S. J. Candau and J. M. Lehn, *Chem. A Eur. J.*, 2009, **15**, 1893–1900.

- 119 H. Ullah, K. A. M. Azizli, Z. B. Man, M. B. Che Ismail and M. I. Khan, *Polym. Rev.*, 2016, **56**, 429–485.
- 120 H. Wei, Y. Wang, J. Guo, N. Z. Shen, D. Jiang, X. Zhang, X. Yan, J. Zhu, Q. Wang, L. Shao, H. Lin, S. Wei and Z. Guo, *J. Mater. Chem. A*, 2015, **3**, 469–480.
- 121 R. P. Wool, *Soft Matter*, 2008, **4**, 400–418.
- 122 C. Fan, J. Tang and X. Zhou, *J. Appl. Polym. Sci.*, 2013, **129**, 2848–2856.
- 123 A. S. Gladman, A. D. N. Celestine, N. R. Sottos and S. R. White, *Adv. Healthc. Mater.*, 2015, **4**, 202–207.
- 124 F. Ahangaran, M. Hayaty and A. H. Navarchian, *Appl. Surf. Sci.*, 2017, **399**, 721–731.
- 125 Q. Li, A. K. Mishra, N. H. Kim, T. Kuila, K. T. Lau and J. H. Lee, *Compos. Part B Eng.*, 2013, **49**, 6–15.
- 126 F. Ahangaran, A. H. Navarchian, M. Hayaty and K. Esmailpour, *Smart Mater. Struct.*, , DOI:10.1088/0964-1726/25/9/095035.
- 127 E. Koh, N. K. Kim, J. Shin and Y. W. Kim, *RSC Adv.*, 2014, **4**, 16214–16223.
- 128 E. Koh, S. Y. Baek, N. K. Kim, S. Lee, J. Shin and Y. W. Kim, *New J. Chem.*, 2014, **38**, 4409–4419.
- 129 I. Polenz, S. S. Datta and D. A. Weitz, *Langmuir*, 2014, **30**, 13405–13410.
- 130 I. Polenz, D. A. Weitz and J. C. Baret, *Langmuir*, 2015, **31**, 1127–1134.
- 131 H. Zhang, X. Zhang, C. Bao, X. Li, D. Sun, F. Duan, K. Friedrich and J. Yang, *J. Mater. Chem. A*, 2018, **6**, 24092–24099.
- 132 P. W. Chen, G. Cadisch and A. R. Studart, *Langmuir*, 2014, **30**, 2346–2350.

- 133 L. Souza and A. Al-Tabbaa, *Constr. Build. Mater.*, 2018, **184**, 713–722.
- 134 I. L. Hia, P. Pasbakhsh, E. S. Chan and S. P. Chai, *Sci. Rep.*, 2016, **6**, 1–8.
- 135 K. Lv, D. Liu, W. Li, S. Tang and X. Zhou, *Mol. Cryst. Liq. Cryst.*, 2012, **557**, 217–227.
- 136 M. Attaei, M. V. Loureiro, M. do Vale, J. A. D. Condeço, I. Pinho, J. C. Bordado and A. C. Marques, *Polymers (Basel)*, , DOI:10.3390/polym10080825.
- 137 D. Mark, S. Haeberle, G. Roth, F. von Stetten and R. Zengerle, *Chem. Soc. Rev.*, 2010, **39**, 1153–1182.
- 138 Y. Zhao, L. Shang, Y. Cheng and Z. Gu, *Acc. Chem. Res.*, 2014, **47**, 3632–3642.
- 139 D. Dendukuri and P. S. Doyle, *Adv. Mater.*, 2009, **21**, 4071–4086.
- 140 W. Wang, M. J. Zhang and L. Y. Chu, *Acc. Chem. Res.*, 2014, **47**, 373–384.
- 141 S. S. Datta, A. Abbaspourrad, E. Amstad, J. Fan, S. H. Kim, M. Romanowsky, H. C. Shum, B. Sun, A. S. Utada, M. Windbergs, S. Zhou and D. A. Weitz, *Adv. Mater.*, 2014, **26**, 2205–2218.
- 142 G. M. Whitesides, *Nature*, 2006, **442**, 368–373.
- 143 K. Ren, J. Zhou and H. Wu, *Acc. Chem. Res.*, 2013, **46**, 2396–2406.
- 144 C. Iliescu, H. Taylor, M. Avram, J. Miao and S. Franssila, *Biomicrofluidics*, 2012, **6**, 16505–1650516.
- 145 X. Yao, Y. Zhang, L. Du, J. Liu and J. Yao, *Renew. Sustain. Energy Rev.*, 2015, **47**, 519–539.
- 146 J. Atencia and D. J. Beebe, *Nature*, 2005, **437**, 648–655.

- 147 H. Song, D. L. Chen and R. F. Ismagilov, *Angew. Chemie - Int. Ed.*, 2006, **45**, 7336–7356.
- 148 H. Song, J. D. Tice and R. F. Ismagilov, *Angew. Chemie - Int. Ed.*, 2003, **42**, 768–772.
- 149 L. Shang, Y. Cheng and Y. Zhao, *Chem. Rev.*, 2017, **117**, 7964–8040.
- 150 J. P. Brody, P. Yager, R. E. Goldstein and R. H. Austin, *Biophys. J.*, 1996, **71**, 3430–3441.
- 151 M. D. Tarn, M. J. Lopez-Martinez and N. Pamme, *Anal. Bioanal. Chem.*, 2014, **406**, 139–161.
- 152 J. D. Tice, H. Song, A. D. Lyon and R. F. Ismagilov, *Langmuir*, 2003, **19**, 9127–9133.
- 153 W. Wang, R. Xie, X.-J. Ju, T. Luo, L. Liu, D. A. Weitz and L.-Y. Chu, *Lab Chip*, 2011, **11**, 1587–1592.
- 154 B. Lu, M. D. Tarn, N. Pamme and T. K. Georgiou, *J. Polym. Sci. Part A Polym. Chem.*, 2018, **56**, 59–66.
- 155 Y. Jun, E. Kang, S. Chae and S.-H. Lee, *Lab Chip*, 2014, **14**, 2145–2160.
- 156 D. C. Appleyard, S. C. Chapin, R. L. Srinivas and P. S. Doyle, *Nat. Protoc.*, 2011, **6**, 1761–1774.
- 157 G. Villar, A. D. Graham and H. Bayley, *Science (80-.)*, 2013, **340**, 48–52.
- 158 S. Seiffert, J. Thiele, A. R. Abate and D. A. Weitz, *J. Am. Chem. Soc.*, 2010, **132**, 6606–6609.
- 159 A. R. Abate, C. H. Chen, J. J. Agresti and D. A. Weitz, *Lab Chip*, 2009, **9**, 2628–2631.
- 160 J. Saliba, A. Daou, S. Damiani, J. Saliba, M. El-Sabban and R. Mhanna, *Genes (Basel)*,

- , DOI:10.3390/genes9060285.
- 161 V. Italia, A. N. Giakoumaki, S. Bonfadini, V. Bharadwaj, T. Le Phu, S. M. Eaton, R. Ramponi, G. Bergamini, G. Lanzani and L. Criante, *Micromachines*, 2018, **10**, 1–10.
- 162 C. X. Zhao and A. P. J. Middelberg, *Chem. Eng. Sci.*, 2011, **66**, 1394–1411.
- 163 L. Capretto, W. Cheng, M. Hill and X. Zhang, *Top. Curr. Chem.*, 2011, **304**, 27–68.
- 164 M. R. Bringer, C. J. Gerdts, H. Song, J. D. Tice and R. F. Ismagilov, *Philos. Trans. R. Soc. A Math. Phys. Eng. Sci.*, 2004, **362**, 1087–1104.
- 165 A. Suea-Ngam, P. D. Howes, M. Srisa-Art and A. J. Demello, *Chem. Commun.*, 2019, **55**, 9895–9903.
- 166 M. Baker, *Nat. Methods*, 2012, **9**, 541–544.
- 167 S. Mashaghi, A. Abbaspourrad, D. A. Weitz and A. M. van Oijen, *TrAC - Trends Anal. Chem.*, 2016, **82**, 118–125.
- 168 H. N. Joensson and H. Andersson Svahn, *Angew. Chemie - Int. Ed.*, 2012, **51**, 12176–12192.
- 169 M. Pflumm, *Nat. Methods*, 2008, **5**, 580–581.
- 170 T. Schneider, J. Kreutz and D. T. Chiu, *Anal. Chem.*, 2013, **85**, 3476–3482.
- 171 <https://www.bio-rad.com/en-uk/applications-technologies/droplet-digital-pcr-ddpcr-technology?ID=MDV31M4VY>, accessed 10/02/2020.
- 172 H. Zec, D. J. Shin and T. H. Wang, *Expert Rev. Mol. Diagn.*, 2014, **14**, 787–801.
- 173 A. K. Price and B. M. Paegel, *Anal. Chem.*, 2016, **88**, 339–353.

- 174 L. Y. Hung, C. H. Wang, C. Y. Fu, P. Gopinathan and G. Bin Lee, *Lab Chip*, 2016, **16**, 2759–2774.
- 175 N. Shembekar, C. Chaipan, R. Utharala and C. A. Merten, *Lab Chip*, 2016, **16**, 1314–1331.
- 176 Dittrich Petra S and M. Andreas, *Nat. Rev. Drug Discov.*, 2006, **5**, 210.
- 177 P. Neuzil, S. Giselbrecht, K. Länge, T. J. Huang and A. Manz, *Nat. Rev. Drug Discov.*, 2012, **11**, 620–632.
- 178 S. Neethirajan, I. Kobayashi, M. Nakajima, D. Wu, S. Nandagopal and F. Lin, *Lab Chip*, 2011, **11**, 1574–1586.
- 179 E. Y. u. Basova and F. Foret, *Analyst*, 2015, **140**, 22–38.
- 180 S. Marre and K. F. Jensen, *Chem. Soc. Rev.*, 2010, **39**, 1183–1202.
- 181 J. H. Kim, T. Y. Jeon, T. M. Choi, T. S. Shim, S. H. Kim and S. M. Yang, *Langmuir*, 2014, **30**, 1473–1488.
- 182 S. Abalde-Cela, P. Taladriz-Blanco, M. G. De Oliveira and C. Abell, *Sci. Rep.*, , DOI:10.1038/s41598-018-20754-x.
- 183 L. Xu, J. Peng, M. Yan, D. Zhang and A. Q. Shen, *Chem. Eng. Process. Process Intensif.*, 2016, **102**, 186–193.
- 184 T. Gu, C. Zheng, F. He, Y. Zhang, S. A. Khan and T. A. Hatton, *Lab Chip*, 2018, **18**, 1330–1340.
- 185 M. Faustini, J. Kim, G. Y. Jeong, J. Y. Kim, H. R. Moon, W. S. Ahn and D. P. Kim, *J. Am. Chem. Soc.*, 2013, **135**, 14619–14626.

- 186 P. Xue, Y. Wu, N. V. Menon and Y. Kang, *Microfluid. Nanofluidics*, 2014, **18**, 333–342.
- 187 C.-H. Yang, C.-Y. Wang, A. M. Grumezescu, A. H.-J. Wang, C.-J. Hsiao, Z.-Y. Chen and K.-S. Huang, *Electrophoresis*, 2014, **35**, NA-NA.
- 188 T. Watanabe, T. Ono and Y. Kimura, *Soft Matter*, 2011, **7**, 9894–9897.
- 189 W. Wang, M. J. Zhang, R. Xie, X. J. Ju, C. Yang, C. L. Mou, D. A. Weitz and L. Y. Chu, *Angew. Chemie - Int. Ed.*, 2013, **52**, 8084–8087.
- 190 S. Yang, F. Guo, B. Kiraly, X. Mao, M. Lu, K. W. Leong and T. J. Huang, *Lab Chip*, 2012, **12**, 2097–2102.
- 191 P. W. Chen, G. Cadisch and A. R. Studart, *Langmuir*, 2014, **30**, 2346–2350.
- 192 B. Shu, S. Wu, L. Dong, Q. Wang and Q. Liu, *Materials (Basel)*, , DOI:10.3390/ma11040630.
- 193 C. Zhang, W. Gao, Y. Zhao and Y. Chen, *Appl. Phys. Lett.*, , DOI:10.1063/1.5064439.
- 194 J. B. Edel, R. Fortt, J. C. DeMello and A. J. DeMello, *Chem. Commun.*, 2002, **2**, 1136–1137.
- 195 S. Krishnadasan, R. J. C. Brown, A. J. DeMello and J. C. DeMello, *Lab Chip*, 2007, **7**, 1434–1441.
- 196 L. Bai, Y. Fu, S. Zhao and Y. Cheng, *Chem. Eng. Sci.*, 2016, **145**, 141–148.
- 197 J. D. Tice, A. D. Lyon and R. F. Ismagilov, *Anal. Chim. Acta*, 2004, **507**, 73–77.
- 198 T. Cubaud and T. G. Mason, *Phys. Fluids*, 2008, **20**, 1–11.
- 199 T. McCreedy, *TrAC - Trends Anal. Chem.*, 2000, **19**, 396–401.

- 200 T. McCreedy, *Anal. Chim. Acta*, 2001, **427**, 39–43.
- 201 D. C. Duffy, J. C. McDonald, O. J. A. Schueller and G. M. Whitesides, *Anal. Chem.*, 1998, **70**, 4974–4984.
- 202 M. R. Kessler and S. R. White, *Compos. Part A Appl. Sci. Manuf.*, 2001, **32**, 683–699.
- 203 H. Jin, C. L. Mangun, A. S. Griffin, J. S. Moore, N. R. Sottos and S. R. White, *Adv. Mater.*, 2014, **26**, 282–287.
- 204 J. M. Taylor, P. M. Jenner and W. I. Jones, *Toxicol. Appl. Pharmacol.*, 1964, **6**, 378–387.
- 205 N. Shahabudin, R. Yahya and S. N. Gan, *Mater. Today Proc.*, 2016, **3**, 88–95.
- 206 R. Shinnar, *J. Fluid Mech.*, 1961, **10**, 259–275.
- 207 M. A. Aravand and M. A. Semsarzadeh, *Macromol. Symp.*, 2008, **274**, 141–147.
- 208 C. Testa, I. Sigillo and N. Grizzuti, *Polymer (Guildf.)*, 2001, **42**, 5651–5659.
- 209 R. P. Wool and K. M. O’Connor, *J. Polym. Sci.*, 1982, **20**, 7–16.
- 210 K. Jud and H. H. Kausch, *Polym. Bull.*, 1979, **1**, 697–707.
- 211 K. Jud, H. H. Kausch and J. G. Williams, *J. Mater. Sci.*, 1981, **16**, 204–210.
- 212 A. D. N. Celestine, N. R. Sottos and S. R. White, *Polym. (United Kingdom)*, 2015, **69**, 241–248.
- 213 S. Lampman, *Characterisation and Failure Analysis of Plastics*, ASM International, 2003.
- 214 J. D. Rule, N. R. Sottos and S. R. White, *Polymer (Guildf.)*, 2007, **48**, 3520–3529.

- 215 M. Araújo, S. Chatrabhuti, S. Gurdebeke, N. Alderete, K. Van Tittelboom, J. M. Raquez, V. Cnudde, S. Van Vlierberghe, N. De Belie and E. Gruyaert, *Cem. Concr. Compos.*, 2018, **89**, 260–271.
- 216 A. Loxley and B. Vincent, *J. Colloid Interface Sci.*, 1998, **62**, 49–62.
- 217 M. Li, O. Rouaud and D. Poncelet, *Int. J. Pharm.*, 2008, **363**, 26–39.
- 218 R. Jeyanthi, B. C. Thanoo, R. C. Metha and P. P. DeLuca, *J. Control. Release*, 1996, **38**, 235–244.
- 219 P. DeRoussel, D. V. Khakhar and J. M. Ottino, *Chem. Eng. Sci.*, 2001, **56**, 5511–5529.
- 220 P. DeRoussel, D. V. Khakhar and J. M. Ottino, *Chem. Eng. Sci.*, 2001, **56**, 5531–5537.
- 221 P. Zhu and L. Wang, *Lab Chip*, 2017, **17**, 34–75.
- 222 J. D. Tice, A. D. Lyon and R. F. Ismagilov, *Anal. Chim. Acta*, 2004, **507**, 73–77.
- 223 K. Studer, C. Decker, E. Beck and R. Schwalm, *Prog. Org. Coatings*, 2003, **48**, 92–100.
- 224 K. Studer, C. Decker, E. Beck and R. Schwalm, *Prog. Org. Coatings*, 2003, **48**, 101–111.
- 225 J. Alvankarian and B. Y. Majlis, *Microsyst. Technol.*, 2017, **23**, 1805–1812.
- 226 J. R. Tumbleston, D. Shirvanyants, N. Ermoshkin, R. Januszewicz, A. R. Johnson, D. Kelly, K. Chen, R. Pinschmidt, J. P. Rolland, A. Ermoshkin, E. T. Samulski and J. M. DeSimone, *Science (80-.)*, 2015, **347**, 1349–1352.
- 227 Y. Pan, H. He, J. Xu and A. Feinerman, *Rapid Prototyp. J.*, 2017, **23**, 353–361.
- 228 M. F. Haase and J. Brujic, *Angew. Chemie - Int. Ed.*, 2014, **53**, 11793–11797.

- 229 J. Man, S. Chien, S. Liang, J. Li and H. Chen, *ChemPhysChem*, 2018, **19**, 1995–1998.
- 230 S. Wang, O. Jeon, P. G. Shankles, Y. Liu, E. Alsberg, S. T. Retterer, B. P. Lee and C. K. Choi, *Biomicrofluidics*, 2016, **10**, 1–4.
- 231 S. Seiffert, J. Dubbert and D. A. Weitz, *Lab Chip*, 2011, **11**, 966–968.
- 232 S. N. Gan and N. Shahabudin, *Applications of Microcapsules in Self-Healing Polymeric Materials*, 2019, vol. i.
- 233 K. Ghosh, Swapan, *Self-Healing Materials, Fundamentals, Design Strategies and Applications*, 2009.
- 234 Y. C. Yuan, M. Z. Rong, M. Q. Zhang and G. C. Yang, *Polymer (Guildf)*., 2009, **50**, 5771–5781.
- 235 P. A. Bolimowski, I. P. Bond and D. F. Wass, *Philos. Trans. R. Soc. A Math. Phys. Eng. Sci.*, , DOI:10.1098/rsta.2015.0083.